INVESTIGATION OF PT SYMMETRY BREAKING AND EXCEPTIONAL POINTS IN DELAY-COUPLED SEMICONDUCTOR LASERS

by

Andrew Wilkey

A Dissertation

Submitted to the Faculty of Purdue University

In Partial Fulfillment of the Requirements for the degree of

Doctor of Philosophy

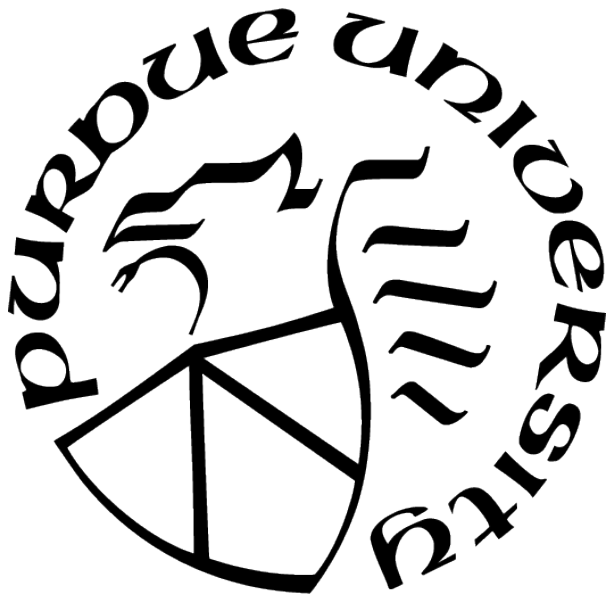

Department of Physics

Indianapolis, Indiana

August 2021

THE PURDUE UNIVERSITY GRADUATE SCHOOL
STATEMENT OF COMMITTEE APPROVAL

Dr. Gautam Vemuri, Co-Chair

Department of Physics

Dr. Yogesh Joglekar, Co-Chair

Department of Physics

Dr. Jing Liu

Department of Physics

Dr. Jeff Ou

Department of Physics

Dr. Horia Petrache

Department of Physics

Approved by:

Dr. Ricardo Decca

For my parents

ACKNOWLEDGMENTS

- IUPUI PT group for insightful discussions
- Dr. Joseph Suelzer for experimental training and laying the groundwork for all that follows in this report
- My advisors for their immense knowledge, help, and (most importantly) their patience
- My family for their continuing support

TABLE OF CONTENTS

LIST OF TABLES

LIST OF FIGURES

ABBREVIATIONS

SCL	Semiconductor Laser
PT	Parity-time
VND	Variable neutral density filter
LK	Lang and Kobayashi
EP	Exceptional points
PA	Phase accumulation
SOW	Sideband oscillation width
SOA	Sideband oscillation amplitude

ABSTRACT

This research investigates characteristics of PT (parity-time) symmetry breaking in a system of two optically-coupled, time-delayed semiconductor lasers. A theoretical rate equation model for the lasers' electric fields is presented and then reduced to a 2x2 Hamiltonian model, which, in the absence of time-delay, is PT-symmetric. The important parameters we control are the temporal separation of the lasers (τ), the frequency detuning ($\Delta\omega$), and the coupling strength (κ). The detuning is experimentally controlled by varying the lasers' temperatures, and intensity vs. $\Delta\omega$ behavior are examined, specifically how the PT-transition and the period and amplitude of sideband intensity oscillations change with κ and τ. Experiments are compared to analytic predictions and numerical results, and all are found to be in good agreement. Eigenvalues, eigenvectors, and exceptional points of the reduced Hamiltonian model are numerically and analytically investigated, specifically how nonzero delay affects existing exceptional points.

1. INTRODUCTION

This chapter gives a brief introduction to semiconductor laser operation and the relatively new field of PT (parity-time) symmetry. The work presented in this paper utilizes a system of coupled semiconductor lasers (SCLs) to provide a test bed for investigating the effects of time-delay on an optical PT-symmetric system. We outline some previous work in PT-symmetric optics and discuss how the content of this research fits within the theoretical and experimental studies of this field.

1.1 Semiconductor Lasers (SCLs)

Soon after the demonstration of the first optical laser in 1960 by Theodore Maiman, the laser was described as "a solution looking for a problem". Indeed, many "problems" have been studied over the past 60 years which have been elegantly solved with the help of this relatively new technology. A significant number of Nobel Prizes have been handed out to work involving lasing, even as recently as Arthur Ashkin's 2018 prize in Physics for optical tweezers [1]. Semiconductor lasers in particular provide a wonderful test bed for nonlinear dynamics due to their sensitivity to optical feedback and their phase and amplitude coupling [2]–[5].

In semiconductor lasers, light is generated by recombination of electron-hole pairs in the active region of a forward-biased p-n junction. As seen in Fig. 1.1, the applied voltage across the junction forces the electrons in the n-region toward the p-region, and the holes move in the opposite direction [6]. This influx of electron-hole pairs constitutes the SCL gain mechanism, and the cleaved facets of the SCL itself form an optical cavity. With the two necessary components for lasing – gain and optical feedback – the light inside the active region is coherently amplified by the process of stimulated emission. SCLs are widely used in many industrial applications due to their small size, high efficiency, and low threshold current requirement. The GaAlAs diodes we use in our experiments have an active region

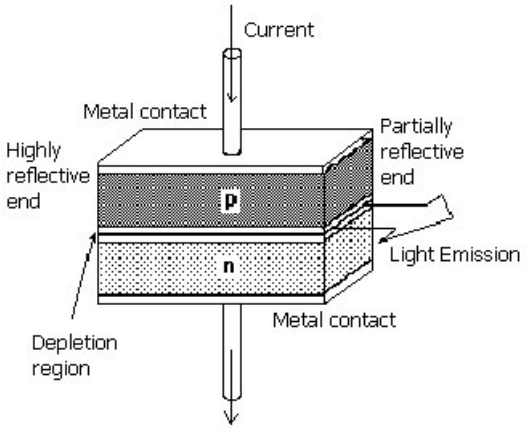

Figure 1.1. Schematic diagram of a semiconductor laser. A forward voltage is applied across a p-n junction, and the light emission from the laser is due to electron-hole pairs in the junction region. The semiconductor material's cleaved facets form an optical cavity, resulting in stimulated emission.

thickness on the order of 0.1-10μm, and the semiconductor material has lateral dimensions on the order of 0.1 - 1mm. Such diode lasers are commonly used for fiber communications, optical data storage, and for pumping other solid-state lasers.

One of the most important features of semiconductor lasers is a unique phase-amplitude coupling. In 1982 Charles Henry investigated the theory of SCL linewidths, which at the time were on the order of 10 times higher than predicted [7]. His work showed that the linewidth broadening was explained by a factor of $1 + \alpha^2$, where α (now referred to as the linewidth enhancement factor) is defined as the coupling between SCL phase and amplitude. Explicitly, α is given by

$$\alpha = \frac{\Delta\mu_R}{\Delta\mu_I}, \tag{1.1}$$

where $\Delta\mu_{R,I}$ is the change in the real and imaginary parts of the SCL's refractive index with respect to carrier density [6], [7]. We'll see the effect of this α factor on laser dynamics when we present our SCL rate equations in chapter 2.

In this report we will investigate the effects of time-delayed coupling in the form of bidirectional injection between two SCLs. The phenomenon of time-delayed optical feedback

in semiconductor lasers has been studied extensively [2]–[5], [8]–[12], with a focus on laser stability and chaotic intensity behavior. In 1986 Tkach and Chraplyvy carried out an investigation into the effects of optical feedback for various delay times and feedback rates, defining five distinct regimes with well-defined transitions [13]. Previous work in our group at IUPUI involved spectrally filtered, time-delayed SCL feedback [12].

Our current work involves the implementation of time-delayed SCL feedback in the context of PT-symmetry, a relatively new area of quantum mechanics. Therefore the results presented here will be couched more in the language of PT-symmetry than in nonlinear SCL dynamics. Specifically, we investigate time-averaged steady-state laser intensities, where much of the chaotic behavior and relaxation phenomena associated with SCL feedback is washed-out. A brief introduction to PT-symmetry and its relation to optics will now be presented.

1.2 PT-symmetry in Optics

There has been considerable interest in recent years concerning a new class of non-hermitian Hamiltonians which may yield real eigenvalues under certain conditions [14]–[24]. These Hamiltonians are know as Parity-Time (PT) symmetric Hamiltonains, and are often used to describe open quantum systems with gain and loss. In standard quantum mechanics there is a requirement that all operators representing physical values must be hermitian, as this guarantees real eigenvalues (observables), unitary evolution, and probability/energy/particle conservation. However, in 1998 Carl Bender and his graduate student Stefan Boettcher discovered that this requirement was too strict, and that there are Hamiltonians which permit real eigenvalues despite not exhibiting hermitian symmetry [14]. This novel class of Hamiltonains has the property that they remain unchanged under simultaneous parity (P) and time (T) reversal operations – in other words, the PT operator commutes with the Hamiltonian H: $[H\ PT] = 0$. The parity operation has the effect of reversing the system in space ($x \rightarrow -x$, $p \rightarrow -p$), and the time operation reverses the system in time

$(t \to -t)$. The fundamental interest in PT-symmetry arises from the ability to extend quantum mechanics to open systems and complex space, where non-hermiticity is associated with energy and probability dissipation [15], [25]–[28].

Interestingly, these Hamiltonians can be moved from regions of real to complex eigenvalues by tuning a parameter that characterizes the system's non-hermiticity. The regime of real eigenvalues is referred to as the PT-unbroken region, where the eigenvectors commute with the PT operator, and the regime of complex eigenvalues is referred to as the PT-broken region, where the eigenvectors no longer commute with the PT operator. The ability to steer a PT-symmetric system between these regions has important applications in the field of optics, such as laser physics[29]–[31] and synthetic optical isolators [32]. This system phase change is known as the PT-transition and is typically marked by an exceptional point, which is a simultaneous eigenvalue and eigenvector degeneracy. These transition points and their properties have been extensively explored in nuclear physics [33], quantum chaotic systems [34], and coupled microwave cavities [35]. Exceptional points have been of great interest in optics over the past few years (see [36] and the references therein). In particular, EPs can be exploited for enhanced sensing – if a PT-symmetric system is operated near an EP with n degeneracies, then a small perturbation ϵ will result in a signal response on the order $\epsilon^{1/n}$, as opposed to a linear response in a hermitian system.

To demonstrate some basic features of PT-symmetry in optics we now present a simple 2-state example system. In 2009 Guo et al. presented an implementation of PT-symmetry in two coupled optical waveguides [37]. One channel was optically pumped to produce an electric field gain γ while the other channel experienced natural attenuation at the same rate $-\gamma$. The physical proximity of the channels provided a transverse evanescent coupling κ. Light was injected longitudinally into the waveguides and the output intensity was observed.

Their work showed that the paraxial wave equation for the electric fields in the waveguide can be written as a 2x2 Hamiltonian model, given by

$$\mathrm{i}\begin{pmatrix} \frac{dE_1}{dt} \\ \frac{dE_2}{dt} \end{pmatrix} = \begin{pmatrix} i\gamma & \kappa \\ \kappa & -i\gamma \end{pmatrix} \begin{pmatrix} E_1 \\ E_2 \end{pmatrix}, \tag{1.2}$$

where E_i are the electric fields in each channel. This set of coupled rate equations is reminiscent of the Schrödinger equation, which is why the 2x2 matrix in Eq. (1.2) is referred to as the system "Hamiltonian". This Hamiltonian, while non-hermitian, is in fact PT-symmetric. In the language of matrix mechanics the P operator swaps the Hamiltonian's diagonal elements and the T operator performs complex conjugation [38]. Under this combined operation the Hamiltonian in Eq. (1.2) remains invariant.

The eigenvalues of the Hamiltonian will determine each channel's intensity output, as solutions for E_i are given by $E_\mathrm{i} \propto \mathrm{e}^{\mathrm{i}\lambda t}$; thus, real and complex eigenvalues will produce dramatically different intensity behavior. The Hamiltonian's eigenvalues are easily obtained: $\lambda = \pm\sqrt{\kappa^2 - \gamma^2}$. Depending on the relative values of the diagonal and off-diagonal elements γ and κ the system can be moved between regions of real and imaginary eigenvalues. Real eigenvalues will generate bounded intensities, and imaginary eigenvalues will lead to exponentially divergent intensities. The PT-transition marks the phase transition between these regions, and is precisely when $\gamma = \kappa$. At this point the corresponding eigenvalues become degenerate with $\lambda = 0$, and the eigenvectors become parallel at this location as well (marking an exceptional point). We therefore expect completely different intensity results depending on the ratio γ/κ.

Example intensity profiles are given in Fig. 1.2. These intensities were generated by numerically integrating Eq. 1.2. The top row shows waveguide intensity for the case of $\gamma < \kappa$ (Fig. 1.2a) and for $\gamma > \kappa$ (Fig. 1.2b). We see that depending on the ratio of γ/κ the system does in fact exhibit dramatically different behavior. An alternate way of examining this phenomenon is to plot the waveguide intensity as a function of the ratio γ/κ, where the

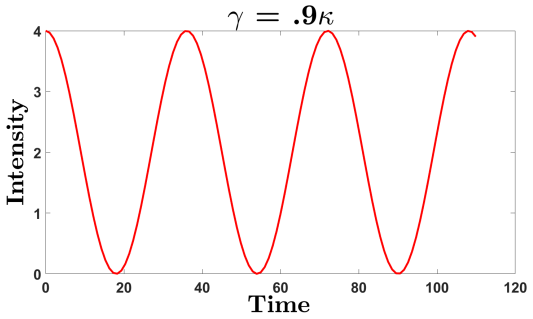

(a) Waveguide intensity vs. time for $\gamma < \kappa$

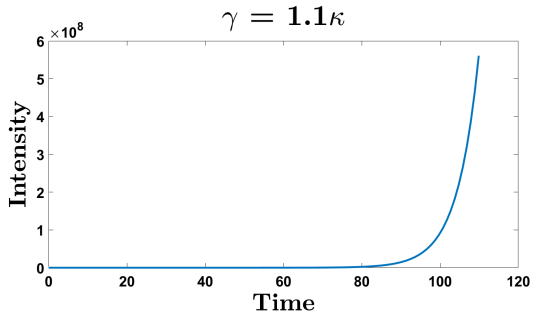

(b) Waveguide intensity vs. time for $\gamma > \kappa$

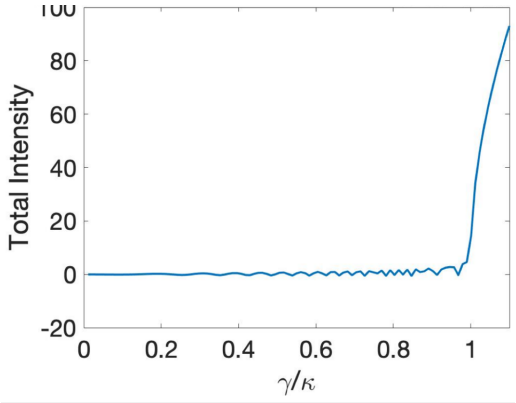

(c) Waveguide intensity vs. γ/κ. The total intensity in the system is probed after some fixed time t and plotted as a function of γ/κ. There is a clear phase transition from bounded to divergent behavior at the PT-transition ($\gamma = \kappa$).

Figure 1.2. Intensity profiles for the waveguide system. The top row shows intensity vs. time and the bottom plot is intensity vs. γ/κ.

system's intensity is probed after a fixed time t and recorded as a function of this parameter ratio. It's clear from Fig. 1.2c that there is a phase transition at $\gamma/\kappa = 1$ (at the PT-transition) from bounded to divergent intensity behavior. In the next chapter we begin our investigation into the effects of time-delay on a system similar to this one.

1.3 Our contribution

In this report we present our contribution to the field of PT-symmetric optics – namely, an investigation of how time-delay affects a traditionally PT-symmetric system. The development of the model and experimental procedure was carried out by Dr. Joseph Suelzer in 2015 during his time as a graduate student in this group. To our knowledge there has been no outside work done on the implementation of time-delay or delayed coupling in the context of PT-symmetry, although studies in nonlinear dynamics and coupled semiconductor lasers have often included delay in various implementations [39], [40]. However, these studies were often concerned with instantaneous laser intensity and carrier dynamics; in this work we examine the time-averaged laser intensities and are not concerned with transient or chaotic responses of the SCL fields and carrier inversion. We will show that a system of two bidirectionally coupled semiconductor lasers can be configured in a manner that produces intensity behavior reminiscent of a PT-symmetric dimer. Rate equations are presented and reduced to a 2x2 pseudo-Hamiltonian rate model, describing the evolution of lasers 1 and 2. This model is completely PT-symmetric in the absence of time-delay. However, when nonzero delay is introduced the system is no longer PT-symmetric, though it does retain key features of PT-symmetry – a phase change between bounded and divergent intensity outputs. Our system has several advantages over traditional PT-symmetric implementations in optics, those being the easy control of the coupling strength between lasers and a relatively easy experimental implementation, using only "off-the-shelf" equipment [37].

Specifically, we analytically describe three key features of the SCL intensity profiles as a function of important system parameters (time delay, coupling strength, and the frequency

detuning between the lasers). These features are (1&2) the width and amplitude of broad intensity oscillations when the laser frequency detuning is larger than the coupling strength and (3) the location of the PT-transition. The oscillation features are important because they arise solely due to nonzero time delay, and are not present in the zero-delay PT-symmetric regime. The effect of delay on the PT-transition is also interesting because there has been no previous study regarding this phenomenon. We then present numerical and experimental observations of these features and how they are affected by time delay and coupling strength. Good agreement is found between the theory, numerical results, and experimental data. Finally, we investigate the exceptional points of the system and how they are affected by nonzero delay. This work is more exploratory than goal-oriented, as we are effectively "going in blind". As stated before, to our knowledge the effects of time-delay have not been studied in the context of PT-symmetry.

The thesis is outlined as follows: In Chapter 2 we present our system, the full rate equations which describe the laser dynamics, and a reduced analytic model for SCL electric fields. The experimental setup and measurement procedures are also discussed. In Chapter 3 we investigate the width of delay-induced broad intensity oscillations. Chapter 4 concerns the amplitude of these oscillations. Chapter 5 presents work done on characterizing the effect of time-delay on the PT-transition. Chapter 6 is an investigation of the analytic model's eigenvalues, eigenvectors, and exceptional points. We then conclude with a brief summary in Chapter 7.

2. MODEL AND EXPERIMENTAL SETUP

2.1 Introduction

The system we use to investigate time-delayed PT-symmetry is composed of two semiconductor lasers in which light from each laser is injected into the active region of the other (see Fig. 2.1). The lasers are operated such that they are completely identical except for their free-running output frequencies, the difference being on the order of 50GHz. A time-delayed coupling arises naturally in this system due to the physical separation between the lasers. Light from SCL1 is not "felt" by SCL2 until it has traveled the cavity distance between the laser facets, and this injected light then influences the laser dynamics in SCL2. The delay time τ is comparable to the characteristic time scales involved in the laser dynamics (carrier and photon lifetimes), and thus cannot be neglected. We will see that time-delay introduces a novel complexity into an otherwise simple PT-symmetric system. The strength of the mutual coupling κ is controlled via a variable neutral density (VND) filter placed between the lasers.

In this chapter we will begin by introducing a rate equation model that describes the evolution of the SCL electric fields and carrier inversions. We will then, with reasonable assumptions, reduce these equations to resemble pseudo-Hamiltonian dimer model for the

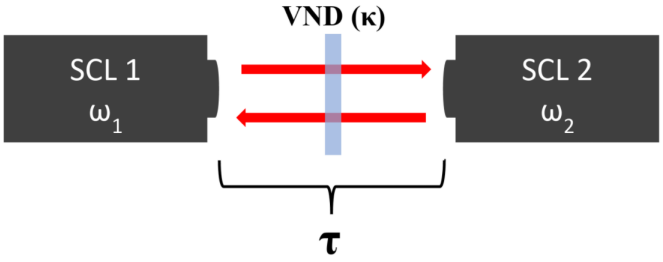

Figure 2.1. Simple diagram of our system. Two lasers, operating at frequencies ω_i, are coupled via mutual optical injection. Due to their physical separation there is an inherent time-delay τ. The coupling strength κ is easily controlled with a variable neutral density (VND) filter.

SCL electric fields. A brief introduction to the intensity dynamics will be presented based on each model. Finally, the experimental setup will be presented and discussed.

2.2 Model

2.2.1 Rate Equation (LK) Model

We use a modified version of the well-known Lang-Kobayashi (LK) SCL rate equation model to describe the evolution of the lasers' electric fields E and carrier inversions N [41]. This is a phenomenological model that has been shown to faithfully simulate semiconductor laser behavior across many systems [42]–[49]. This model can also be derived from fundamentals (Maxwell's equations) [42]. The four coupled nonlinear rate equations are as follows:

$$\frac{dE_1}{dt} = (1 + i\alpha)N_1(t)E_1(t) + i\Delta\omega E_1(t) + \kappa e^{-i\theta\tau}E_2(t-\tau), \tag{2.1a}$$

$$\frac{dE_2}{dt} = (1 + i\alpha)N_2(t)E_2(t) - i\Delta\omega E_2(t) + \kappa e^{-i\theta\tau}E_1(t-\tau), \tag{2.1b}$$

$$T\frac{dN_1}{dt} = P_1 - N_1(t) - (1 + 2N_1(t)) \mid E_1(t) \mid^2, \tag{2.1c}$$

$$T\frac{dN_2}{dt} = P_2 - N_2(t) - (1 + 2N_2(t)) \mid E_2(t) \mid^2, \tag{2.1d}$$

where $E_{1,2}$ are the electric field amplitudes, $N_{1,2}$ are the carrier inversions above threshold for each laser, $P_{1,2}$ are the pump currents above threshold, α is the linewidth enhancement factor, τ is the time delay, κ is the coupling strength (taken to be equal for both lasers), and T is the ratio of the carrier lifetime (1ns) to the photon lifetime (10ps). All timescales are in units of the SCL photon lifetime, 10ps. This model assumes that the two lasers are identical and operate on a single longitudinal mode but have slightly different optical frequencies $\omega_{1,2}$. The relative detuning between them is given by $\Delta\omega = (\omega_1 - \omega_2)/2$, and the rate equations are written in a frame that is rotating at the average frequency of the lasers, $\theta = (\omega_1 + \omega_2)/2$. This model is valid for weak coupling, neglects multiple feedback reflections, and assumes

Table 2.1. Typical values for various parameters

Quantity	Symbol	Scaled value
Linewidth enhancement factor	α	5
Coupling strength	κ	0 - 0.5
Cavity length	τ	0-500
Ratio of carrier to photon lifetime	T	100
Pump rate	P	1.03

that both lasers have identical gain coefficients despite a slight difference in their optical frequencies. The $\exp(-i\theta\tau)$ term accounts for the phase accumulation as light propagates from one laser to the other. The two PT parameters are the coupling strength κ and the frequency detuning $\Delta\omega$. Typical parameter values are given in Table 2.1, where all units are scaled according to Ref. [49].

The first term in equations 2.1a&b accounts for the growth/decay of the E field, depending on the sign and size of N. The imaginary piece $i\alpha$ causes a phase shift due to the linewidth enhancement factor α. The term containing $\Delta\omega$ describes the frequency pulling effect felt by the lasers, and the final term describes the delayed coupling between the two fields. For equations 2.1c&d the first term is the pump rate, the second term is spontaneous emission, and the third accounts for stimulated emission and gain saturation.

Typical intensity results generated by these equations is given in Fig. 2.2a&b, which shows the intensities of both lasers versus the frequency detuning between them for two different delay values. The left plot is for zero time delay, and shows the SCL instantaneous intensity (blue) and the time-averaged intensity (red) for $\kappa = 0.02$. These intensity profiles are obtained by numerically integrating the four delay-coupled rate equations using a Runge-Kutta 4th order algorithm, in which the delay term is evaluated by storing and recalling the electric field values depending on the delay time τ. We choose a set of parameters κ, τ, θ, and $\Delta\omega$, integrate the rate equations for some time t until a steady state is reached, average over 10ns, and then record the intensity values of each laser. By doing this for many values of detuning we can generate the plots seen in Fig. 2.2. Ultimately we are

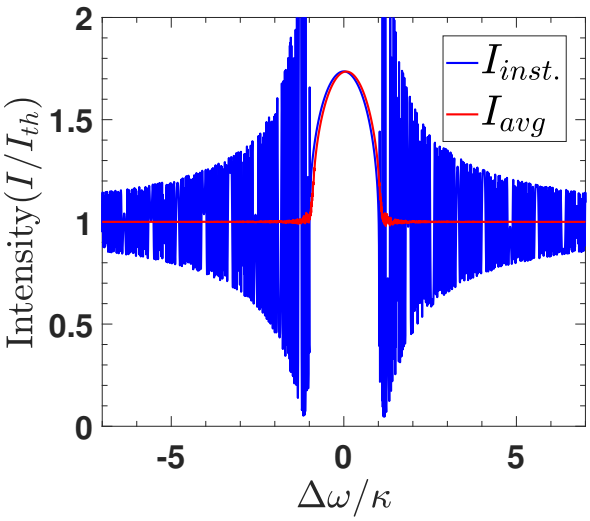

(a) Instantaneous (blue) and average (red) intensities for $\kappa = 0.02, \tau = 0$, and $\theta = 0$ as a function of $\Delta\omega/\kappa$. Both SCL1 and SCL2 share the same intensity profiles.

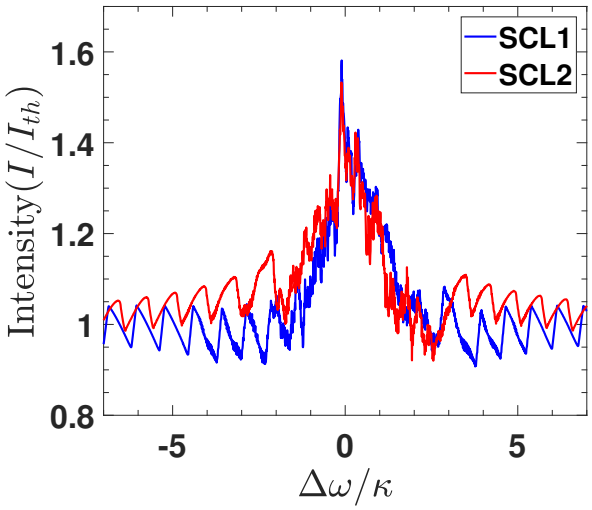

(b) Average intensities for SCL1 (blue) and SCL2 (red) for $\kappa = 0.02, \tau = 200$, and $\theta = 0$ as a function of $\Delta\omega/\kappa$. The two lasers do not share the same intensity profile, but they are quite similar.

Figure 2.2. Numerical intensity solutions from the LK rate equations as a function of $\Delta\omega/\kappa$. In the absence of delay (left) the average intensity sits at threshold for large $\Delta\omega/\kappa$ and diverges for small $\Delta\omega/\kappa$. Similarly, for nonzero delay (right) the average intensity for both lasers oscillates about threshold for large $\Delta\omega/\kappa$ and diverges for small $\Delta\omega/\kappa$, retaining the key features of PT-symmetric behavior.

interested experimentally observable intensities, and so we average the intensities over 10ns to mimic experimental detector response (red curve). In all plots to follow we only show the *average* intensities. When $|\Delta\omega| > \kappa$ there are rapid bounded intensity oscillations, and when $|\Delta\omega| < \kappa$ the laser intensities do not oscillate and instead saturate to levels above threshold ($I/I_{th} = 1$). For zero delay both SCL1 and SCL2 share the same intensity profiles. This mirrors the waveguide behavior seen in Section 1.2, though the regions in which we see these behaviors is reversed. This is due to the fact that our system is defined to be anti-PT symmetric, as will be discussed in the following subsection.

For nonzero delay the results are given in Fig. 2.2b. The delay does alter the intensity profiles, but the overall behavior remains largely the same, namely that beyond $|\Delta\omega|/\kappa = 1$ the average intensity values are bounded near threshold and within $|\Delta\omega|/\kappa = 1$ the intensity values saturate to a level above threshold. We still observe an abrupt increase in the intensities of the lasers near $\Delta\omega = \kappa$. For the zero delay case this transition is *exactly* at $\Delta\omega = \kappa$; we will explain this fact when we discuss the analytic model. Additionally, for nonzero delay there are oscillations in the intensity as the detuning is increased — these are referred to as sideband oscillations, and they are a direct result of the delayed coupling. Note that these are not *time* oscillations, but rather transitions of steady state intensities from above to below some average intensity level.The properties of these oscillations will be discussed in Chapters 3 and 4. The delay also has the effect of widening the central "dome", the region of intensity saturation above threshold. This detuning range for which the intensities remain above threshold is referred to as the domewidth, and will be discussed in Chapter 5. For zero delay the domewidth is exactly $2\Delta\omega/\kappa$ (see Fig. 2.2a), but for nonzero delay it appears that the transition is larger than $2\Delta\omega/\kappa$ (see Fig. 2.2b). These two delay-induced features, the sideband oscillations and the widening domewidth, are the main focus of this work.

The phase accumulation term is of great importance when it comes to the analytic predictions discussed in later chapters. Ideally, an experiment could be constructed such that the phase accumulation term $\theta\tau$ is an integer multiple of 2π, effectively eliminating the

term from the rate equations. This would simply involve tuning either the laser frequencies or the delay time so that the product $\theta\tau$ is exactly 2π. We will refer to this configuration as "zero PA", or no phase accumulation, as $\theta\tau$ would be 0 modulo 2π. Another possible configuration would be if the average frequency θ were some nonzero constant θ_0. This is referred to as the "static PA" case, a generalization of the zero PA case. There is no significant difference between these two cases when it comes to the impact on intensity dynamics. Finally, in the experiment we have what is known as "variable PA", where the phase accumulation depends on the frequency detuning $\Delta\omega$. This arises from the fact that experimentally we fix one laser's frequency while the other is actively swept over some frequency range; using the definition of θ we can write $\theta = \omega_2 + \Delta\omega$, where ω_2 is the SCL2 static frequency. This configuration makes the resulting equations much more complicated, as we will see later. When discussing experimental, theoretical, and numerical work we must include both the static and variable cases of PA in order for proper comparison.

Figure 2.3 shows the impact of phase accumulation on intensity dynamics. For static PA both lasers exhibit sideband oscillations, but for variable PA only the laser whose frequency is changed (SCL1, blue) exhibits sideband oscillations. Furthermore, the period of these sideband oscillations is different between the two cases. The overall shape of the central dome is minimally affected, but it is unclear visually how the domewidth is impacted. These effects will be investigated in later chapters.

While the LK rate equations are useful for numerically simulating the experimental system, they are too complicated to provide insight into the dependence of the sideband oscillations and domewidth on system parameters. It's also unclear how this system reduces to a PT-symmetric one in the absence of delay. We now present a reduced model that, with reasonable approximations, allows for analytic solutions concerning these delay-dependent phenomena.

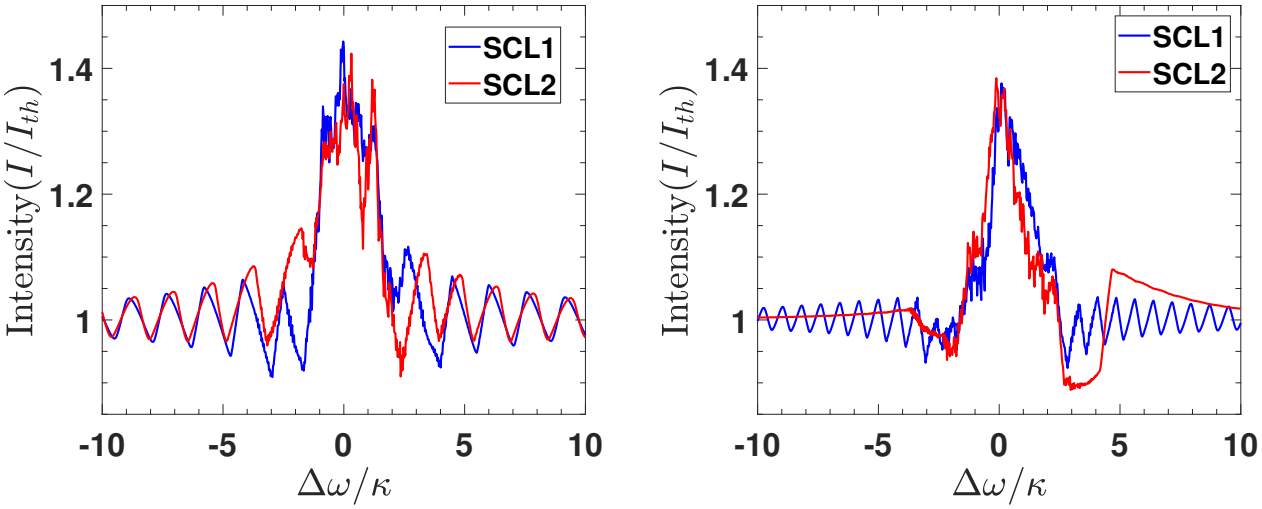

(a) Numerical intensities for $\kappa = 0.02, \tau = 100$, and $\theta = 0$. This is the "zero" PA case. Notice that both lasers exhibit sideband oscillations beyond $\Delta\omega = \kappa$.

(b) Numerical intensities for $\kappa = 0.02, \tau = 100$, and $\theta = \omega_2 + \Delta\omega$. This is the "variable" PA case. Notice that only the laser whose frequency is swept (blue) exhibits sideband oscillations beyond $\Delta\omega = \kappa$. The intensity of SLC2 (red) is static in this region.

Figure 2.3. Numerical intensities vs. $\Delta\omega/\kappa$ for zero (left) and variable (right) phase accumulations. The variable case corresponds to the experimental method.

2.2.2 Analytic Model

In order to massage the LK equations into something that resembles the 2x2 waveguide Hamiltonian model in Eq. (1.2), we first make the assumption that the lasers are operating in a steady state and are pumped just above the threshold required for lasing. This means that the population inversion above optical transparency is very close to zero ($N_{1,2} \approx 0$) and that the carrier inversion does not change significantly in time. Thus, the carrier rate equations 2.1c&d can effectively be ignored. Next, in steady state operation the average value of the electric fields will not change significantly in time, and together with an assumption that the field solutions $E_{1,2}$ can be written as $e^{\lambda t}$ the delay terms $E_{1,2}(t-\tau)$ can be expressed as $E(t)e^{-\lambda\tau}$, where λ are the system's eigenvalues. This substitution results in a pseudo-2x2 rate equation model for the SCL electric fields $E_{1,2}$:

$$\begin{pmatrix} \frac{dE_1}{dt} \\ \frac{dE_2}{dt} \end{pmatrix} = \begin{pmatrix} i\Delta\omega & \kappa e^{-\lambda\tau}e^{-i\theta\tau} \\ \kappa e^{-\lambda\tau}e^{-i\theta\tau} & -i\Delta\omega \end{pmatrix} \begin{pmatrix} E_1 \\ E_2 \end{pmatrix}, \tag{2.2}$$

which resembles the Hamiltonian representation of the waveguide example in Section 1. The effective Hamiltonian $\mathcal{H}$ is given by the 2x2 matrix in the above equation. Our new analytic model, though, is slightly different from the waveguide model in two ways – first, it is missing the i in front of the $\frac{dE_{1,2}}{dt}$ terms. This separates our system from a traditional Schrödinger equation found in quantum mechanics and traditional PT-symmetry. The lack of an i actually makes our system *anti*-PT symmetric; however, for the purposes of this report we do not emphasize this difference. In the context of all to follow, the only difference between traditional PT-symmetry and anti-PT symmetry is that in our system real eigenvalues will correspond to exponentially changing laser intensities, and imaginary eigenvalues correspond to bounded intensities. We also emphasize that while this reduced model may resemble a 2x2 dimer, it is actually *infinite* dimensional due to the inclusion of the eigenvalue λ inside the effective Hamiltonian. We will investigate the effects of nonzero delay on the characteristic equation in the following chapters.

In the case of zero delay the effective Hamiltonian reduces to that of a simple PT-symmetric dimer (Eq. (1.2)),

$$\begin{pmatrix} \frac{dE_1}{dt} \\ \frac{dE_2}{dt} \end{pmatrix} = \begin{pmatrix} i\Delta\omega & \kappa \\ \kappa & -i\Delta\omega \end{pmatrix} \begin{pmatrix} E_1 \\ E_2 \end{pmatrix}. \tag{2.3}$$

We now see that the diagonal gain term in Eq. (1.2) is replaced by the frequency detuning $\Delta\omega$, and the coupling term κ is on the off-diagonal. Unlike the coupled waveguide system where the coupling is determined by the physical proximity of the channels, our setup allows for easy, continuous control of κ via the VND. Furthermore, in our system the "gain" term $\Delta\omega$ is always exactly equal and opposite for the two lasers, and we do not have to worry about tuning the gain and attenuation rates such that they are equal in magnitude. The effective Hamiltonian in Eq. 2.3 has eigenvalues $\lambda = \pm\sqrt{\kappa^2 - \Delta\omega^2}$, which are plotted in Fig. 2.4. Depending on the magnitudes of the diagonal and off-diagonal elements the eigenvalues can either be purely real or purely imaginary, resulting in divergent or bounded intensity behavior, respectively. Comparing this eigenvalue plot to the zero-delay intensities in Fig. 2.2a we see that the region of intensity saturation above threshold corresponds to the region of real eigenvalues, while the region of fast oscillations about threshold corresponds to the region of imaginary eigenvalues. In other words, for zero-delay the system is perfectly PT-symmetric, and this is reflected both in the analytic model and the LK model where there is considerably more complexity.

2.3 Experimental Setup

As stated before, our attempt to capture SCL intensity behavior as a function of frequency detuning has the advantage of being low-cost and having low-complexity when compared to other optical PT-symmetric investigations. The experimental schematic is given in Fig. 2.5. We use Hitachi HL7851G GaAlAs laser diodes with multi-quantum well structures, which have free-running single-mode frequencies near 782nm. An HP optical spectrum analyzer

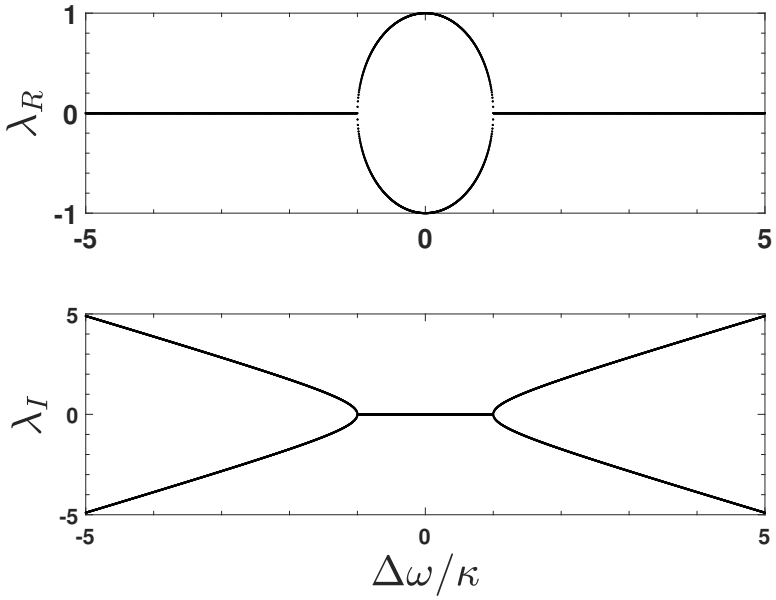

Figure 2.4. Eigenvalues of the effective Hamiltonian in Eq. (2.3). The real parts are plotted on the top row and the imaginary parts are plotted on the bottom row, all as a function of $\Delta\omega/\kappa$. There is a clear phase transition at the location $\Delta\omega/\kappa = 1$, which explains the corresponding phase transition at this location in Fig. 2.2a.

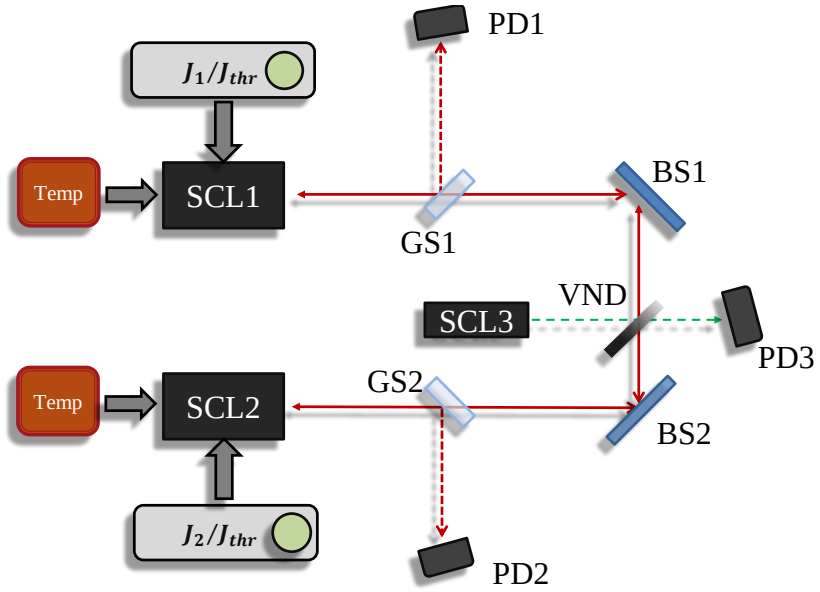

Figure 2.5. Experimental setup. The SCLs are controlled by current and temperature controllers. GS: glass slide, BS: beam splitters, VND: variable neutral density filter, PD: photodiodes. A third SCL is used to characterize the transmission through the VND and hence measures the value of κ.

and a 2GHz Fabry-Perot analyzer are used to observe the mode structure of each laser, ensuring that both operate in the single-mode regime. Light is emitted from each laser and directed into the active region of the other laser. The SCLs are identical except for their operating temperatures and optical frequencies. The output of these diodes is regulated via current and temperature controllers, which stabilize the injection current and allow for continuous control of the SCL operating temperatures. Pump currents and temperatures can be set to within accuracies of 0.1mA and 0.01°C, respectively. The frequency of the SCL output is dependent on the operating temperature, and thus we can easily and continuously control the frequency detuning between the lasers by sweeping over one laser's operating temperature range. By measuring the external distance between the diodes we can measure the delay time τ. The coupling strength κ is defined theoretically as

$$\kappa = \frac{(1-r^2)}{r\tau_{\text{in}}}\xi\tau_p, \tag{2.4}$$

where r is the laser facet reflectivity, ξ^2 is the transmitted optical power through the VND, τ_p is the photon lifetime, and τ_{in} is the internal laser round-trip lifetime. By monitoring the transmitted power through the VND via a third SCL and photodiode (SCL3 in Fig. 2.5) we can calculate the exact value of κ. However, due to the relative sizes of the incoming beam profile ($>100\mu m$) and the laser active region ($10\mu m$), only a portion of the incoming light is actually coupled into the laser. This mismatch results in a phenomenologically consistent reduction of κ by a factor of 10, $\kappa_{\text{e}ff} = 0.1\kappa_{theory}$, which is included in all coupling strengths in this report [50]. The glass slides (GS) reflect a portion of light to be sent to 1GHz photodiodes (PD), and their signals are sent to a 1GHz oscilloscope.

In order to generate intensity plots comparable to those seen in Fig. 2.3b we experimentally detune the two lasers by continuously changing the temperature of one laser while keeping the other fixed. The PID settings on the temperature controller allow for adjustment of the actual temperature trajectory, as unlike the pump current controller the laser's operating temperature does not respond to changes instantaneously. For changes in temperature

less than 4°C the frequency dependence of the laser on temperature is comfortably assumed to be linear:

$$\omega_1(T) = \omega_{1_0} - k_T T, \tag{2.5}$$

where k_T is experimentally determined to be 153GHz/°C. This is determined by using an optical spectrum analyzer with 0.001nm resolution to measure SCL wavelength for various temperature settings. This was also verified by using a fixed 2GHz free spectral range Fabry-Perot etalon. If the laser is swept through a fixed temperature range ΔT, n number of peaks will be observed in the etalon, and k_T is therefore $k_T = (2GHz)n/\Delta T$.

Due to our inability to exactly detune each laser in an equal and opposite manner such that their average value $\theta = (\omega_1 + \omega_2)/2$ is a constant, we must compare all experimental results to the analytic and numerical cases of variable PA, where θ depends on $\Delta\omega$. Perhaps with more precise equipment a static phase accumulation could be achieved experimentally.

Figure 2.6 shows a typical experimental intensity plot as a function of $\Delta\omega/\kappa$. The frequency of SCL1 is slowly swept over a suitable range, and the intensities are recorded via the oscilloscope. The oscilloscope voltages are then turned into intensity values with a Matlab program. The detuning is swept with a rate 153GHz/(5sec) so that there are no transient responses from the lasers. In Fig. 2.6 we see that the laser whose frequency is swept (blue) exhibits sideband oscillations outside of $|\Delta\omega/\kappa| = 5 - 6$, and that there is a clear phase transition from bounded to unbounded intensities near this value. SCL2 does not oscillate but still exhibits this phase transition at the same value. Compared with Fig. 2.3b (variable PA LK solution) there is overall good agreement between the features in both plots.

The experimental work reported here concerns the measurement of the period and amplitude of the sideband oscillations as the delay and coupling are varied, as well as the measurement of the central domewidth, the region of exponential growth and decay when $|\Delta\omega| < \kappa$. Each set of experimental results will be reported in the corresponding chapters.

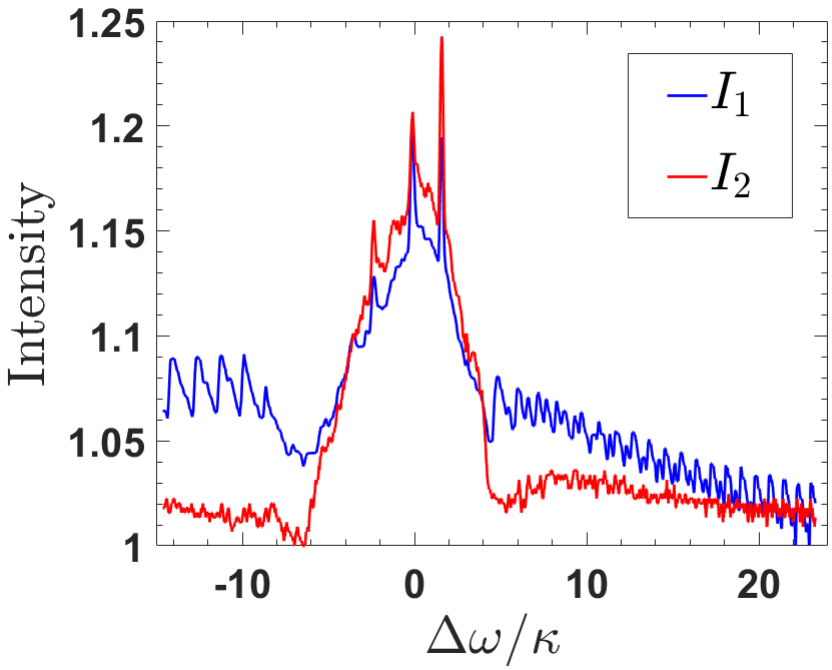

Figure 2.6. Experimental intensity vs. $\Delta\omega/\kappa$ for $\tau = 180$ and $\kappa = 0.008$. Intensities for SCL1 are in blue and SCL2 is in red. The main feature of PT-symmetry is present here, even with all experimental complications: a phase transition near $\Delta\omega = \kappa$. This plot also shows sideband oscillations only for the laser whose frequency is swept (blue), in agreement with Fig. 2.3b.

3. SIDEBAND OSCILLATION WIDTH

3.1 Introduction

We have seen that the introduction of time-delay in our system results in several observable effects on the intensity behavior, most importantly the creation of sideband intensity oscillations when $|\Delta\omega|/\kappa > 1$ and a widening of the PT-transition near $|\Delta\omega|/\kappa = 1$. We will attempt to explain the features associated with these delay-dependent phenomena using an analytic approach based on a simplified system model. An investigation of the validity of that analysis will be carried out using a more complicated numerical model and with experimental data. To begin, we'll start with the sideband oscillation width (SOW), the period of the broad time-averaged intensity oscillations in the region $|\Delta\omega|/\kappa > 1$. This period is defined as the detuning gap between successive intensity transitions from above to below the threshold value (see Fig. 3.1). The specific reason for this somewhat obtuse definition will become clear in Section 3.2. Since the SOW is defined in frequency space (i.e. detuning, a frequency, is the x-axis of Fig. 3.1), we choose to refer to this quantity simply as SOW in order to avoid confusion. Of course, in real experimental units the SOW is a frequency (Hz). The value of the SOW actually changes depending on oscillation number, although this effect is hard to notice visually, and the SOW saturates to a steady value when the detuning is far from the central dome. The SOW in particular has given us the best results when comparing the analytic solution to the numerical and experimental data.

This chapter will be organized as follows. First, an analytic prediction will be derived for the cases of zero and variable PA using an eigenvalue analysis based on the reduced Hamiltonian model. The eigenvalues of the pseudo-Hamiltonian will be evaluated by separating the real and imaginary parts, and the features of these eigenvalues will be discussed. This will lead to an expression of the SOW as a function of $\kappa\tau$, and then both numerical and experimental results will be presented and discussed. We find that there is excellent agreement between the three scenarios (Hamiltonian model, numerical model, and experiment).

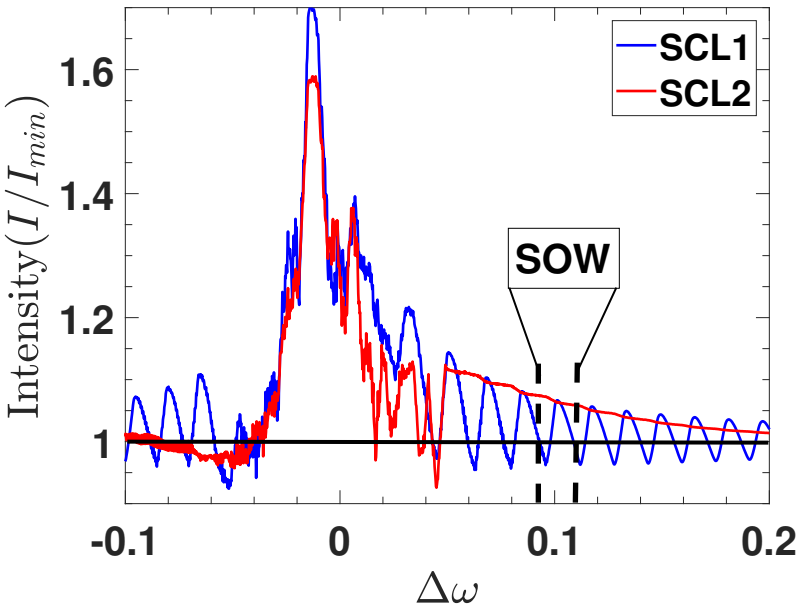

Figure 3.1. Typical intensity vs. detuning plot for variable PA, $\kappa = 0.02$ and $\tau = 100$. The sideband oscillation width (SOW) is defined as the detuning gap between intensity transitions from above to below threshold ($I/I_{th} = 1$, horizontal black line), as indicated in the figure with black dashed lines.

3.2 Eigenvalue Analysis (FG Equations)

In order to understand the origins of the sideband oscillations and to see how their widths depend on system parameters, we begin with the most simple model for our system, the pseudo-2x2 Hamiltonian model for the lasers' electric fields. This model ignores carrier inversion dynamics and assumes that the lasers are operating in the steady state regime. The two coupled rate equations, derived from the LK rate equations, are given as follows:

$$\begin{pmatrix} \frac{dE_1}{dt} \\ \frac{dE_2}{dt} \end{pmatrix} = \begin{pmatrix} i\Delta\omega & \kappa e^{-\lambda\tau} e^{-i\theta\tau} \\ \kappa e^{-\lambda\tau} e^{-i\theta\tau} & -i\Delta\omega \end{pmatrix} \begin{pmatrix} E_1 \\ E_2 \end{pmatrix}, \tag{3.1}$$

where E_{i} are the lasers' electric fields, $\Delta\omega$ is the frequency detuning, κ is the feedback strength, τ is the delay time, and θ is the average laser frequency $(\omega_1 + \omega_2)/2$. Due to the time-delay the eigenvalue λ is present inside the Hamiltonian, which will give us some trouble when attempting to explicitly solve the characteristic equation. We again stress that this is an i*nfinite*-dimensional system due to the time-delay.

3.2.1 Eigenvalues as a Prediction of SCL Intensity

Ultimately we are interested in i*ntensity* behavior, as this is what will be measured in the lab. Why are we then starting with the system's eigenvalues? The answer is simple. In the derivation of Eq (3.1) we make the assumption that solutions for the electric field can be written as $E(t) \propto e^{\lambda t}$. By definition the lasers' intensities are $I(t) = |E(t)|^2$; therefore the behavior of λ ultimately determines the behavior of the lasers' intensities. However, now we must address the complication of infinitely many eigenvalues associated with Eq. (3.1). If there are infinitely many λ, how does each solution affect the overall intensity? It turns out that for our system only the eigenvalues with the *greatest real parts* determine the intensity behavior. Each eigenvalue λ represents a mode in each laser's electric field evolution. The infinite modes do not combine linearly, as the Hamiltonian model is nonlinear due to the time-

delay. It is reasonable to say that the mode with the largest real part will ultimately dominate the laser's behavior, as a large real part drives that particular mode toward saturation faster than any other mode. We are not concerned with the imaginary parts, as these result in fast temporal electric field oscillations, and will ultimately be averaged out by the detectors.

This assumption can be tested numerically. Figure 3.2 shows the correspondence between the eigenvalues with the largest real part and numerical laser intensity for similar parameters. In the top row we show the real parts of the eigenvalues with the largest real parts as a function of $\Delta\omega/\kappa$. The red/blue regions correspond to regions where $\mathrm{Re}(\lambda)$ are positive/negative, which signify regions of electric field growth/decay. Because of the nonlinearities and saturation present in both the LK model and in the physical system, exponential growth/decay from positive/negative eigenvalues can't continue forever. For positive/negative eigenvalues the laser intensity will grow/decay to a higher/lower intensity value compared to the threshold level, which is defined as the intensity in the absence of SCL coupling ($\lambda = 0$). This can be seen by comparing the top row of Fig. 3.2 to the bottom row, where the overall shape of the intensity curves mimic the eigenvalue curves. Notice that the sideband oscillations arise due to the eigenvalues crossing from positive to negative, and that the detuning locations that mark this transition are shared in the intensity plot.

3.2.2 Characteristic Equation

Now that we have demonstrated that the SCL intensities are effectively determined by the eigenvalues with the largest real parts, we can begin our eigenvalue analysis. The ultimate goal is to solve for the width of the sideband oscillations. We'll begin by evaluating the characteristic equation of the Hamiltonian in Eq. (3.1):

$$\lambda^2 + \Delta\omega^2 - \kappa^2 \mathrm{e}^{-2\lambda\tau}\mathrm{e}^{-2\theta\tau} = 0 \tag{3.2}$$

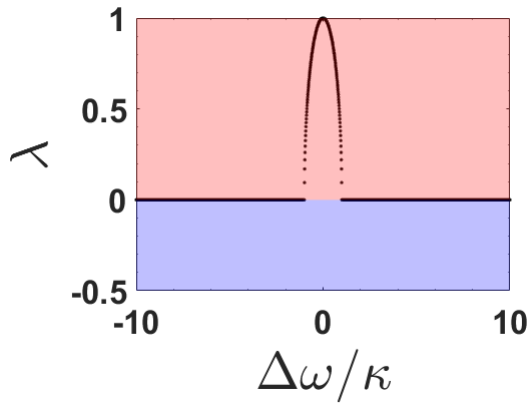

(a) Eigenvalues with largest real part as function of $\Delta\omega/\kappa$ for zero delay. Only the real part of λ is plotted. The system is completely PT-symmetric in this regime, eigenvalue solutions are either purely imaginary or purely real. The red region corresponds to positive Re(λ) and the blue region is negative Re(λ).

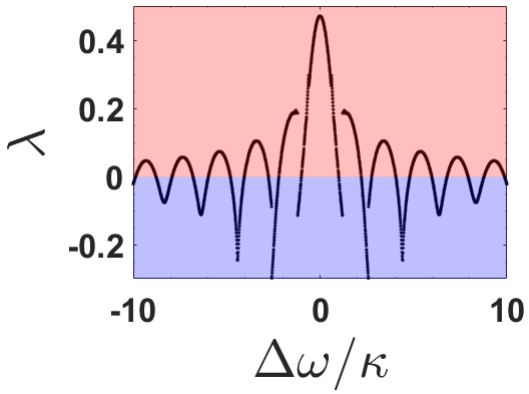

(b) Eigenvalues with largest real part as function of $\Delta\omega/\kappa$ for nonzero delay ($\tau = 80$). Only the real part of λ is plotted. For nonzero delay there are regions where λ is complex and where Re(λ) is negative. The red region corresponds to positive Re(λ) and the blue region is negative Re(λ).)

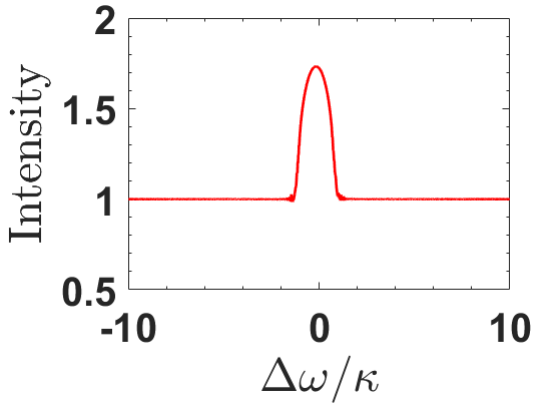

(c) Intensities for same parameters as Fig. 3.2a. Both lasers share the same intensity profile. For zero delay the system is PT-symmetric, hence the phase transition at $\Delta\omega/\kappa = 1$. The intensities never dip below 1, which is the laser steady-state intensity in the absence of coupling.

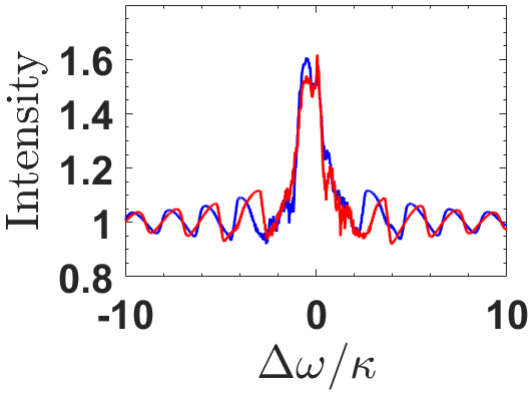

(d) Intensities for same parameters as Fig. 3.2b. For nonzero delay the intensities may dip below 1. Notice how the sideband oscillations line up with the above eigenvalue plot.

Figure 3.2. Correspondence between eigenvalues (with largest real part) and SCL intensity. The top row shows the real part of eigenvalues with largest Re(λ) generated from the Hamiltonian in Eq. (3.1). The red/blue regions correspond to positive/negative Re(λ), i.e. regions where the overall intensity saturates above/below threshold. The bottom row shows numerical SCL intensity generated from the LK rate equation model. All four plots have the x-axis as detuning scaled by the coupling strength. Notice how the shape of each eigenvalue plot is mirrored by the corresponding intensity plot. Only the eigenvalues with the largest real parts significantly affect intensity behavior.

Solutions of this equation are the system's eigenvalues. We cannot obtain a closed-form solution for λ, which means we will have to find a more clever way to get what we're after. Unfortunately, λ is generally complex, which means we cannot graph the eigenvalues directly and see the dependence on $\Delta\omega$. What we do is the following: write the eigenvalues as $\lambda = \lambda_R + \mathrm{i}\lambda_I$ and separate Eq. (3.2) into its real and imaginary parts. Each resulting *real* equation can then be plotted, and the intersections of the two will be the eigenvalue solutions. By making this substitution we arrive at the following important equations:

$$F(\lambda_R, \lambda_I) = \Delta\omega^2 + \lambda_R^2 - \lambda_I^2 - \kappa^2 \mathrm{e}^{-2\lambda_R\tau}\cos(2\tau(\lambda_I + \theta)) = 0 \tag{3.3a}$$

$$G(\lambda_R, \lambda_I) = 2\lambda_R\lambda_I + \kappa^2 \mathrm{e}^{-2\lambda_R\tau}\sin(2\tau(\lambda_I + \theta)) = 0, \tag{3.3b}$$

where F contains the real parts of Eq. (3.2) and G contains the imaginary parts. The behavior and shape of each equation is intricately linked to the system's overall intensity behavior, as we will see. A thorough understanding of these equations will provide great insight into the system's behavior.

Figure 3.3 shows two sets of typical F and G curves for zero (left) and nonzero (right) phase accumulation. The F and G equations will be discussed in great detail in Chapter 6, so for now we will describe the features relevant for the sideband and domewidth analyses. First, it's important to note that except in the case of variable PA, only the F equation depends on $\Delta\omega$. As the detuning is swept the F equation's two "antennae" branches, the branches that shoot off to $\mathrm{Re}(\lambda = +\infty)$, shift up along the vertical axis. These "antennae" curves, wherever they intersect the G curve, generate the eigenvalues with the greatest real part (i.e. the intersections furthest to the right for any given detuning). Both the F and G curves have "finger" branches that come in from $\mathrm{Re}(\lambda) = -\infty$, approach the vertical axis, and then return to $\mathrm{Re}(\lambda) = -\infty$. These "fingers" are numbered by their appearance above and below the horizontal axis (see Fig. 3.3a). Notice how the G curve undulates about the vertical axis – this curve will be important to the sideband analysis. Static phase accumulation has the effect of breaking the symmetry of each curve across the x-axis, but

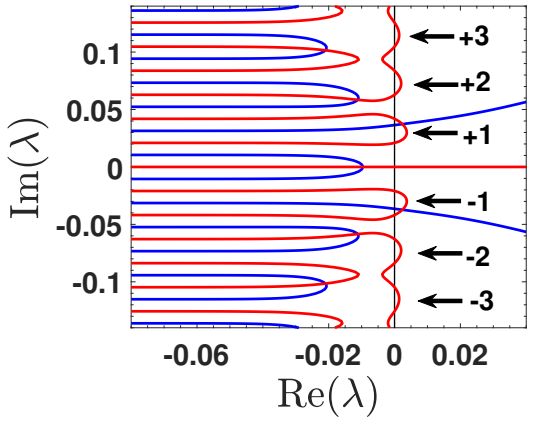

(a) F (blue) and G (red) curves for $\Delta\omega = 0.04$, $\tau = 75$, $\kappa = 0.02$, and $\theta = 0$. Black arrows label the G "fingers".

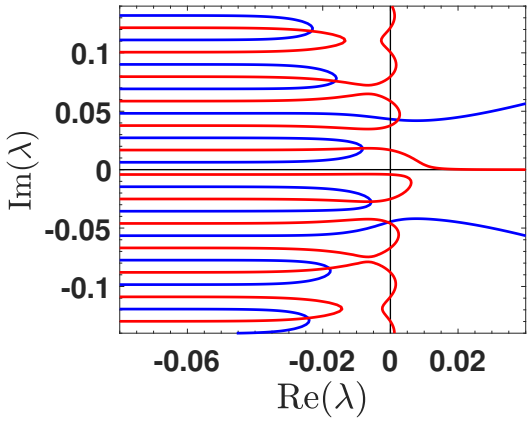

(b) F (blue) and G (red) curves for $\Delta\omega = 0.04$, $\tau = 75$, $\kappa = 0.02$, and $\theta = 0.025$. Notice how the nonzero phase *theta* breaks the symmetry across the x-axis.

Figure 3.3. F (blue) and G (red) curves plotted for various parameters. The x-axis is Re(λ) and the y-axis is Im(λ). Intersections of the two curves are solutions to Eq. (3.2). The left plot is for zero PA and the right plot is for nonzero PA. The spacing of the "fingers", or the branches that protrude from Re(λ) = $-\infty$, have the vertical spacing $\pi/2\tau$.

the overall behavior is quite similar (Fig. 3.3b). In fact, for eigenvalue solutions far from the x-axis the two cases are nearly identical.

As the detuning is increased from zero, the topmost F "antenna" solution will move upward intersect *every* part of G that lies to the right of the vertical axis for some detuning. This means that the real part of the rightmost intersection will cross from positive to negative whenever the G curve crosses the vertical axis. We know from examining Fig. 3.2 that the SCL intensities will also cross from above to below threshold when the eigenvalues cross from positive to negative – therefore, if we can solve for the locations where G intersects the Im(λ) axis we will then know where the intensities cross their threshold value.

3.2.3 SOW Analytic Solution

The following SOW theoretical analysis was first carried out by Dr. Yogesh Joglekar for the case of zero phase accumulation. My contribution was to extend the analysis to nonzero

phase accumulation, both static and variable, as well as a special case of variable frequency pulling (section 3.5).

In order to obtain an analytic expression for the SOW we first require a solution for detuning locations where G intersects the vertical axis ($\mathrm{Re}(\lambda) = 0$). Setting $\lambda_R = 0$ in Eq. (3.3b) results in the following relation:

$$\kappa^2 \sin(2\tau(\lambda_I + \theta)) = 0 \tag{3.4}$$

which has solutions $\lambda_I = \frac{n\pi}{2\tau} - \theta$, where n corresponds to the n_{th} crossing of the vertical axis. Plugging this back into the F equation yields the detunings for which these crossings occur:

$$\Delta\omega_n = \pm\kappa\sqrt{(-1)^n + \frac{(n\pi)^2}{(2\kappa\tau)^2} + \frac{\theta^2}{\kappa^2} - \frac{n\pi\theta}{\kappa^2\tau}}. \tag{3.5}$$

Now, we are looking for the period between successive crossings from positive to negative $\mathrm{Re}(\lambda)$ (or negative to positive). This means we can define the sideband width as $\mathrm{SOW}{=}\kappa\Big(\Delta\omega_{2n+2} - \Delta\omega_{2n}\Big)$. We choose the even n to simplify the calculations, but we can also use odd n – the important part is that we take the difference between every *other* $\Delta\omega_n$.

To evaluate the SOW we need to carry out a difference between two square root terms. For demonstration purposes we'll set the phase accumulation θ to zero in order to simplify calculations. The problem is this:

$$\mathrm{SOW} = \kappa\sqrt{(-1)^{(2n+2)} + \frac{((2n+2)\pi)^2}{(2\kappa\tau)^2}} - \kappa\sqrt{(-1)^{(2n)} + \frac{((2n)\pi)^2}{(2\kappa\tau)^2}}, \tag{3.6}$$

which cannot be simplified for arbitrary n. However, in the limit of large n (i.e. oscillations far from the central dome) we can rearrange some terms and make the binomial approximation to get rid of the square roots. This results in the following solution for the SOW:

$$\mathrm{SOW} = \frac{\pi}{\tau} - \frac{1}{2}\frac{\kappa^2\tau}{\pi n(n+1)}. \tag{3.7}$$

There are a few interesting consequences of this expression. First, when n (which is proportional to the oscillation number) is large, the SOW saturates to the value $\boldsymbol{\pi}/\tau$, which is *independent* of κ. This means that far from the central dome the sideband oscillations have a constant period. Second, the SOW is inversely proportional to the delay time. Both of these predictions can easily be checked numerically and experimentally. The final feature of the SOW solution is that the period of oscillation increases with n until it saturates; this is somewhat hard to see, even in the numerical solution (Fig. 3.1). However, since large n is required for this solution to hold, this feature is not investigated further. Interestingly, by performing the same calculation with nonzero θ we arrive at the same asymptotic solution for the sideband width: SOW $= \boldsymbol{\pi}/\tau$. Thus the SOW is not affected by static phase accumulation (at least for large n). Of course, for the case of static PA both SCL1 *and* SLC2 oscillate with the same sideband period, and the two lasers share this same SOW prediction.

Amazingly, this same method can be used to obtain a closed solution for the SOW in the case of *variabl*e PA. Variable PA is defined as $\theta = \theta_0 + \Delta\omega$, which corresponds to the physical scenario where one laser's frequency is swept while the other remains fixed. Because the detuning is present inside the phase accumulation term the resulting F and G equations become much more complicated; however, by following the above procedure to find $\Delta\omega_n$ the following solution is obtained:

$$\Delta\omega_n = \frac{\kappa^2(-1)^n}{\left(\frac{n\boldsymbol{\pi}}{\tau} - 2\theta_0\right)} + \frac{1}{4}\left(\frac{n\boldsymbol{\pi}}{\tau} - 2\theta_0\right). \tag{3.8}$$

Taking the difference $\Delta\omega_{2n+2} - \Delta\omega_{2n}$ results in a similar expression for the SOW:

$$\text{SOW} = \frac{\boldsymbol{\pi}}{2\tau} - \frac{\kappa^2\boldsymbol{\pi}}{\tau}\left[\left(\frac{(n+1)\boldsymbol{\pi}}{\tau} - \theta\right)\left(\frac{n\boldsymbol{\pi}}{\tau} - \theta\right)\right]^{-1}. \tag{3.9}$$

Thus, in the same limit of large n, the SOW has the asymptotic value $\boldsymbol{\pi}/2\tau$, which is exactly *half* the period of the static PA case. In fact, all of the three predictions concerning the

SOW from the static case apply to the variable case, with the only difference being a factor of 2 in the asymptotic solution. We'll encounter this factor of 2 again when analyzing the sideband oscillation amplitude. For the variable PA case only *on*e laser expresses sideband oscillations; however, the analytic prediction provides only *on*e prediction value, $\pi/2\tau$. In other words, this analytic method cannot explain or predict the fact that SCL2 does not oscillate. This is just something to keep in mind, as we'll find a more robust way of solving for the SOW in section 3.5. It's important to note that Eq. (3.7) is not a limiting case of Eq. (3.9), since each expression comes from a fundamentally different system setup.

Now that we have an analytic prediction we can check the SOW both numerically and experimentally, looking for 1) a constant period independent of the coupling strength and 2) an inverse relation between SOW and the delay time.

3.3 Numerical Results

The above predictions were first investigated numerically. In short, the analytic prediction is e*xactly* reproduced by the rate equation model. Figure 3.4 contains two intensity profiles that encapsulate these results. For the case of zero PA, two different intensity curves are plotted, one (blue) for $\kappa = 0.04$ and one (magenta) for $\kappa = 0.02$. Both plots have the same delay ($\tau = 100$), and only SCL1's intensity is shown. The first prediction of Eq. (3.7) is that the sideband oscillation width should be independent of the coupling strength. Indeed, by examining the period of oscillation for the blue and magenta curves it's obvious that the two curves share the same sideband period when sufficiently far from zero detuning. In fact, n only needs to be around 5-6 for this to hold true. This phenomenon was checked for many different combinations of $\kappa\tau$, and the result was always the same: the numerical SOW does not depend on κ for large n. The coupling strength only affects the amplitude of the oscillations. This result also holds for the case of variable PA.

Next, the dependence of the sideband oscillation width was checked as a function of the delay time. In Fig. 3.4 the SOW is measured to be 0.0315, which is extremely close to

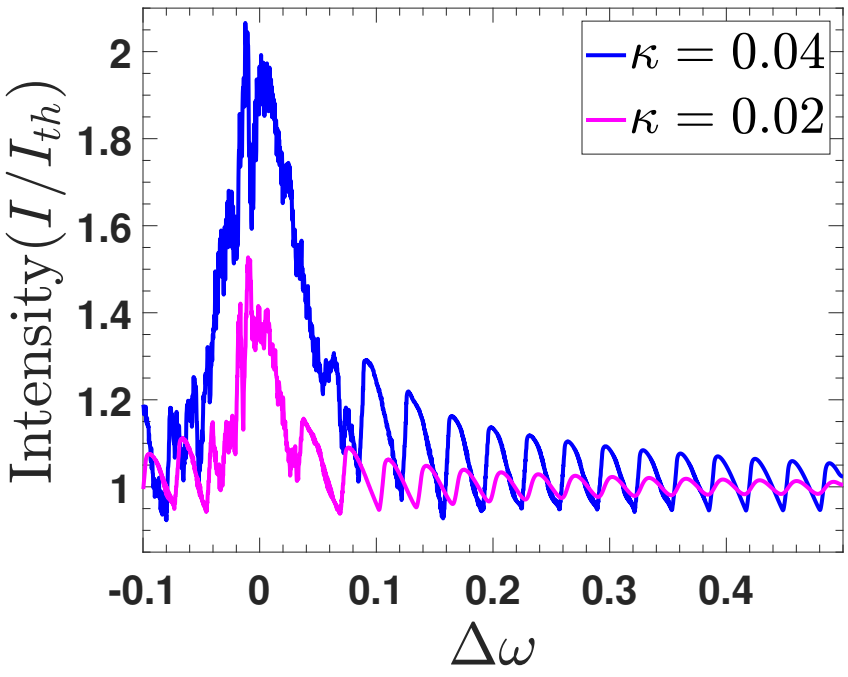

Figure 3.4. Intensity vs. detuning for two values of κ generated by integrating the LK rate equations. Only SCL1's intensity is plotted. In this plot $\tau = 100$ and $\theta = 0$. The blue curve is for $\kappa = 0.04$, while the magenta plot is $\kappa = 0.02$. The numerical data reproduces both predictions made by Eq. (3.7), namely that the SOW is independent of κ (the period of the blue and magenta curves is equal for large n) and that the SOW is equal to π/τ.

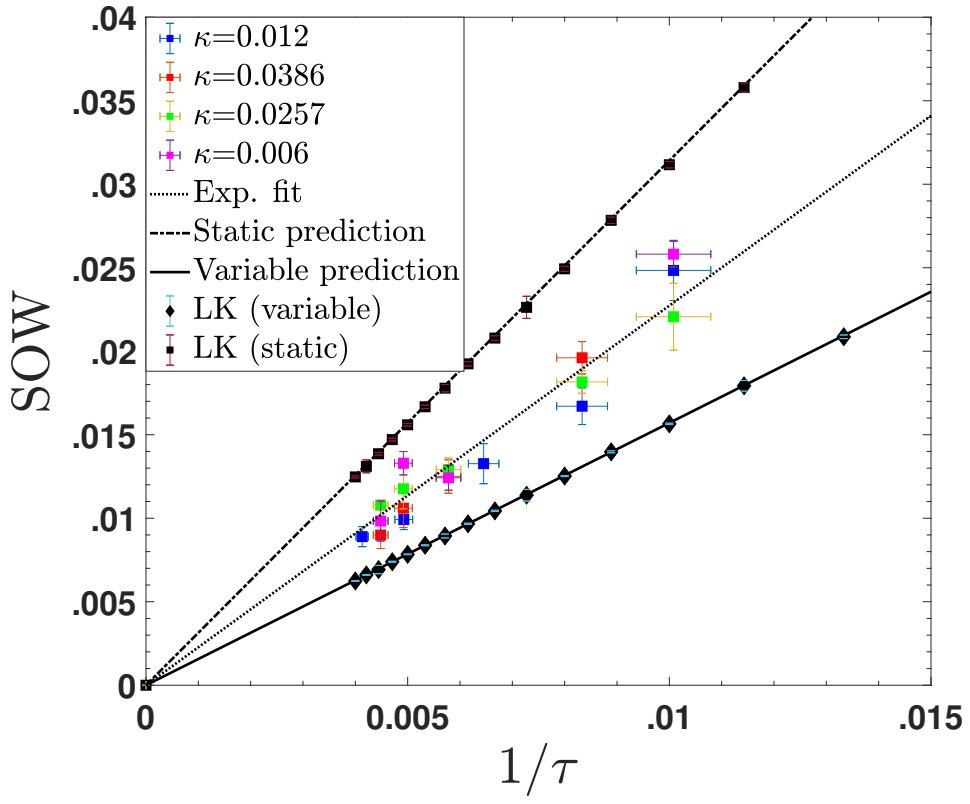

Figure 3.5. Numerical and experimental results for SOW as a function of $1/\tau$. The black squares/diamonds are numerical data from integrating the LK equations in the cases of static (square) and variable (diamond) phase accumulation. The dash-dotted line indicates the analytic prediction for static PA and the solid black line indicates the analytic prediction for variable PA. The colored data points are experimental data, and the colors correspond to different values of κ (see legend). The dotted line is the experimental fit.

the predicted value of $\boldsymbol{\pi}/\tau = 0.03145$. The numerical procedure for SOW measurement is to first generate an intensity plot and then either run an FFT (fast Fourier transform) on the intensity data for SOW frequency or run a peak search algorithm and directly obtain the peak-to-peak detuning widths. Even though both of these methods do not exactly use the definition laid out in section 3.2 (that the SOW is defined as the detuning gap between successive intensity transitions from above to below threshold), the end result is the exact same value.

But does the SOW *change* with the proper inverse τ dependence? The answer is yes – the numerical SOW is inversely related to the delay time τ. Figure 3.5 summarizes the results, where the SOW is plotted as a function of inverse delay time. The black square points are numerical solutions of SOW from the LK equations in the case of static PA, and the dash-dot line is the corresponding analytic prediction of π/τ. It's clear that the numerical data nearly perfectly matches the prediction; in fact, the error bars associated with the numerical measurements are so small that they can barely be seen. The variable PA case is represented by black diamonds (numerical data) and a black solid line (analytic prediction, $\pi/2\tau$). Again the agreement is virtually perfect. This is very surprising, as the LK model is much more complicated than the Hamiltonian model, with nonlineraities and carrier dynamics influencing the SCL intensities. It just goes to show how reasonable our assumptions were when reducing the LK equations to the Hamiltonian model.

3.4 Experimental Results

Now on to the experimental results. The experimental detuning is generated by keeping one laser's frequency fixed and sweeping the other's frequency over some range, which corresponds to the variable PA case. Therefore, we compare all experimental results to Eq. (3.9). The procedure for measuring the experimental SOW is as follows: first, the detuning of laser 1 is swept and an intensity vs. detuning plot is generated for some κ and τ far from the central dome (Fig. 3.6). Generally we capture 20 oscillations in one data set in order to obtain a roust SOW measurement. Next, an FFT is run on the intensity data and the oscillation frequency is determined. The FWHM (full width half max) value of the SOW frequency peak determines the size of the vertical error bars in Fig. 3.5. This frequency is then turned into a proper SOW value and recorded. Alternatively the SOW can be obtained by running a peak search algorithm on the data in Fig. 3.6 and then taking the average of the peak-to-peak detuning widths. This process is repeated for multiple values of κ and τ, and the results of this experiment are given in Fig. 3.5. The colored square points repre-

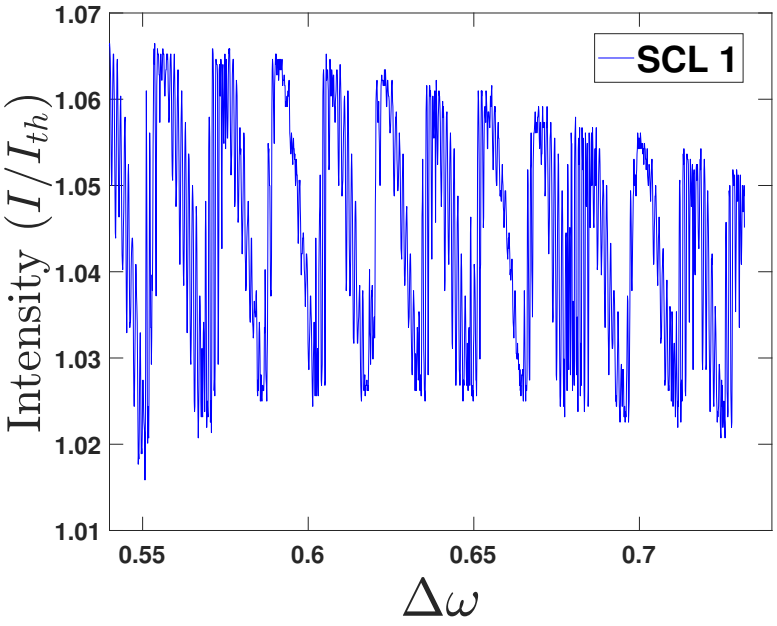

Figure 3.6. Typical experimental SCL intensity as a function of detuning. Only the swept laser's intensity is shown. In this plot $\tau = 138$ and $\kappa = 0.0053$; the phase accumulation is variable. Despite noisy data the SOW can be obtained by both an FFT and by using a peak search program to determine the peak-to-peak oscillation widths. For this plot the SOW=0.16.

sent experimental measurements of SOW as a function of inverse delay $1/\tau$ – the different colors correspond to different values of κ (see figure legend). Horizontal error bars are due to uncertainties in delay measurement. The dotted line is the linear fit of the experimental data.

Let's examine the two main predictions of Eq. (3.9). The first is that the SOW is independent of κ if the oscillations are sufficiently far from the dome. The experimental data confirms this prediction – by examining Fig. 3.5 it's clear that for any given detuning there is no tendency for one set of κ data to lie above/below another. In other words, there is no evidence that the coupling strength consistently affects the value of SOW; otherwise an obvious "color pattern" would be seen on the plot. As for the second prediction, there is great evidence for the inverse dependence of the SOW on the delay time. The experimental

forms a nice linear trend, as indicated by the dotted line in Fig. 3.5. However, the *slope* of this trendline is not equal to either the variable or static PA predictions. Ideally the experimental trend line would have slope $\pi/2$, but it is in fact equal to 2.273, which almost exactly bisects the variable and static predictions! This is evident just by examining the three lines in Fig. 3.5 – the experimental dotted line looks to be halfway between the two analytic predictions. It almost seems too perfect to be coincidence... we'll attempt to explain this in the next section.

In summary, the experimental data confirms the two main predictions associated with the SOW: 1) that the SOW is independent of the coupling strength κ and 2) that the SOW in inversely proportional to the delay time τ. The exact slope of the $1/\tau$ dependence does not exactly match the variable PA prediction, although it is relatively close. What could be causing this discrepancy? There are two experimental complications that could explain the difference:

1. The calibration method used to turn SCL temperature into frequency is not quite linear. As the temperature of each laser is scanned, the center frequency of the single-mode SCLs shift up or down; however, due to the discrete nature of the supported cavity modes the shifting is not perfectly smooth. At certain temperatures the laser mode will "hop" from one wavelength to another, usually only on the order of 0.3nm, but this hopping will affect the detuning calibration used to generate the x-axis in Fig. 3.6. Between mode-hoppings the frequency curves are almost perfectly linear, and we try to choose temperature ranges where there is no apparent mode hopping; however, such delicate detuning measurements can be affected by any inconsistencies in the frequency/temperature relation.

2. The analytic and numerical models assume single-mode SCL operation, and the frequency of each laser is assumed to be independent of the other. There is no frequency pulling in either model. However, it is not unreasonable to expect some degree of influ-

ence of one laser's frequency on the other – these are, after all, coupled oscillators, and by changing one laser's frequency there may be a tangible effect on the other's. This frequency pulling effect would manifest itself in the definition of phase accumulation, which would in turn affect the analytic prediction. Can the value of the experimental data linear fit be explained by adjusting our model to include frequency pulling?

Surprisingly, the second complication – frequency pulling – can be investigated analytically, numerically, and experimentally, which we now present.

3.5 Frequency Pulling

If there is indeed SCL frequency pulling present in the experimental setup we'll need to modify the analytic and numerical models to reflect that. Let's begin with the analytic model. We'll also limit the analysis to *linear* frequency pulling, where the frequency of SCL2 depends linearly on the frequency of SCL1. We'll assume, perhaps non-physically, that this is a non-reciprocal process and that SCL1 is not in turn influenced by SCL2. Explicitly we can write the frequency of SCL2 as

$$\omega_2 = \omega_{2_0} + b\omega_1, \tag{3.10}$$

where ω_{2_0} is the free-running frequency of SCL2 in the absence of coupling (a constant) and b is a parameter that determines the strength of the frequency pulling effect. If b is positive, any positive change in ω_1 will result in ω_2 being "pulled" toward the new ω_1 value. Normally, frequency pulling means that the b parameter is always positive, so the change of ω_2 follows the change of ω_1; however, for this analysis we'll let b take any real value, regardless of the "physicality" of such a constant. We're simply interested in seeing what happens if we let ω_1 affect ω_2.

Using the same definitions of $\Delta\omega = (\omega_1 - \omega_2)/2$ and $\theta = (\omega_1 + \omega_2)/2$ we can generate their "frequency pulled" versions by substituting in Eq. (3.10):

$$\Delta\omega = \frac{1}{2}\Big[(1-b)\omega_1 - \omega_2\Big] \tag{3.11a}$$

$$\theta = \frac{1}{2}\Big[\omega_{2_0} + \frac{(1+b)}{(1-b)}\Big(2\Delta\omega + \omega_{2_0}\Big)\Big] \tag{3.11b}$$

Using these definitions we can then re-do the analysis in section 3.2 where we solve for the detunings for which the F and G branches intersect on the y-axis. The ultimate goal is to analytically solve for the SOW in the case of frequency pulling. In fact, this frequency pulling definition actually includes both the static and variable PA cases – they are built in to the expressions in Eq. (3.11a&b)! If we substitute $b = -1$ we see that the value of ω_2 changes at the same rate as ω_1 but in the opposite direction, such that the quantity θ remains constant. If we then set ω_{2_0} to $n\boldsymbol{\pi}/\tau$ we obtain the zero PA case. Furthermore, if we set $b = 0$ the frequency of ω_2 remains fixed for all values of ω_1; this corresponds to the case of *variable* PA, the experimental case. If we are able to obtain an analytic expression for the SOW in terms of b we can check these limiting cases explicitly.

Starting with the G equation (Eq. (3.3b))and substituting $\lambda_R = 0$ we arrive at the following condition for λ_I:

$$\lambda_I = \frac{n\boldsymbol{\pi}}{2\tau} - \frac{1}{2}\Big[\omega_{2_0} + \frac{(1+b)}{(1-b)}\Big(2\Delta\omega + \omega_{2_0}\Big)\Big]. \tag{3.12}$$

This expression can then be substituted back into the F equation (Eq. (3.3a)) to obtain an expression that we can use to find the detunings $\Delta\omega$ for which there are eigenvalue transitions from positive to negative λ_R:

$$\kappa^2(-1)^n - \Delta\omega^2 + \left[\frac{n\boldsymbol{\pi}}{2\tau} - \frac{1}{2}\Big[\omega_{2_0} + \frac{(1+b)}{(1-b)}\Big(2\Delta\omega + \omega_{2_0}\Big)\Big]\right]^2 = 0. \tag{3.13}$$

Solving this results in a quadratic equation for $\Delta\omega$:

$$\Delta\omega^2\left[-1+\frac{(1+b)^2}{(1-b)^2}\right]+\Delta\omega\left[\frac{(1+b)}{(1-b)}\left(\frac{(1+b)}{(1-b)}\omega_{2_0}+\omega_{2_0}-\frac{n\boldsymbol{\pi}}{\tau}\right)\right]$$
$$+\left[\kappa^2(-1)^n+\frac{n^2\boldsymbol{\pi}^2}{4\tau^2}+\frac{\omega_{2_0}^2}{4}-\frac{n\boldsymbol{\pi}}{2\tau}\omega_{2_0}+\frac{\omega_{2_0}^2(1+b)^2}{4(1-b)^2}+\frac{\omega_{2_0}^2(1+b)}{2(1-b)}-\frac{n\boldsymbol{\pi}}{2\tau}\frac{(1+b)}{(1-b)}\omega_{2_0}\right]=0 \tag{3.14}$$

Needless to say the resulting solution for $\Delta\omega$ is quite messy, and not particularly illuminating by itself. Let's check the limiting cases of static ($b=-1$) and variable ($b=0$) phase accumulation to verify the accuracy of Eq. (3.14). For static PA we set $b=-1$, which results in

$$\Delta\omega_n=\pm\kappa\sqrt{(-1)^n+\frac{(n\boldsymbol{\pi})^2}{(2\kappa\tau)^2}+\frac{\omega_{2_0}^2}{4\kappa^2}-\frac{n\boldsymbol{\pi}\omega_{2_0}}{2\kappa^2\tau}}. \tag{3.15}$$

When writing the phase accumulation $\theta=(1/2)\omega_{2_0}$ from Eq. (3.11b) it's clear that Eq. (3.15) is exactly same as what was obtained before in Eq. (3.5). Thus the same SOW prediction is contained in the general frequency pulling case (Eq. 3.14). How about the case of variable PA? For that situation $b=0$, and Eq. (3.14) simplifies to

$$\Delta\omega_n=\kappa\left[\frac{(-1)^n+\left(\frac{\omega_{2_0}}{\kappa}-\frac{n\boldsymbol{\pi}}{2\kappa\tau}\right)^2}{\frac{n\boldsymbol{\pi}}{\kappa\tau}-\frac{2\omega_{2_0}}{\kappa}}\right]. \tag{3.16}$$

From Eq. (3.11b) we see that for $b=0$, $\theta=\omega_{2_0}$, and with this substitution we recover the exact same detuning solution as in Eq. (3.8). Thus the two main SOW predictions for both static and variable PA are contained in our "universal" frequency pulling model (Eq. (3.14)), which is quite remarkable.

That's all well and good, but our interest for this section lies in positive values of b. For simplicity we'll set $\omega_{2_0} = n\pi/\tau$, which is functionally the same as setting $\omega_{2_0} = 0$. This results in a closed expression for $\Delta\omega_n$ for arbitrary b:

$$\Delta\omega_n = \frac{\kappa(1-b)}{8b}\left[\frac{n\pi}{\kappa\tau}(1+b) \pm \sqrt{\left(\frac{n\pi}{\kappa\tau}\right)^2(1+b)^2 - 16b\left[(-1)^n + \left(\frac{n\pi}{2\kappa\tau}\right)^2\right]}\right] \tag{3.17}$$

Now that we have an expression for the $\Delta\omega$ at which the eigenvalues cross the y-axis we can continue the SOW analysis and find the detuning gap between successive crossings from positive to negative. Again, the SOW is defined as $\Delta\omega_{n+2} - \Delta\omega_n$. Performing this evaluation and taking the limit of large n results in the following expression for the sideband oscillation width:

$$\text{SOW} = \frac{(1-b)}{b}\frac{\pi}{4\tau}\Big((b+1) \pm (b-1)\Big). \tag{3.18}$$

Curiously this expression provides *two* values for the SOW depending on the choice of sign inside the parentheses. These two widths are

$$\text{SOW}_1 = \frac{\pi}{\tau}\frac{1-b}{2} \tag{3.19a}$$

$$\text{SOW}_2 = \frac{\pi}{\tau}\frac{1-b}{2b}. \tag{3.19b}$$

What is the physical interpretation of *two* SOW predictions? Let's check the familiar case of static PA, $b = -1$. Plugging this into Eq. (3.19a&b) we obtain the result $\text{SOW}_{1,2} = \pm\pi/\tau$. We get *two* sideband periods, one positive and one negative, but with the same magnitude. The magnitude matches the prediction found earlier in Eq. (3.7). How about the case of variable PA? By plugging in $b = 0$ we find that $\text{SOW}_1 = \pi/2\tau$ and $\text{SOW}_2 = \infty$. The first value matches what we've seen before in Eq. (3.9), but the second value is $infinity$. With this information we can finally interpret the two values of SOW: the magnitude of one solution of SOW describes the oscillation period of SCL1 and the magnitude of the other SOW solution describes the oscillation period of SCL2. It's unclear what exactly a negative

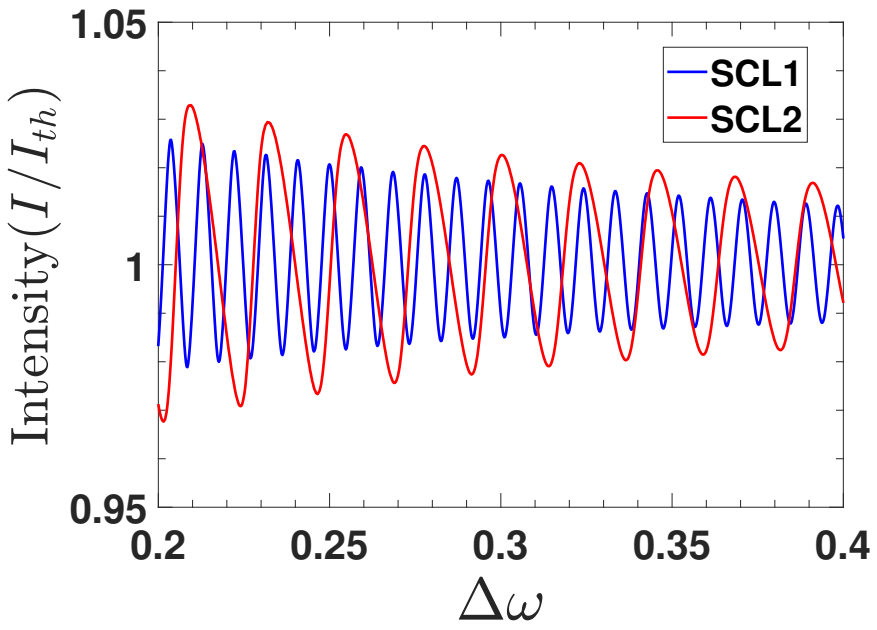

Figure 3.7. Numerical intensities for the case of frequency pulling, with parameters $\tau = 100$, $\kappa = 0.02$, and $b = 0.41$. These intensities show sideband oscillations far from the central dome. Each laser oscillates, but at different frequencies. The blue curve is SCL1 and the red curve is SCL2. The measured SOW are 0.0093 and 0.0227 for SCL1 and SCL2, respectively, which is exactly equal to the analytic prediction.

oscillation width means physically, but the magnitudes are clearly correct. In the static PA case both lasers oscillate with the same period;n the variable PA case one laser oscillates and the other doesn't. Another way of saying SCL2 doesn't oscillate is to say that it's oscillation period is $infinity$. By trying to solve the problem of frequency pulling we've stumbled upon a more robust solution for the SOW, one that can predict the oscillation period of *both* lasers.

Now, the reason we started this investigation was to examine the physical scenario of frequency pulling as it applied to the experimental setup, where b would be a small positive number. If we substitute a value of $b = 0.7$ (arbitrary) into Eq. (3.19a&b) we get the values $\text{SOW}_1 = 0.47/\tau$ and $\text{SOW}_2 = 0.67/\tau$, which means that both lasers oscillate but with different periods. This can be checked numerically by integrating the LK equations. We'll choose a b value such that the experimental slope obtained in Fig. 3.5 is predicted, i.e.

$\mathrm{SOW_i} = 2.273/\tau$. This slope means we choose $b = 0.41$. Both lasers may oscillate in this case, but at least one of them should give us the desired SOW relation.

Figure 3.7 shows a numerical example of this frequency pulling phenomenon. Intensities are generated by integrating the LK equations with parameters $\tau = 100$, $\kappa = 0.02$, and $b = 0.41$. The blue curve is for SCL1 and the red curve is for SCL2. Clearly both lasers oscillate about the threshold intensity value, but their periods are different. The measured SOW are 0.0093 and 0.0227 for SCL1 and SCL2, respectively, which are for all intents and purposes exactly equal to the analytic prediction from Eq. (3.19a&b). An interesting feature of the sideband oscillations is seen in Fig. 3.7, that the amplitude of the sideband oscillations is proportional to the period. This will be discussed in more detail in the following chapter.

Our goal was to explain the altered experimental SOW vs. $1/\tau$ slope with frequency pulling. If this is the explanation then the frequency of SCL2 needs to be pulled by SCL1 at a rate of $0.41\omega_1$. A brief measurement of this pulling was made by measuring the frequency of SCL2 with and without coupling, i.e. with and without light from SCL1 coupled into the active region. No apparent change in frequency was observed. Furthermore, the numerical intensities show that both lasers oscillate with relatively similar amplitudes. If such a frequency pulling was present in the experiment then we should just as easily see the intensity oscillations of SCL2 – however, this is not observed either. Figure 3.8 shows experimental data for the same parameters as in Fig. 3.6, $\tau = 138$ and $\kappa = 0.0053$. The left scale (blue) is for SCL1 (blue curve), and the red scale/curve is for SCL2. Clearly SCL2 does not show any evidence of sideband oscillations, certainly not at the same amplitude as SCL1.

We conclude that there is no good evidence for frequency pulling in our experimental system. However, the analytic solution for arbitrary b provided us with a more robust prediction method for the cases of static and variable PA, in that it allowed for predictions concerning each laser's oscillation widths. It's a bit of a shame, as the experimental trendline in Fig. 3.5 sits so perfectly between the two analytic predictions – it seems to be more than just coincidence. Unfortunately, frequency pulling is not the reason for this discrepancy.

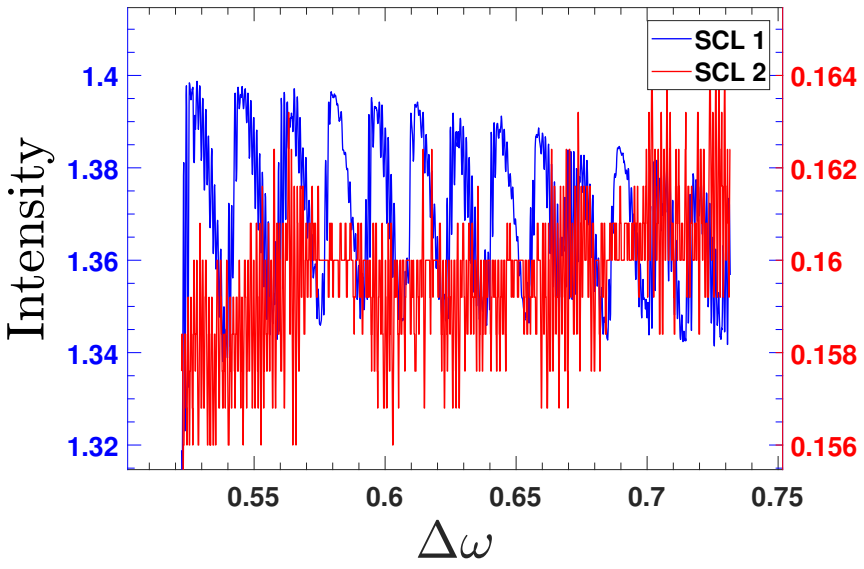

Figure 3.8. Experimental intensities vs. detuning for SCL1 (blue) and SCL2 (red) for $\tau = 138$ and $\kappa = 0.0053$. The intensity scale for SCL1 is on the left in blue, and the scale for SCL2 is on the right in red. There is no evidence of frequency pulling in this experimental data, as the intensity of SCL2 does not appear to oscillate at all.

3.6 Conclusion

We conclude this section by observing that the SOW results give us good reason to trust our eigenvalue approach for explaining intensity behavior. It's remarkable that the Hamiltonian model, which ignores various system nonlinearities and carrier dynamics, is capable of generating robust, closed form predictions for intensity phenomena despite having a transcendental characteristic equation. The numerical data *exactly* reproduces the analytic predictions, and the experimental data also matches the predictions to a very high degree. Next we'll turn to another feature of the delay-induced sideband oscillations – namely, the amplitude and how it depends on system parameters. Again, we are interested these sideband oscillations because they are only present with non-zero time delay, which is the unique built-in feature our system posses.

4. SIDEBAND OSCILLATION AMPLITUDE

4.1 Introduction

Similar to the period of the sideband oscillations, we can obtain analytic predictions about the *amplitud*e as well, specifically the rate at which the oscillation amplitudes increase/decrease with detuning. The sideband oscillation amplitude (SOA) is something that can be easily measured in the lab, and thus will provide another good experimental "check" to investigate the validity of both the pseudo-Hamiltonian model and rate equation models for our system. We define the SOA as the peak-to-trough intensity amplitude of each sideband oscillation (see Fig. 4.1 for reference), and this value can be tracked as a function of various system parameters. Again, the sideband oscillations are of great interest due to the fact that they arise solely due to the time-delay. First an analytic prediction will be made based on the reduced Hamiltonian model, and then numerical and experimental data will be presented concerning these predictions.

4.2 Analytic Solution

Because of the successes we had with the sideband oscillation width, we will again start with the pseudo-2x2 Hamiltonian model for the electric fields. In the lab we ultimately measure the intensity amplitude of the oscillations – therefore, an understanding of the amplitude of the ei*genvalu*e oscillations will allow for comparison, as the steady-state laser electric fields seem to be proportional to the real parts of the eigenvalues. Of course, since we don't know the direct numerical correspondence between eigenvalues and intensities, the following analysis will only provide a prediction for the functional form of the SOA rate of change.

Our road map is straightforward. The sideband oscillation amplitudes can be calculated by subtracting the minima of λ_R from the maxima of λ_R for eigenvalue solutions with the largest real part; if we can find expressions for both then our job is done. In the following

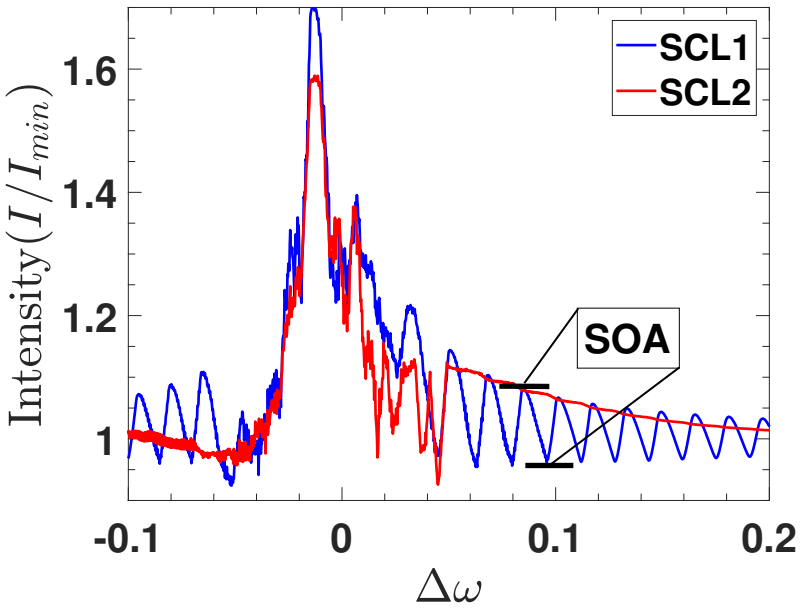

Figure 4.1. Typical intensity vs. detuning plot for variable PA, $\kappa = 0.02$ and $\tau = 100$. The sideband oscillation amplitude (SOA) is defined as the peak-to-trough intensity value for each sideband oscillation, as indicated in the figure with black horizontal bars.

analysis we'll stick with the static phase accumulation case ($\theta = 0$) for simplicity – we'll discover that the variable PA case ($\theta = \theta_0 + \Delta\omega$) is a straightforward extension of the static version.

Let's begin with the λ_R maxima: starting from the F and G equations (whose shared solutions are the system's eigenvalues) it's clear that the λ_R maxima correspond to the horizontal maxima of G, since (for fixed PA) G does not depend on detuning. The F "antennae" branches always intersect the maxima of G for some detuning. To solve for the rightmost values of G we simply evaluate the first derivative of G with respect to λ_I and set the result equal to zero. This gives us two coupled equations for λ:

$$G = 2\lambda_R\lambda_I + \kappa^2 \mathrm{e}^{-2\lambda_R\tau}\sin(2\tau(\lambda_I + \theta)) = 0 \tag{4.1a}$$

$$\frac{dG}{d\lambda_I} = 2\lambda_R + 2\tau\kappa\mathrm{e}^{-2\tau\lambda_R}\cos(2\tau(\lambda_I + \theta)) = 0 \tag{4.1b}$$

Each equation contains the term $\mathrm{e}^{-2\tau\lambda_R}$ – by isolating the term in each equation we find the following relation for λ_I:

$$2\tau\lambda_I = \tan(2\tau(\lambda_I + \theta)). \tag{4.2}$$

This relation, while transcendental, is well approximated by the following:

$$\lambda_I = \frac{(2n+1)\boldsymbol{\pi}}{4\tau} - \theta, \tag{4.3}$$

where n is an integer representing the extrema number starting from the λ_R axis. This approximation works particularly well, since the difference $\Delta\lambda_I = \lambda_{I_{actual}} - \lambda_{I_{approx}}$ will produce some $\Delta\lambda_R$, but at the maxima — by definition — $\Delta\lambda_R$ isn't significant. It's also important to note that this condition is independent of κ.

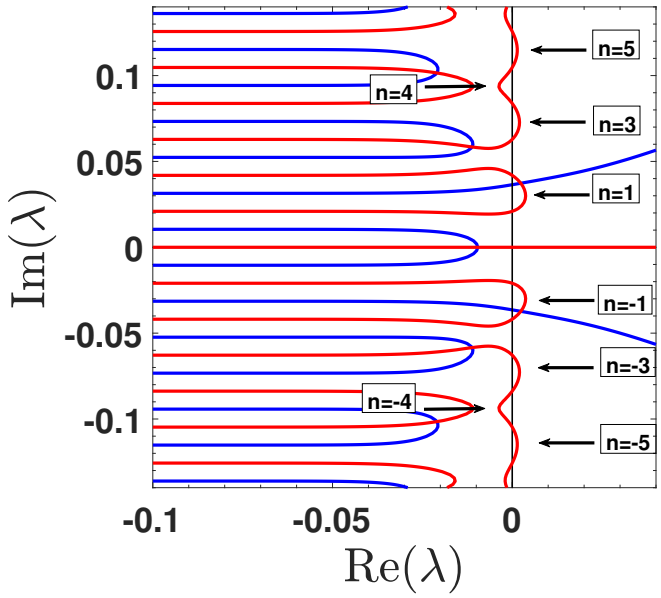

Figure 4.2. Typical F and G plot, with the x-axis representing λ_R and the y-axis λ_I. In this figure $\tau = 75$, $\kappa = 0.02$, and $\theta = 0$. The indices n from Eq. (4.4) are labeled in the figure, and the black arrows point to the maxima to which the indices refer. Notice that there is no $n = 2$, since the G curve is broken at that location.

To find the λ_R for which these maxima occur we simply substitute Eq. (2.3) into Eq. (2.1a), which produces the following relation for λ_R:

$$2\tau\lambda_R e^{2\tau\lambda_R} = \frac{-\kappa^2\tau^2\cos(n\pi)}{\frac{(2n+1)\pi}{4} - \theta\tau} \tag{4.4}$$

Only odd n provide the maxima of λ_R (see Fig. 4.2), and by utilizing the Lambert W function λ_R can be written explicitly as

$$\lambda_{R_{max}} = \frac{1}{2\tau} \mathrm{W}_0\left(\frac{(2\kappa\tau)^2}{(2n+1)\pi - 4\theta\tau}\right). \tag{4.5}$$

The $\mathrm{W}_0(x)$ term is the zeroth branch of the Lambert W function, which is defined as the inverse of xe^x. The Lambert function will be covered in detail in chapter 6; for now the intricacies of W are not important, only that it allows for closed solutions of λ_R.

Now we turn to the minima of λ_R. There are two ways for minima λ_R to occur:

1. When G is broken (discontinuous) across the λ_R axis (i.e. for $\kappa\tau \geq 1/\sqrt{2\mathrm{e}}$) the minima come from F and G intersections where one solution moves left along the λ_R axis and the next solution over moves right.

2. When G is continuous, the minima come from the even n in Eq. (4.5).

Let's begin with the first condition – at a certain detuning, two neighboring intersections of F and G with different λ_I values will have the same λ_R value. This leads to a set of four coupled equations for the two sets of coordinates $(\lambda_R, \lambda_{I_1})$ and $(\lambda_R, \lambda_{I_2})$ and the detuning $\Delta\omega$ for which they occur:

$$\lambda_R^2 - \lambda_{I_1}^2 + \Delta\omega^2 - \kappa^2 \mathrm{e}^{-2\lambda_R\tau}\cos(2\tau(\lambda_{I_1} + \theta)) = 0 \tag{4.6a}$$

$$\lambda_R^2 - \lambda_{I_2}^2 + \Delta\omega^2 - \kappa^2 \mathrm{e}^{-2\lambda_R\tau}\cos(2\tau(\lambda_{I_2} + \theta)) = 0 \tag{4.6b}$$

$$\lambda_R\lambda_{I_1} + \kappa^2 \mathrm{e}^{-2\lambda_R\tau}\sin(2\tau(\lambda_{I_1} + \theta)) = 0 \tag{4.6c}$$

$$\lambda_R\lambda_{I_2} + \kappa^2 \mathrm{e}^{-2\lambda_R\tau}\sin(2\tau(\lambda_{I_2} + \theta)) = 0 \tag{4.6d}$$

It turns out that these cannot be solved analytically, since by combining the third and fourth equations we arrive at a transcendental equality for the λ_I:

$$\frac{\lambda_{I_1}}{\sin(2\tau(\lambda_{I_1} + \theta))} = \frac{\lambda_{I_2}}{\sin(2\tau(\lambda_{I_2} + \theta))}. \tag{4.7}$$

However, since for typical values of $\kappa\tau$ G is only broken for small n, it turns out that condition (1) is not relevant for large n, i.e. far from the central dome. This region of large n was also investigated in the SOW analysis, as the analytic prediction was only valid for high oscillation number. In that unbroken G region minima condition (2) holds, and we already have an analytic expression for that — Eq. (4.4). By choosing *even* n this time we can write the $\lambda_{R_{min}}$ as

$$\lambda_{R_{min}} = \frac{1}{2\tau}\mathrm{W}_0\left(\frac{-(2\kappa\tau)^2}{(2n+3)\boldsymbol{\pi} - 4\theta\tau}\right). \tag{4.8}$$

Note the slight change in the denominator inside the Lambert function from $(2n+1)$ to $(2n+3)$ when comparing Eqs. (4.5) & (4.8). Now the SOA can be evaluated as the difference between $\lambda_{R_{max}}$ and $\lambda_{R_{min}}$:

$$\text{SOA} = \frac{1}{2\tau}\left[\text{W}_0\left(\frac{(2\kappa\tau)^2}{(2n+1)\boldsymbol{\pi} - 4\theta\tau}\right) - \text{W}_0\left(\frac{-(2\kappa\tau)^2}{(2n+3)\boldsymbol{\pi} - 4\theta\tau}\right)\right] \tag{4.9}$$

The question is now this: what is the behavior of the SOA for large n? That is, of course, the region for which this analysis is valid. By large n we mean that the arguments of the W functions are much less than 1: $\frac{2\kappa^2\tau^2}{n\boldsymbol{\pi}} << 1$. For large n the phase accumulation term $\theta\tau$ is washed out, and therefore PA has no impact on the SOA, just like the SOW analysis. The Lambert W function can be approximated by the series

$$\text{W}_0(x) \approx x - x^2 + \frac{3}{2}x^3 - ... \tag{4.10}$$

which becomes linear for small x. However, since the expansion terms are rather large for the W function, for a linear approximation to be valid x must be on the order of 0.1. This corresponds to an n value of around 10-20 oscillations. After making a linear approximation of Eq. (4.9) we find that the sideband oscillation amplitude has the following dependence on $\kappa\tau$:

$$\frac{\text{SOA}}{\kappa} = \frac{2\kappa\tau}{n\boldsymbol{\pi}}. \tag{4.11}$$

The SOA scaled by κ has 1) an inverse dependence on n and 2) a linear dependence on $\kappa\tau$, which can both be checked numerically and experimentally. The first part of this prediction seems reasonable, as both numerical and experimental intensity profiles show a decreasing sideband amplitude as $|\Delta\omega|$ increases. Of course, the constants involved in this prediction may differ from numerical and experimental results due to the unknown correspondence between eigenvalue and intensity, but the functional form should be valid.

4.3 Numerical SOA Results

Using the LK rate equation model we can numerically measure the SOA as a function of both n and $\kappa\tau$. First, an intensity profile is generated by integrating the LK equations and plotting the results as a function of detuning. For consistency we choose to measure oscillations on the *positive* $\Delta\omega$ side of the central dome. Only oscillations far from the dome are measured. Figure 4.3a shows a typical intensity profile for experimental parameters ($\kappa = 0.02, \tau = 100$). The SOA is measured by numerically searching for the intensity maxima and minima and taking the difference. The inverse of SOA/κ is then plotted vs. oscillation number n, for which we expect a linear fit. The slope of the fit should in theory be equal to $\boldsymbol{\pi}/(2\kappa\tau)$. The intercept of the fit gives the initial oscillation number, which is not anything we're interested in. Figure 4.3b shows the $(\mathrm{SOA}/\kappa)^{-1}$ vs. n curve for the intensity data in Fig. 4.3a – the results are almost perfectly linear, confirming the first prediction about the dependence on n. Surprisingly, the actual value (0.755) is very close to the prediction (0.785), but only for the *variable* PA case. Of course, we were not expecting such correspondence between the exact prefactors of the theoretical results and the numerical data.

By finding the slope of these linear fits for multiple values of $\kappa\tau$ and plotting the inverse of these slopes (which we call M) as a function of $\kappa\tau$ we are able to generate Fig. 4.3c, which shows the linear dependence of M on $\kappa\tau$. The analytic predictions for this slope is $2/\boldsymbol{\pi}$. The star points are for variable PA and the circle points are for zero PA. The different colors in Fig. 4.3c correspond to different values of κ, and the linear trends hold well for $\kappa\tau < 5$ in both cases. This result confirms the second prediction of Eq. (4.11). It really is remarkable that there is so much correspondence between the pseudo-Hamiltonian model and the rate equation model, as the Hamiltonian model lacks many of the complicating pieces of the LK equations. For higher $\kappa\tau$ we need access to very high oscillation numbers n, and since the rate equation model is only valid for small detunings ($\Delta\omega < 1$) we are unable to actually

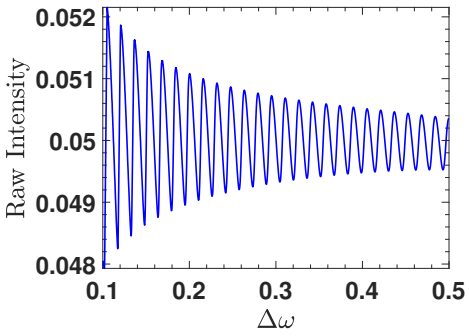

(a) SCL 1 intensity vs. detuning for variable PA. In this plot $\kappa = 0.02$ and $\tau = 100$. Only one laser is shown in this figure.

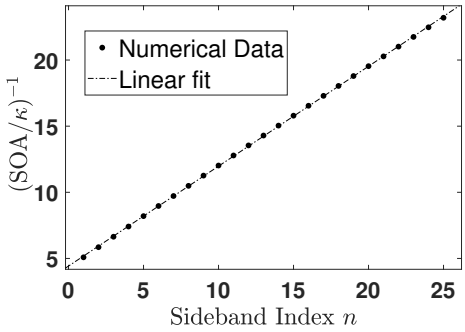

(b) SOA inverse vs. n. This data as taken from Fig. 4.3a (same parameters). The slope of the fit (0.755) is very close to the analytic prediction (0.785).

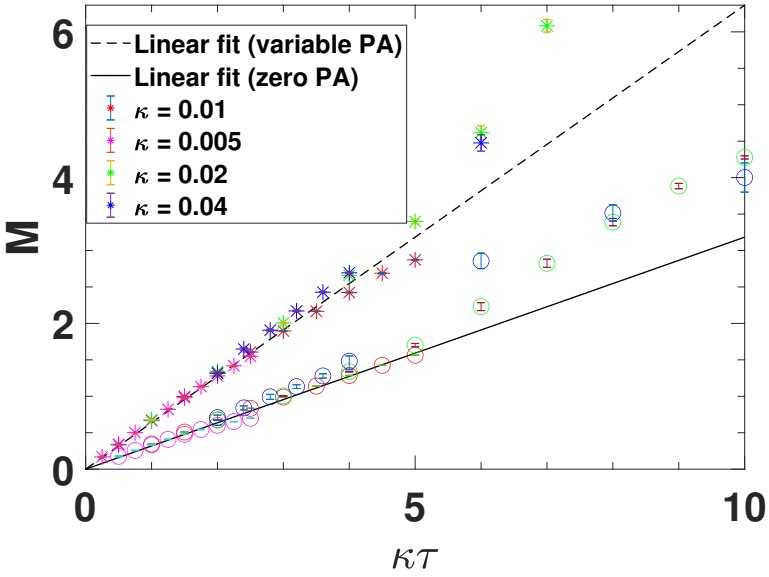

(c) M as a function of $\kappa\tau$. The star points are for the variable PA case, and the circle points are for zero PA. The colors correspond to different values of κ (see figure legend). The solid and dashed lines are the linear fits for zero PA and variable PA, respectively.

Figure 4.3. A summary of numerical SOA results. Plots a and b are for $\kappa\tau = 2$. Once an intensity profile (Fig. 4.3a) is generated, the SOA is numerically calculated and the inverse is plotted against index number n (Fig. 4.3b). By repeating this process for many combinations of $\kappa\tau$ Fig. 4.3c is generated; both the variable PA and zero PA cases were studied.

generate such high oscillation numbers numerically; this is what slightly throws the data off the linear trend. For the zero PA case the slope of this trend is 0.33 – surprisingly, for the *variable* PA case the slope is almost exactly twice the zero PA slope, at 0.65. Similar to the SOW phenomenon, a factor of 2 separates the results from each case. Furthermore, the slope for the variable PA case is almost exactly equal to the analytic prediction of $2/\pi$. Again, we were not expecting any such correspondence.

As an aside, the factor of 2 difference between the variable PA and zero PA models can be explained by the following logic. The variable PA has the effect of generating twice as many sideband oscillations for a fixed detuning when compared to the zero PA case. Furthermore, for every other sideband oscillation, the F and G equations in each case must overlap by definition. Therefore we expect the amplitudes in the variable PA case to change twice as slowly, which results in a steeper M vs. $\kappa\tau$ plot.

4.4 Experimental Results

The procedure for experimental measurement of the SOA is similar to the numerical case: generate an intensity profile as a function of detuning and measure the peak-to-trough amplitude of the sideband oscillations. A slight complication arises due to experimental realities, however; for larger $\kappa\tau$ values the sidebands are hard to experimentally observe, as their amplitudes are very small. Therefore we make the compromise of measuring the oscillations immediately following the central dome, since those oscillations are large. We then have the added benefit of measuring the SOA in a region in which the amplitude rate of change is the greatest, which may allow for better results due to limited detector resolution. This means the large n approximation will not hold, but even with this complication the data still fits the predictions reasonably well.

Figure 4.4a shows a typical experimental intensity profile for $\kappa = 0.008$ and $\tau = 138$. These oscillations are somewhat noisy, but there is enough resolution to measure the peaks and troughs. From this data we are able to generate a $(\mathrm{SOA}/\kappa)^{-1}$ vs. n plot, shown in Fig.

4.4b. Again we see a very good linear fit, confirming the first prediction of Eq. (4.11). Slopes are measured for several combinations of $\kappa\tau$, and the resulting M vs. $\kappa\tau$ plot is given in Fig. 4.4c. Here there is less agreement with the analytic prediction. A linear trend is not clear – there is a monotonic increase in M, but the value of M seems to saturate for higher $\kappa\tau$, almost looking like a square root curve. There are many experimental complications that may explain the poorness of this fit:

1. We do not have access the high n region needed for the analytic prediction to be valid.

2. The intensity signal is noisiest near the central dome, which is very close to where we are measuring the SOA.

3. Unlike the SOW measurements, the sideband amplitudes depend on the actual SCL intensity values. Care must be taken to ensure a proper detector calibration between data sets of different parameters. By decreasing the coupling strength the net intensity level of both lasers drops (due to the mutual injection and beam alignment) – this effect is not present in the numerical model. By scaling each data set by a base intensity level we attempt to overcome this complication, but it is not perfect.

4. As always there is uncertainty in κ, both due to the transmitted power vs. voltage curve from calibrating the detector and due to the fact that not all of the incoming light is actually injected into the lasers' active regions (something that we did not attempt to measure). There is phenomenological evidence for reducing the final value of κ by a factor of 10, which we already include in our coupling strength definition.

There is much room for improvement in this experiment, and perhaps better agreement can be obtained by future graduate students with more time. With the success of the SOW results and the good linearity of the $(\mathrm{SOA}/\kappa)^{-1}$ vs. n plots, it's reasonable to assume that the final piece should match the prediction a bit better than it does.

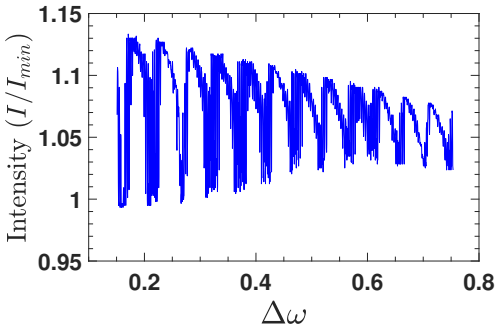

(a) Experimental SCL 1 intensity vs. detuning. In this plot $\tau = 138$ and $\kappa = 0.008$. Only one laser is shown in this figure (the one that oscillates).

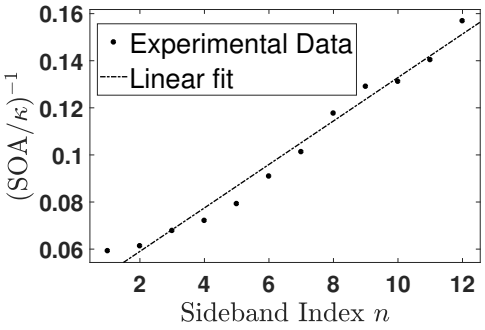

(b) SOA inverse vs. n. This data was taken from Fig. 4.4a (same parameters). The slope of the fit (0.00923) is not anywhere near the analytic prediction (1.423).

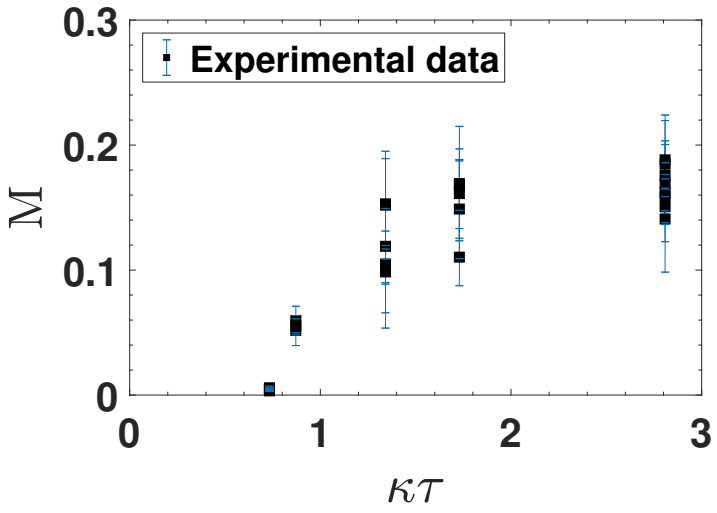

(c) M as a function of $\kappa\tau$. The overall behavior is not quite linear, though it does seem to monotonically increase, perhaps saturating for large $\kappa\tau$.

Figure 4.4. A summary of experimental SOA results. Plots a and b are for $\kappa\tau = 1.10$. Once an intensity profile (Fig. 4.4a) is generated, the SOA is numerically calculated and the inverse is plotted against index number n (Fig. 4.4b). By repeating this process for many combinations of $\kappa\tau$ Fig. 4.4c is generated. The linear trend in Fig. 4.4b is good confirmation of the first SOA prediction – however, there is not a linear trend in Fig. 4.4c, which does not confirm the second SOA prediction.

It's somewhat surprising that the first prediction of Eq. (4.11) is experimentally reproduced so well, but the second is not. Nevertheless, the experimental results are further proof that the analytic model is very useful for explaining the underlying reasons for complicated intensity behavior. **agarwal_spontaneous_2012**

5. CENTRAL DOMEWIDTH

5.1 Introduction

In this chapter we will discuss the central domewidth of the SCL intensity, which is proportional to the frequency detuning at which the PT-transition occurs. For convenience we will refer to the domewidth as $\Delta\omega_c$, as it is ultimately a detuning measurement. Of course, for nonzero delay the system is no longer PT-symmetric; however, the SCL intensities still show a sort of "phase transition" between bounded and divergent behavior near the PT-symmetric detuning $\Delta\omega = \kappa$. Figure 5.1 shows an example intensity profile for the two lasers for the case of variable PA. There is a transition between bounded behavior ($|\Delta\omega| > \kappa$) and divergent behavior ($|\Delta\omega| < \kappa$), although the transition is no longer as clear as the zero delay case. We therefore experimentally define the domewidth as the detuning region for which the central dome intensity stays above a threshold value for each laser (horizontal dash-dot line). The domewidth is then the detuning range for which this condition holds (vertical dashed lines). The time delay has the effect of widening this divergent intensity region non-monotonically, and we attempt to investigate this feature analytically, numerically, and experimentally. Unlike the previous two chapters, the domewidth is an inherently PT-symmetric phenomenon (at least in the absence of delay), as so we will now see firsthand how the complication of nonzero time delay affects PT system features.

First, an analytic prediction will be obtained via the Hamiltonian model. Next, this prediction will be checked against numerical and experimental intensity data. Ultimately we find that there is less agreement between the experimental results and the theoretical predictions, but that the qualitative features of the predictions are present in the data. We also briefly explore parameters spaces that may explain discrepancies between the experiment, LK model, and theory.

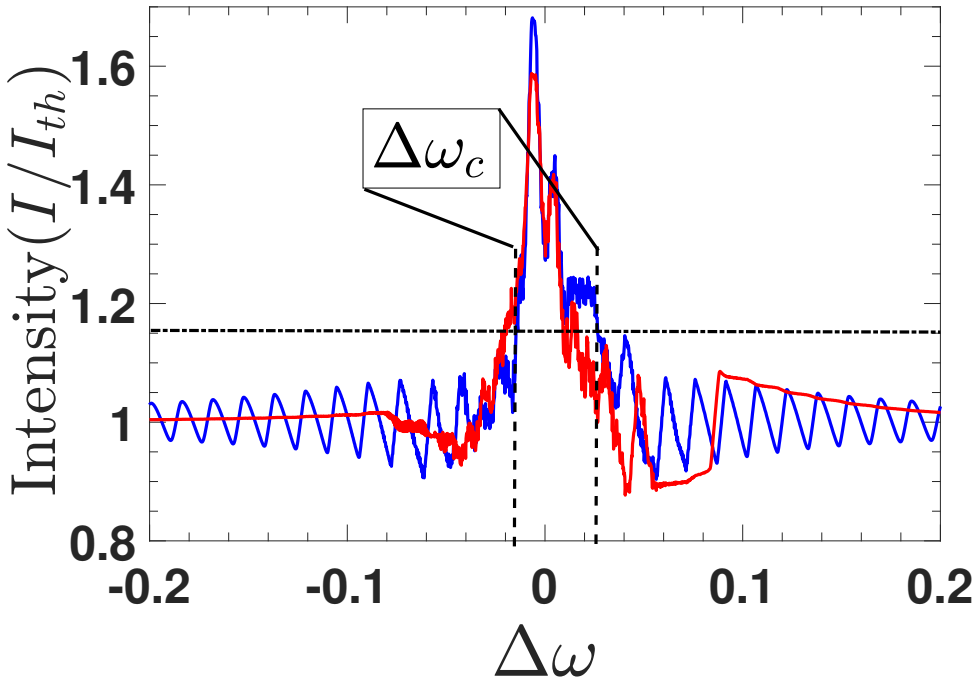

Figure 5.1. Example of the central domewidth for variable PA with parameters $\tau = 100$ and $\kappa = 0.02$. Intensities of SCL1 (blue) and SCL2 (red) are plotted as functions of detuning. There is a phase transition between bounded behavior ($|\Delta\omega| > \kappa$) and divergent behavior ($|\Delta\omega| < \kappa$), but this detuning location may not be equal to the PT-symmetric value. The domewidth $\Delta\omega_c$ is defined by the detuning range for which the SCL1 intensity stays above some threshold value (dash-dot horizontal line). The vertical dashed lines show the detuning locations for where this transition occurs.

5.2 Eigenvalue Analysis

The following theoretical analysis is based on a method first carried out by Dr. Yogesh Joglekar for the case of zero phase accumulation. My contribution was to extend the analysis to nonzero and variable PA.

Just like the sideband oscillation width and amplitude, the domewidth can be explained by examining the Hamiltonian model's eigenvalues, specifically the eigenvalues with the greatest real part. In the limit of zero time-delay the PT-transition is defined by the phase transition from real to imaginary eigenvalues; in other words, when the real parts of the eigenvalue solutions transition from zero to nonzero. We'll define the analytic domewidth in a similar way: the domewidth $\Delta\omega_c$ is the frequency detuning for which, starting from $\Delta\omega = 0$, the real part of the dominant eigenvalues first becomes zero. Because we do not have experimental access to eigenvalues we use a slightly different definition when it comes to numerical and experimental observation, the definition being laid out in the first paragraph of the previous section.

For this analysis we again start with the F and G equations (Eq. 3.3e&b) and try to find an expression for the location of where the dominant eigenvalue solutions first cross the y-axis. In chapter 3 we obtained an expression for the detunings at which the real part of the dominant eigenvalues cross the y-axis:

$$\Delta\omega_n = \pm\kappa\sqrt{(-1)^n + \frac{(n\boldsymbol{\pi})^2}{(2\kappa\tau)^2} + \frac{\theta^2}{\kappa^2} - \frac{n\boldsymbol{\pi}\theta}{\kappa^2\tau}} \tag{5.1a}$$

$$\Delta\omega_n = \frac{\kappa^2(-1)^n}{\left(\frac{n\boldsymbol{\pi}}{\tau} - 2\theta_0\right)} + \frac{1}{4}\Big(\frac{n\boldsymbol{\pi}}{\tau} - 2\theta_0\Big). \tag{5.1b}$$

Equation (5.1a) is for static phase accumulation and Eq. (5.1b) is for variable phase accumulation. The n value describes which crossing we're dealing with, as the dominant eigenvalues oscillate back and forth across the y-axis. Since we're looking for the crossing for which the dominant eigenvalue's real part first becomes zero we naively set $n = 0$ and solve for $\Delta\omega_0$,

which should then give us the domewidth $\Delta\omega_c$. However, when $\kappa\tau$ is larger than 1 the $n = 0$ choice is not valid for $\Delta\omega_c$ – yes, there is an eigenvalue crossing of the y-axis at this detuning, but just before that crossing the next eigenvalue over overtakes the crossing eigenvalue's real part and stays positive. In other words, the dominant eigenvalue stays positive past the first $\Delta\omega_n$ detuning value, and we must use the next crossing over, n_2. This is demonstrated in Fig. 5.2, which shows the F (blue) and G (red) curves for static PA with the parameters $\tau = 100$, $\kappa = 0.03$, and $\theta = 0$. The dominant eigenvalue (the rightmost intersection of F and G) has positive real part in Fig. 5.2a. As the detuning is increased towards $\Delta\omega_0$, the first y-axis crossing, that dominant eigenvalue's real part decreases towards zero. However, the eigenvalue with the *second most* real part begins moving toward the y-axis (Fig. 5.2b). Depending on the value $\kappa\tau$ the second eigenvalue can actually overtake the first's real part and become the dominant eigenvalue before the original eigenvalue crosses the y-axis, and so the dominant eigenvalue stays positive past $\Delta\omega_0$ (Fig. 5.2c). The dominant eigenvalue hops from one intersection to the next.

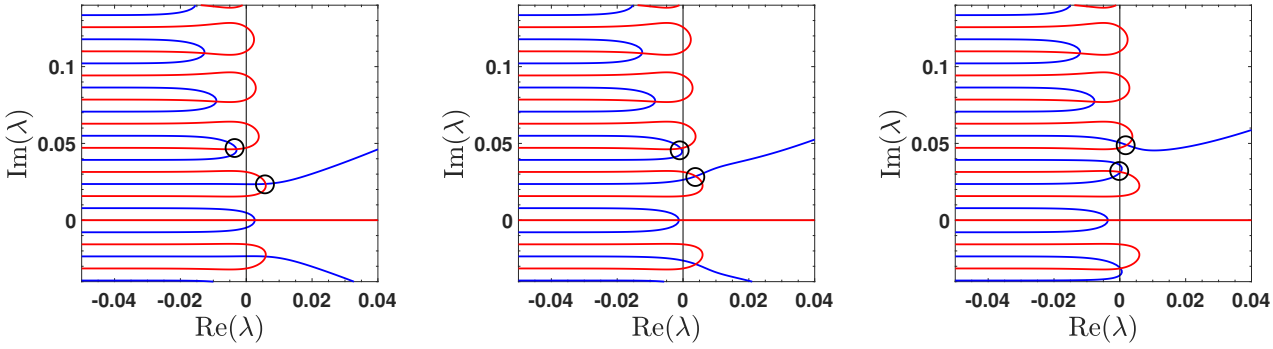

(a) $\Delta\omega = 0.023$ (b) $\Delta\omega = 0.034$ (c) $\Delta\omega = 0.043$

Figure 5.2. F (blue) and G (red) curves for zero PA, $\tau = 100$, and $\kappa = 0.03$. For values of $\kappa\tau > 1$ the dominant eigenvalue remains positive beyond $\Delta\omega_0$ in Eq. (5.1a). As the detuning is increased (subplots left to right) the dominant eigenvalue moves left along the Re(λ) axis, while the next eigenvalue over moves right. It's possible for the second most dominant eigenvalue to surpass the real part of the existing dominant eigenvalue such that the overall real part stays positive. These two eigenvalues, dominant and second most dominant, are circled in the subplots. Notice that in Fig. 5.2c the second most dormant eigenvalue has become the dominant eigenvalue.

So, how do we know which n value to use? If one eigenvalue's real part crosses from positive to negative while at the same time the adjacent eigenvalue's real part crosses from negative to positive, the system exhibits a dominant eigenvalue that is always positive. This reasoning will let us solve for the discontinuities $(\kappa\tau)_n$ for which we must change our value of n in order to accurately find $\Delta\omega_c$.

With the above condition for finding $(\kappa\tau)_n$ we get, for the case of zero PA, the expression

$$1 + \frac{(2n\pi)^2}{(2\kappa\tau)^2} = -1 + \frac{((2n+1)\pi)^2}{(2\kappa\tau)^2} \tag{5.2}$$

which gives the values of $(\kappa\tau)_n$

$$(\kappa\tau)_n = \frac{\pi}{2\sqrt{2}}\sqrt{4n+1} \tag{5.3}$$

which in conjunction with Eq. (5.1a) gives a complete analytic solution for the domewidth. For variable PA a similar method is used to find $(\kappa\tau)_n$:

$$(\kappa\tau)_n = \frac{\pi}{2}\sqrt{\frac{2n(2n+1)}{4n+1}} \tag{5.4}$$

The behavior of these equations is plotted in Fig. 5.3. Domewidth scaled by κ is plotted as a function of $\kappa\tau$. The solid curve is for zero PA and the dashed curve is for variable PA. The central domewidth will increase non-monotonically as a function of $\kappa\tau$, essentially "widening" beyond the PT-symmetric value of $\Delta\omega/\kappa = 1$. In both PA scenarios the domewidth jumps discontinuously at the prescribed locations $(\kappa\tau)_n$, with the variable case having twice as many "sawteeth" for a given $\kappa\tau$ range (again, the factor of 2 appears when comparing the variable to static case!). Asymptotically, for large $\kappa\tau$ the domewidth increases linearly with a slope 2π. This asymptotic slope is common to both PA cases and can be derived from Eq. (5.1a&b). Taking the limit of large $\kappa\tau$ and combining expressions $(\kappa\tau)_n$ and $\Delta\omega_n$ reduces the domewidth solutions to $\Delta\omega_c/\kappa \approx \frac{2}{\pi}\kappa\tau$ for *both* PA cases.

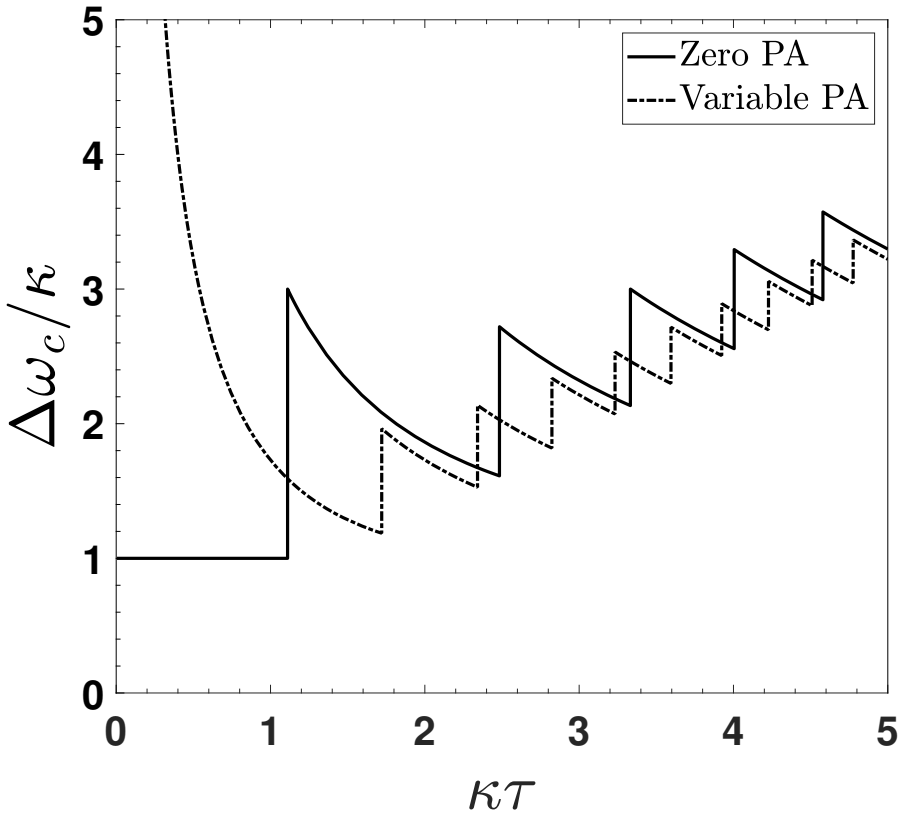

Figure 5.3. Analytic solution for $\Delta\omega_c/\kappa$ as a function of $\kappa\tau$. The domewidth is expected to increase non-monotonically as a function of coupling strength and delay. The solid curve is for zero PA and the dashed curve is for variable PA.

Interestingly, the domewidth predictions differ dramatically when $\kappa\tau < 1$; in the zero PA case the domewidth is constant, equal to the zero-delay PT-symmetric case. In the variable PA case the domewidth diverges for small $\kappa\tau$. This is due to the fact that for variable PA the eigenvalue solutions with positive $\mathrm{Im}(\lambda)$ obey Eq. (5.1b); for eigenvalues with negative $\mathrm{Im}(\lambda)$ that equation does not work. We are not sure exactly as to why this is; however, for consistency we choose to analyze only the dominant eigenvalues in the $\mathrm{Im}(\lambda)$ half of the plane. A consequence of this is that if $\kappa\tau < 1.9$ then there are no dominant eigenvalues with positive real parts, leading to divergent and incorrect domewidths. After $\kappa\tau = 1.9$ the domewidth prediction is valid.

There are two main predictions for the domewidth, for either PA case: 1) the domewidth increases non-monotonically as a function of $\kappa\tau$ with an asymptotic slope $2/\boldsymbol{\pi}$, and 2) there are discontinuous jumps at prescribed $\kappa\tau$ locations. We now examine the numerical results.

5.3 Numerical Results

By integrating the LK equations and generating intensity plots we can check the above prediction via numerical analysis. The procedure is to generate an intensity vs. detuning plot for a given $\kappa\tau$, find the detuning range over which the intensity of SCL1 stays above some threshold value, and then recording that data. This can be done for many combinations of $\kappa\tau$ until a corresponding $\Delta\omega_c/\kappa$ vs. $\kappa\tau$ plot is filled out. The threshold intensity is chosen such that the zero-delay domewidth is exactly equal to κ. This ensures the domewidth plot starts at 1 on the y-axis.

5.3.1 Zero Phase Accumulation

Figure 5.4 shows numerically generated domewidth plots for zero PA. The y-axis is $\Delta\omega_c$ and the x-axis is $\kappa\tau$. For the top plot, κ is fixed to be 0.2 while τ is swept from 0 to 25; in the bottom plot $\kappa = 0.1$ and τ runs from 0 to 50. Both plots use the same intensity threshold to measure $\Delta\omega_c$. The data does not exactly reproduce the prediction in Fig. 5.3, but there is

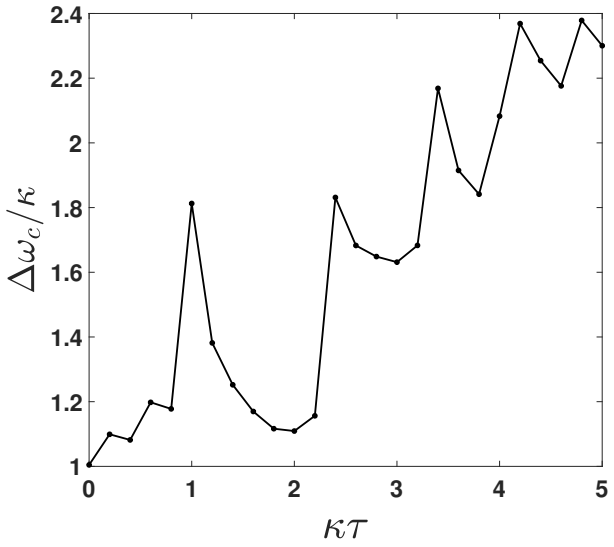

(a) $\kappa = 0.2$, $\tau = 0 - 25$

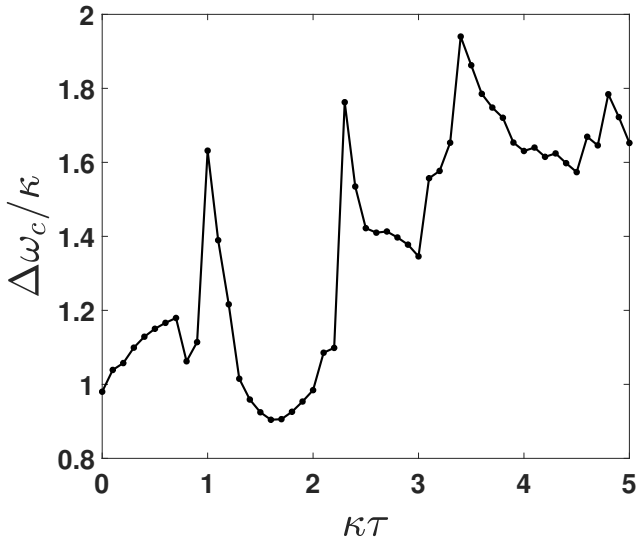

(b) $\kappa = 0.1$, $\tau = 0 - 50$

Figure 5.4. Numerical domewidth for zero PA. The y-axis is the measured domewidth $\Delta\omega/\kappa$ and the x-axis is $\kappa\tau$. In both plots we fix κ and sweep τ. The two predictions from Fig. 5.3 are present in the top plot, less so in the bottom plot: 1) a non-monotonic increase in $\Delta\omega_c/\kappa$ and 2) discontinuous jumps near the predicted $\kappa\tau$ (compare to Fig. 5.3). It seems that the accuracy of the domewidth prediction requires τ to be small.

strong evidence for the two main predictions. The domewidth increases non-monotonically with an apparent slope of 0.3 (for the top plot, about half the prediction), and there are

discontinuous jumps near where the analytic model predicts. The exact size of the jumps do not necessarily match the prediction, but since the definition for domewidth differs between the two models we find that there is reasonably good agreement. Similar behavior is seen for SCL2. Figure 5.4b does not match the prediction as well as Fig. 5.4a. This is due to the fact that the domewidth depends on κ and τ independently when it comes to the LK equations and experiment. For whatever reason the accuracy of the analytic solution requires τ to be small (0-30), which is physically hard to implement (cavity length of 0-10cm). In both plots the coupling strength is very large, which is also not achievable in the lab.

5.3.2 Variable Phase Accumulation

For variable PA the domewidth plot is given in Fig. 5.5, where $\kappa = 0.2$ and τ is swept from 0 to 25. This domewidth measurement used the same threshold level as in Fig. 5.4a&b. Again, to a reasonable degree the numerical results matches the prediction in Fig. 5.3 for variable PA. After $\kappa\tau = 1.9$ the domewidth increases non-monotonically with a similar slope (0.4), and it appears to have discontinuities near the prescribed values $(\kappa\tau)_n$. Before $\kappa\tau = 1.9$ the results are hard to decipher, but they stay close to $\Delta\omega_c/\kappa = 1.5$. Again, we emphasize that the analytic prediction for variable PA is not valid for this range.

5.3.3 Timescale Variation

How can the numerical results be improved? We attempted to find better agreement between the analytic and numerical results by modifying the physical parameters of the system to drive the numerical model more toward the analytic reduction. The parameter we alter is the ratio of the carrier to photon lifetime, T. One of the assumptions made to reduce the LK equations to the Hamiltonian model is that the carrier dynamics can be ignored. This can be achieved by setting T to a higher number than it's current value (100), since the rate of change $\frac{dN_i}{dt}$ is inversely related to T (Eq. 2.1c&d). If T is large, the carrier inversion does not change. This is not a parameter that we can alter in the lab, as it is tied

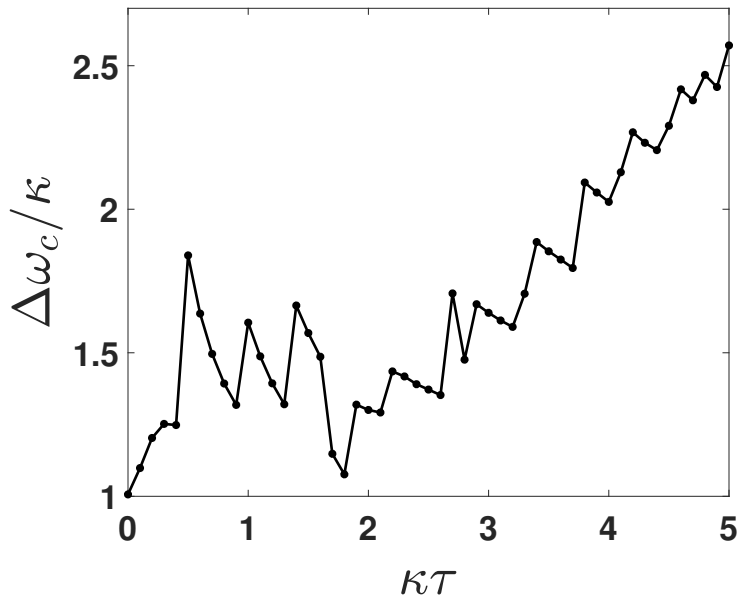

Figure 5.5. Numerical domewidth plot for variable PA, $\kappa = 0.2$ and $\tau = 0 - 25$. The y-axis is the measured domewidth $\Delta\omega/\kappa$ and the x-axis is $\kappa\tau$. When $\kappa\tau > 1.9$ the observed behavior reasonably matches the analytic prediction in Fig. 5.3 (dashed line).

to semiconductor material characteristic, but such an alterations easy to vary numerically. This T behavior was investigated numerically by repeating the domewidth measurement for large and small T, T=1000 and T=10. The results are plotted in Fig. 5.6a&b. Figure 5.6a is for T = 1000 and Fig. 5.6b is for T=10. Surprisingly we get the opposite of what we expected: the domewidth measurements are better for smaller T. This can be explained by noting that a small ratio T means the carrier lifetime is comparable to the photon lifetime; in other words, a change in SCL intensity is almost immediately followed by the corresponding change in carrier inversion. In this limit the carrier dynamics mirror the intensity dynamics with a small time lag (depending on T), and if this time lag is small then the carrier dynamics can be effectively be ignored.

In summary, the LK equations show reasonably good agreement with the analytic prediction, albeit for a limited parameter range.

5.4 Experimental Results

The experimental method for determining the domewidth as a function of $\kappa\tau$ is the same as the numerical case: generate an intensity vs. detuning curve for SCL1 (swept laser), find the detuning range for which the intensity remains above some threshold value, and record this range as the domewidth $\Delta\omega_c$. Figure 5.7 shows the experimental results. The orange points are for a delay of 95 and the blue points are for a delay of 180, and κ is swept to obtain the corresponding $\kappa\tau$ points. At first glance there doesn't seem to be much correspondence between this plot and the dashed-curve in Fig. 5.3. However, we argue that there is evidence for agreement with the analytic variable PA model. First, Fig. 5.7 shows that the experimental data has discontinuous jumps near the prescribed locations $(\kappa\tau)_n$. There is a jump near $\kappa\tau = 1.7$, 2.5, 3, 3.6, and 4, although the magnitudes certainly do not match the prediction. Comparing these values with those in Fig. 5.3 and we see they are not far off the jumps in the dashed curve. Next, the domewidth remains constant before $\kappa\tau = 1.5$, which is also present in the numerical results in Fig. 5.5. This constant $\Delta\omega_c/\kappa$

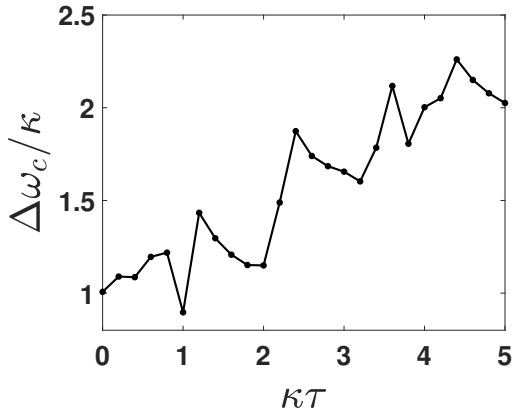

(a) $\kappa = 0.2$, $\tau = 0 - 25$, $\theta = 0$, T = 1000

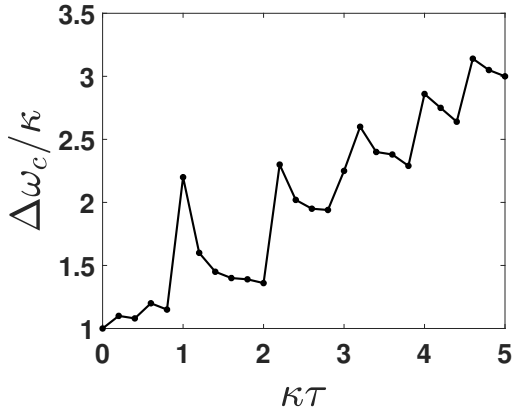

(b) $\kappa = 0.1$, $\tau = 0 - 25$, $\theta = 0$, T = 10

Figure 5.6. Domewidth plots for two different values of T, the ratio of carrier to photon lifetimes. The top plot is for T=1000 and the bottom is for T=10. We naively expect better results for large T; however, the opposite is true. Notice how the slope of the bottom plot (T=10) is very close to the prediction of $2/\boldsymbol{\pi}$.

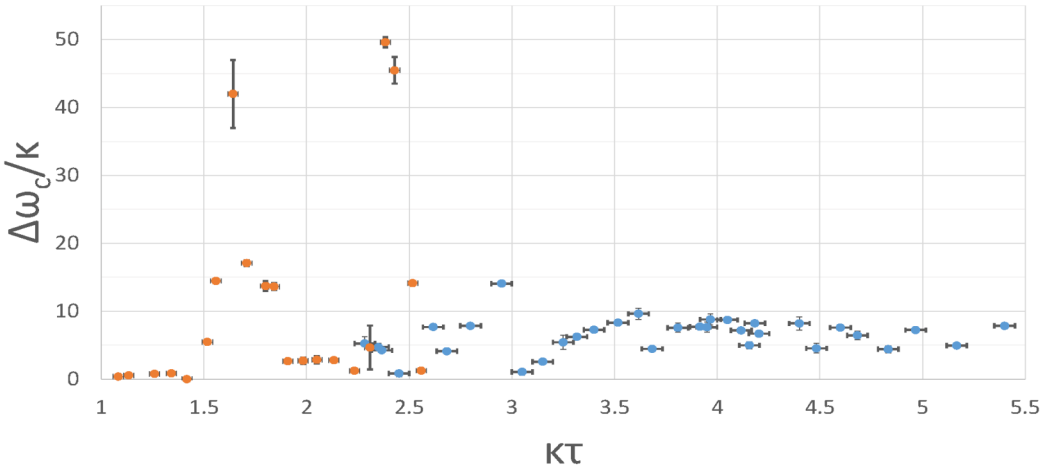

Figure 5.7. Experimental domewidth $\Delta\omega_c/\kappa$ vs. $\kappa\tau$. The orange points are for $\tau = 95$ and the blue points are for $\tau = 180$. Arguably, the main features of the analytic prediction are present in this plot, namely large discontinuities near the prescribed $(\kappa\tau)_n$, a static domewidth before $\kappa\tau = 1.9$, and an overall increasing domewidth until $\kappa\tau \approx 4$ where the value saturates.

behavior is predicted in the zero PA case as well. Finally we see that the overall domewidth increases non-monotonically until $\kappa\tau \approx 4$ upon which the value saturates for larger $\kappa\tau$.

This saturation is present in the numerical results as well, and of course the experiment is expected to share more features with the LK model than the analytic model. Figure 5.8 shows the domewidth saturation for large $\kappa\tau$. For $\kappa = 0.2$ and $\theta = 0$ the delay time is swept over a range 0-75. The domewidth increases non-monotonically until it eventually saturates to a constant value. The value of $\kappa\tau$ for which this saturation occurs *decreases* as the value of κ decreases. In other words, for experimental values of κ and τ the domewidth saturates for $\kappa\tau$ on the order of 4-8. This may explain why the experimental data appears to saturate near $\kappa\tau \approx 4$.

5.5 Summary

While the domewidth measurements seem less robust when compared to the sideband measurements, there is still good evidence that the central domewidth can be explained via

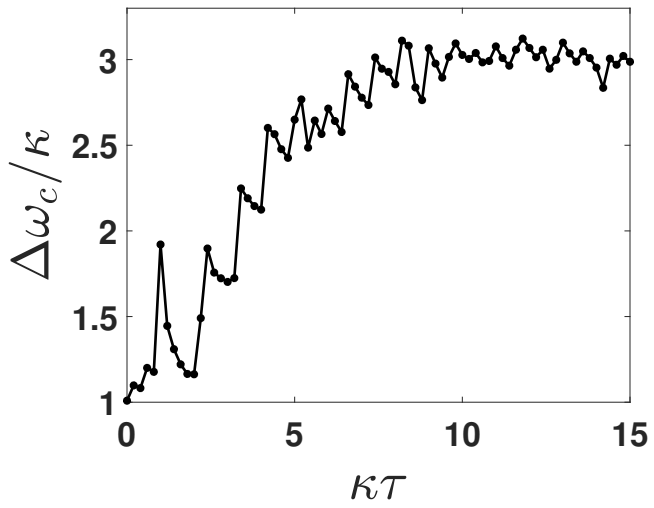

Figure 5.8. Domewidth saturation. The parameters for this plot are $\kappa = 0.2$, $\tau = 0 - 75$ $\theta = 0$, and T = 100. The measured $\Delta\omega_c/\kappa$ increases until it saturates to a constant value. The $\kappa\tau$ for which the domewidth saturates depends on τ.

an eigenvalue method based on the reduced Hamiltonian model. In the absence of delay this Hamiltonian model agrees extremely well with the LK equation intensities, and the system exhibits a PT-transition exactly when $\Delta\omega = \kappa$. The added complexity of time delay serves to widen this transition in a non-monotonic fashion, which is supported by analytic, numerical, and experimental results. The instantaneous SCL intensities in and near the central dome are subject to chaotic behavior, and for a given detuning the SCL intensities may fluctuate with large amplitudes in time, reaching values of $I/I_{th} = 1.3 - 1.4$. Therefore we expect noisier data in this region, even after time-averaging the numerical and experimental data. The asymmetric dependence of the domewidth on κ and τ, seen in the numerical investigation, also makes this feature unique when compared to the SOW and SOA results. Finally, the domewidth measurement is highly dependent on the intensity threshold used to determine the domewidth detuning range. Due to the chaotic behavior of the lasers near $\Delta\omega = \kappa$ and the emergence of high-amplitude sideband oscillations near that same transition, a small change in threshold intensity can completely alter the domewidth results. Overall the central PT-transition is much more sensitive to system parameters, and it is unclear how much more improvement in experimental measurement there can be with our current "off-the-shelf" equipment.

6. EXCEPTIONAL POINTS

This chapter is written as a theory paper to be submitted for publication. It is presented here in its entire form, with minor editing.

6.1 Introduction

Recent years have seen an explosion of interest in parity-time symmetric (PT) systems which are described by a class of non-hermitian Hamiltonians that may yield real eigenvalues under some conditions [14]–[24]. PT-symmetric Hamiltonians are invariant under simultaneous application of parity ($x \to -x$, $p \to -p$) and time-reversal ($t \to -t$) operators [14], [15], and a system described by such a Hamiltonian can be tuned via a non-Hermiticity parameter such that the eigenvalues undergo a transition from real to complex. The fundamental interest in PT-symmetric Hamiltonians arises from the possibility of extending quantum mechanics to open systems and complex space, where non-Hermiticity is associated with energy or probability dissipation. PT-symmetry requires a complex potential, and since the refractive index in optics (which is related to gain/loss) plays the role of potential, optical systems have been a fertile playground for the implementation of PT-symmetry, and various configurations with balanced gain and loss have been proposed and demonstrated [24], [51]–[54]. On the applied front, PT-symmetric systems have applications that include unidirectional light propagation and single-mode lasing, among others [30], [55]–[57].

One common realization of a PT-symmetric dimer consists of two evansecently coupled, single-mode waveguides, one of which has gain and the other an equal amount of loss [24]. Denoting the gain/loss by $\pm\gamma$ and the mutual coupling by κ, the resulting Hamiltonian is

$$H = \begin{pmatrix} i\gamma & \kappa \\ \kappa & -i\gamma \end{pmatrix}. \tag{6.1}$$

The eigenvalues of this matrix are given by $\lambda = \pm\sqrt{\kappa^2 - \gamma^2}$, which are real for $\gamma < \kappa$, complex for $\gamma > \kappa$, and for $\gamma = \kappa$ the two eigenvalues become degenerate and the corresponding eigenvectors coalesce. The regime with real eigenvalues is referred to as the PT-unbroken phase, and the regime with complex eigenvalues is the PT-broken phase. In the unbroken regime the wavefunction norm is bounded, but in the PT-broken regime the norm grows or decays exponentially. The transition from one phase to the other is marked by a sharp threshold, $\gamma = \kappa$ in this case, and this point is called an exceptional point (EP), defined by degenerate eigenvalues and parallel eigenvectors at this threshold. EPs are generic properties of non-hermitian matrices and as such appear in classical and quantum systems that can be characterized as eigenvalue problems. They were extensively discussed in nuclear physics [33], predicted in quantum chaotic systems [34], and shown to occur in coupled microwave cavities [35]. The EP boundary between the PT-broken and unbroken regions is a key feature of PT-symmetric systems, and there has been considerable effort devoted to investigating the properties of EPs [36], [58]–[70]. Indeed, very recently the importance of EPs in PT-symmetric photonic systems has received much attention (see e.g. Ref. 36). In particular, because the variation across an EP leads to an abrupt increase in the norm of the wavefunction, there has been an interest in exploiting EPs for enhanced sensing applications. It has been shown that when operating a non-Hermitian system near an EP with n degeneracies, a small perturbation ϵ produces an eigenvalue response of order $\epsilon^{1/n}$, as opposed to a linear response in Hermitian systems [29], [71]–[73]. For $\epsilon < 1$ this can enormously increase sensing resolution.

This section is motivated by a recent experimental implementation [74] of a classical PT-symmetric dimer in a pair of mutually coupled semiconductor lasers (SCLs), wherein light from one SCL is injected into the active region of the other SCL and vice-versa, as shown schematically in Fig. 6.1. A time-delayed coupling arose naturally in this system because the physical separation between the lasers was comparable to the characteristic time scales of the lasers (photon and carrier inversion lifetimes), thereby introducing a novel element into the

study of PT-symmetry [75]. It is important to emphasize that even though only two lasers are coupled to each other, this dimer configuration now becomes infinite-dimensional due to the delayed coupling. Without the time-delay our system has, under certain approximations, an effective Hamiltonian reminiscent of Eq. (6.1), with the diagonal elements now being the relative detuning between the lasers ($\pm\Delta\omega$) and the off-diagonal elements being the coupling strength of light from one laser into the other (κ) [73], [74]. The relative detuning $\Delta\omega$ is therefore the non-hermiticity parameter for the coupled SCLs. As we have shown in prior work [40], [58], despite a time-delayed coupling the SCLs continue to show remnants of PT-symmetric behavior commonly seen for zero delay, i.e. an abrupt phase transition across a boundary determined by the EP at $\Delta\omega = \kappa$. The delay also introduces new features into the behavior of the system, e.g. additional transitions (referred to as "sideband transitions") which manifest themselves as oscillations in a laser's intensity as the relative detuning is varied. These additional transitions were observed experimentally and faithfully reproduced in our numerical analysis based on a model that is commonly used to study coupled SCLs [42]. Typical numerical and experimental results are given in Fig. 6.2a&b, respectively, which show the intensity of the two SCLs as the relative frequency detuning is swept. In Ref. 75 we characterized the dependence of these additional transitions on coupling strength and time-delay through experiments, simulations, and analytic calculations.

The aforementioned sideband transitions and the infinite-dimensional nature of the system provided the stimuli for our examination of the nature of EPs in delay-coupled SCLs. Are there EPs in a PT-symmetric dimer if a time-delay is introduced in the coupling term? If so, how many are permitted, and under what conditions do these EPs appear? To address these questions, the emphasis of this paper is on an analysis of the eigenvalues and eigenvectors of the infinite-dimensional effective Hamiltonian that arises when a time-delayed coupling is introduced into an otherwise conventional PT-symmetric system. We begin our investigation by presenting a rate equation model that is used to describe a pair of mutually coupled SCLs, which we have shown in a previous work to reduce to the form of Eq. (6.1)

under certain reasonable approximations [43]. The inclusion of a time-delay in the coupling term makes analytical solutions very difficult, so we first report numerical results on the eigenvalues and eigenvectors of the system. We then use the Lambert W function, which we have shown recently can be used to study the dynamics of a laser with time-delayed coupling [44], to obtain analytical results which are in excellent agreement with the numerical results [74]. The analytic results allow us to establish constraints on parameters of the system which lead to EPs. In addition to revealing the overall behavior of the eigenvalues and eigenvectors in a time-delayed PT-symmetric system, our work establishes, numerically and analytically, that depending on parameter choices this system can have one, two, or zero second-order EPs and one third-order EP, in contrast to the zero-delay configuration wherein there is only one EP at $\Delta\omega = \kappa$.

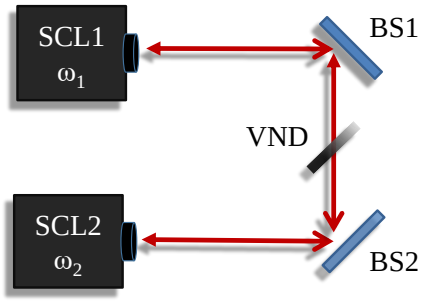

Figure 6.1. System diagram. Light emitted from each semiconductor laser (SCL) is directed by beam splitters (BS) back into the other's active region. The coupling strength is controlled with a variable neutral density filter (VND), and the frequencies of the lasers ($\omega_{1,2}$) are modulated by adjusting the SCLs' operating temperatures.

In Section 6.2 we present the rate equations for the lasers' intracavity electric fields and carrier inversions and reduce them to a pseudo-2x2 effective Hamiltonian. A numerical analysis of the eigenvalues and eigenvectors of this effective Hamiltonian is presented in Section 6.3, with special attention paid to the parameter conditions under which EPs can occur. Since the time-delayed system has infinite eigenvalues (and therefore infinite eigenvectors), we focus only on the seven largest ones which have the greatest influence on the intensity

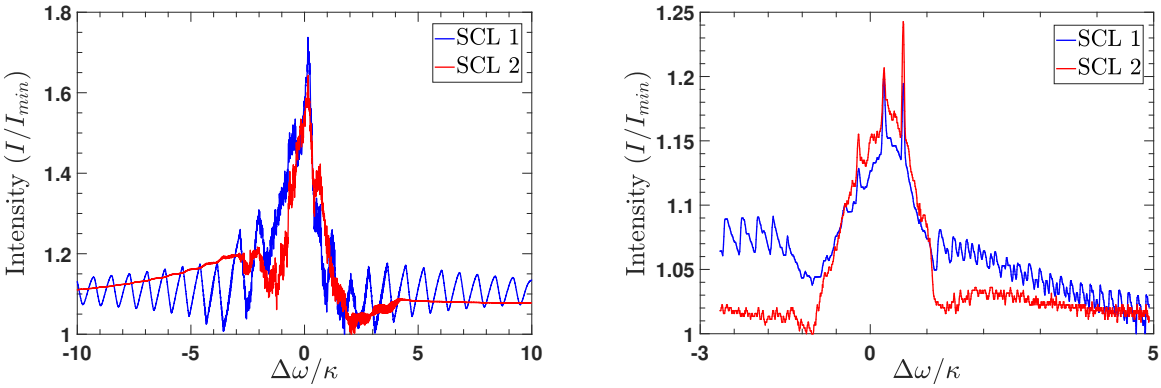

(a) Simulation (b) Experimental data

Figure 6.2. Numerical (panel a) and experimental (panel b) intensities for delay-coupled SCLs. The x-axis is the frequency detuning between the lasers (scaled by the coupling strength) and the y-axis is SCL intensity scaled to the background intensity. In both plots the scaled delay time τ is 120 and the scaled coupling rate κ is 0.02. All timescales are in units of the SCL photon lifetime, 10ps. There is a phase transition near $\Delta\omega/\kappa = 1$ where the intensities change from oscillatory to exponential growth/decay. The sideband oscillations are *not* temporal oscillations due to complex eigenvalues; rather, these are slow oscillations that remain after a 10ns averaging process and arise solely due to the non-zero delay. The asymmetry between lasers is due to the fact that only one laser's frequency is swept (blue) while the other is held fixed (red).

dynamics of the SCLs. Section 6.4 contains analytical results wherein we derive constraints on the relevant parameters which delineate regimes in which the EPs arise. The analysis is based on the use of the Lambert W function [44], and predictions of the analytical results are in excellent agreement with the numerical results. Finally, we conclude with a summary and discussion of the results.

6.2 Model

We begin by reviewing the reduction of the rate equation model that describes coupled SCLs to an effective Hamiltonian that resembles a conventional PT-symmetric system. The

rate equations are based on the Lang-Kobayashi model [41], which is often used to simulate SCL behavior [41], [45]–[48], [76], [77]. They are as follows:

$$\frac{dE_1}{dt} = (1 + i\alpha)N_1(t)E_1(t) + i\Delta\omega E_1(t) + \kappa e^{-i\theta\tau}E_2(t-\tau), \tag{6.2a}$$

$$\frac{dE_2}{dt} = (1 + i\alpha)N_2(t)E_2(t) - i\Delta\omega E_2(t) + \kappa e^{-i\theta\tau}E_1(t-\tau), \tag{6.2b}$$

$$T\frac{dN_1}{dt} = P_1 - N_1(t) - (1 + 2N_1(t)) \mid E_1(t) \mid^2, \tag{6.2c}$$

$$T\frac{dN_2}{dt} = P_2 - N_2(t) - (1 + 2N_2(t)) \mid E_2(t) \mid^2, \tag{6.2d}$$

where $E_{1,2}$ are the electric field amplitudes, $N_{1,2}$ are the carrier inversions above threshold for each laser, $P_{1,2}$ are the pump currents above threshold, α is the linewidth enhancement factor, τ is the time delay (which depends on the separation between the lasers), κ is the coupling strength of light from one laser into the other (taken to be equal for both lasers), and T is the ratio of the carrier lifetime to the photon lifetime. All timescales are in units of the SCL photon lifetime, 10ps. This phenomenological model assumes that the two lasers are identical and operate on a single longitudinal mode but have slightly different optical frequencies $\omega_{1,2}$, and the relative detuning between them is given by $\Delta\omega = \omega_1 - \omega_2$. The rate equations are written in a frame that is rotating at the average frequency of the lasers, $\theta = (\omega_1 + \omega_2)/2$. This model is valid for weak coupling, neglects multiple feedback reflections, and assumes that both lasers have identical gain coefficients despite a slight difference in their optical frequencies. The $\exp(-i\theta\tau)$ term accounts for the phase accumulation as light propagates from one laser to the other. The two PT parameters are the coupling strength κ and the frequency detuning $\Delta\omega$. A typical result generated by these equations is given in Fig. 6.2a, which shows the intensities of both lasers versus the frequency detuning between them. Alongside this plot is a representative experimental measurement for similar parameters (Fig. 6.2b), as reported in Ref. 75. The blue profiles are for the laser whose frequency is swept to change the relative detuning. In both experiments and simulations we observe an abrupt increase in the intensities of the lasers near $\Delta\omega = \kappa$. Additionally, there are oscillations in

the intensity as the detuning is increased — these sideband oscillations are a direct result of the delayed coupling.

We now follow arguments similar to those in Ref. 43 and assume that when the lasers are operating in a steady state the population inversion above transparency is very close to zero ($N_{1,2} \approx 0$), and so the population rate equations Eq. (6.2c) & (6.2d) can be ignored. Assuming electric field solutions of the form $e^{\lambda t}$, the delay term $E_{1,2}(t-\tau)$ in Eq. (6.2a) & (6.2b) is expressed as $e^{-\lambda\tau}E_{1,2}(t)$. This substitution results in a pseudo-2x2 model for the electric field dynamics,

$$\begin{pmatrix} \frac{dE_1}{dt} \\ \frac{dE_2}{dt} \end{pmatrix} = \begin{pmatrix} i\Delta\omega & \kappa e^{-\lambda\tau}e^{-i\theta\tau} \\ \kappa e^{-\lambda\tau}e^{-i\theta\tau} & -i\Delta\omega \end{pmatrix} \begin{pmatrix} E_1 \\ E_2 \end{pmatrix}, \tag{6.3}$$

which for zero delay reduces to a Hamiltonian reminiscent of the usual PT-symmetric dimer (Eq. (6.1)),

$$\begin{pmatrix} \frac{dE_1}{dt} \\ \frac{dE_2}{dt} \end{pmatrix} = \begin{pmatrix} i\Delta\omega & \kappa \\ \kappa & -i\Delta\omega \end{pmatrix} \begin{pmatrix} E_1 \\ E_2 \end{pmatrix}. \tag{6.4}$$

Note that the gain/loss terms in Eq. (6.1) are replaced by $\pm\Delta\omega$ [43]. The the eigenvalues of Eq. (6.4) are given by $\lambda = \pm\sqrt{\kappa^2 - \Delta\omega^2}$. Due to the classical nature of the model, this effective Hamiltonian actually describes an anti-PT symmetric system [78]–[80]; however, we will continue to refer to it as PT-symmetric since the conclusions of our work are not sensitive to this nuance.

In the general case with non-zero delay the model leads to an eigenvalue-like problem defined by

$$\det\left[\begin{pmatrix} i\Delta\omega & \kappa e^{-\lambda\tau}e^{-i\theta\tau} \\ \kappa e^{-\lambda\tau}e^{-i\theta\tau} & -i\Delta\omega \end{pmatrix} - 1\lambda\right] = 0. \tag{6.5}$$

It is important to note that when $\tau \neq 0$ the Hamiltonian is *not* a 2x2 eigenvlaue problem; rather, it is infinite dimensional due to the time delay, resulting in infinite solutions for λ.

The characteristic equation is evaluated with the substitution $\lambda = \lambda_R + i\lambda_I$, where λ_R and λ_I are real. Separating the real and imaginary components generates a pair of coupled equations, with $F(\lambda_R, \lambda_I)$ containing the real parts and $G(\lambda_R, \lambda_I)$ containing the imaginary parts:

$$F(\lambda_R, \lambda_I) = \Delta\omega^2 + \lambda_R^2 - \lambda_I^2 - \kappa^2 \mathrm{e}^{-2\lambda_R\tau}\cos(2\tau(\lambda_I + \theta)) = 0 \tag{6.6a}$$

$$G(\lambda_R, \lambda_I) = 2\lambda_R\lambda_I + \kappa^2 \mathrm{e}^{-2\lambda_R\tau}\sin(2\tau(\lambda_I + \theta)) = 0 \tag{6.6b}$$

The G equation is independent of $\Delta\omega$, an observation that will be important later in the discussion. We find solutions for the eigenvalues, λ, by numerically solving the coupled F and G equations and looking for their intersections.

The eigenvalues found by solving the F and G equations are then used to generate corresponding eigenvectors. Assuming a generic eigenvector $(\alpha, \beta)^T$ and substituting it into the matrix equation Eq. (6.3) results in coupled equations for α and β:

$$\lambda\alpha = i\Delta\omega\alpha + \kappa \mathrm{e}^{-\lambda\tau}\mathrm{e}^{-i\theta\tau}\beta \tag{6.7a}$$

$$\lambda\beta = \kappa \mathrm{e}^{-\lambda\tau}\mathrm{e}^{-i\theta\tau}\alpha - i\Delta\omega\beta. \tag{6.7b}$$

We can set α =1 without a loss of generality, so

$$\beta = \frac{\lambda - i\Delta\omega}{\kappa \mathrm{e}^{-\lambda\tau}\mathrm{e}^{-i\theta\tau}}. \tag{6.8}$$

The evolution of the eigenvectors $(1, \beta)^T$ can therefore be tracked by following the evolution of β. The behavior of eigenvalues λ and eigenvectors β are discussed in the next section. Multiple values of delay will be examined, both small delays (i.e. less than the relaxation oscillation period of the SCLs) and longer delays. Experimentally accessible delays that arise

from the physical footprints of the SCLs and other optics lie between $\tau = 80$ to $\tau = 300$ [74]. From the observations on degeneracy of eigenvalues and eigenvectors we will obtain information about the EPs of the time-delayed system.

6.3 Results

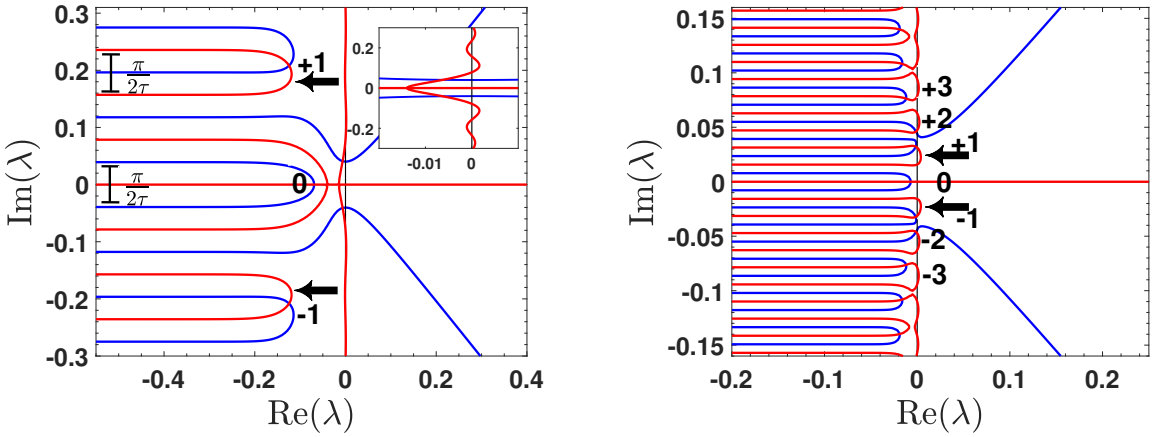

(a) $\kappa\tau$=0.4 ($\kappa = 0.02, \tau = 20$)

(b) $\kappa\tau$=2 ($\kappa = 0.02, \tau = 100$)

Figure 6.3. Plots of F (blue) and G (red) equations for different values of $\kappa\tau$ (without phase accumulation, $\theta\tau = 2n\pi$ where n is an integer). The x-axis is Re(λ) and the y-axis is Im(λ). Intersections correspond to eigenvalue solutions. The "fingers", or the branches that protrude from Re(λ) $= -\infty$, are labeled for the G equation. The black arrows indicates where the G "fingers" reach their maximum Re(λ) value, which is only greater than zero when $(\kappa\tau)^2 > 0.185$ (1/2e) (Fig. 6.3b). The inset plot in 3.1a shows a close-up view of the central G branch that straddles the Im(λ)=0 axis when $\kappa\tau = 0.4$. For all plots $\Delta\omega = 2\kappa = 0.04$ (though actual value of $\Delta\omega$ is not important). Note that the "finger" spacing is equal to $\pi/2\tau$, as indicated on plot (a).

We begin with a discussion of the behavior and evolution of the F and G equations, as they underlie the behavior and evolution of the system's eigenvalues and eigenvectors. Typical plots of $F(\lambda_R, \lambda_I)$(blue) and $G(\lambda_R, \lambda_I)$(red) are given in Fig. 6.3. To illustrate the important features, we will, for now, set the phase accumulation term $\theta\tau$ to be $2n\pi$ (where n is an integer), which corresponds to sweeping each laser's frequency at an equal rate but with opposite sign such that the relation $\theta = (\omega_1 + \omega_2)/2 = 2n\pi/\tau$ is always satisfied.

Each F and G plot has "fingers" which extend from Re(λ)=-∞ and curve back around near Re(λ)=0, and the spacing of each "finger" corresponds to the period of the sine and cosine terms in Eq. (6.6), $\pi/2\tau$. We label these "fingers" with indices 0, ±1, ±2, etc., with the 0th finger corresponding to the one that straddles the Re(λ)-axis and the index labels increasing (decreasing) as the fingers shift up (down) along the Im(λ)-axis (see Fig. 6.3 for an example of this labeling). The location of the turning point for each finger (i.e. the rightmost point the finger reaches on the Re(λ)-axis) depends on the coupling strength (κ) and time-delay (τ). We found numerically that only if $\kappa\tau > 1/\sqrt{2e}$ does the turning point lie beyond Re(λ)=0, shown with the black arrows in Fig. 6.3. As the detuning approaches zero, the F plot's "antennae", the two branches that extend outward toward Re(λ)=$\pm\infty$, move closer to the origin (result not shown). The G plot, as stated earlier, does not depend on $\Delta\omega$, and the line Im(λ)=0 is always a solution to the G equation. One particular branch of G is important in the eigenvalue dynamics, namely the branch that straddles the Re(λ)=0 axis (pictured in Fig. 6.4a insert). This branch is continuous for $\kappa\tau<1/\sqrt{2e}$ and is broken otherwise – as we will see in the next section, this breaking condition is critical to the existence of exceptional points. This value of $1/\sqrt{2e} \approx 0.43$ was first observed numerically; in the analysis section we will derive this analytically by using the Lambert W function. Finally, it is clear from these plots that besides the solutions on the Im(λ)=0 axis, all the intersections of F and G come in complex conjugate pairs. To examine the eigenvalues of our system, we need to plot the intersections of F and G and see how those points evolve.

6.3.1 Eigenvalue Results

In Fig. 6.4 are shown the real and imaginary parts of the eigenvalues as a function of $\Delta\omega$ for a delay of 0 (Fig. 6.4 a,c) and 100 (Fig. 6.4 b,d). The coupling strength is chosen to be $\kappa = 0.02$, a typical experimental value. The zero delay case yields the expected behavior wherein the real and imaginary parts of the two eigenvalues coalesce at the EP, i.e. when $\Delta\omega = \kappa$. When $\theta\tau = 2n\pi$ the eigenvalues appear in complex conjugate pairs and the plots

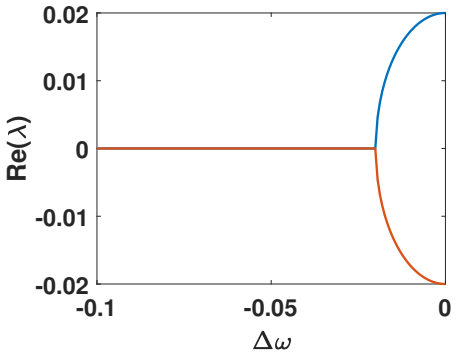

(a) Real part λ, $\tau = 0$

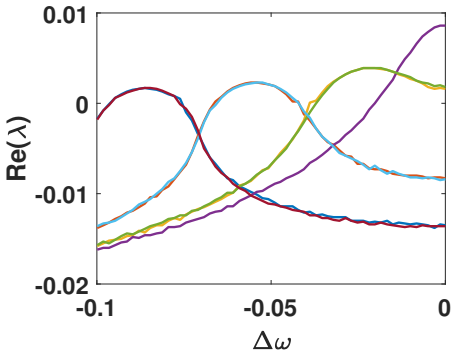

(b) Real part λ, $\tau = 100$

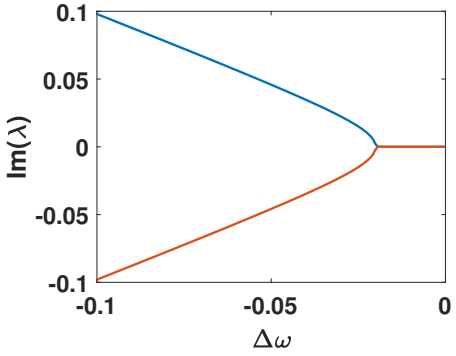

(c) Imaginary part λ, $\tau = 0$

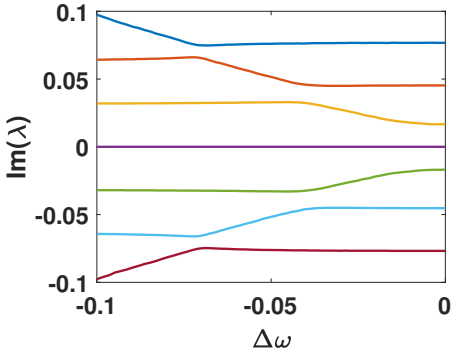

(d) Imaginary part λ, $\tau = 100$

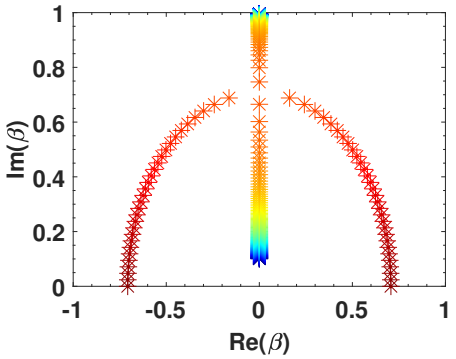

(e) Eigenvector evolution, $\tau = 0$

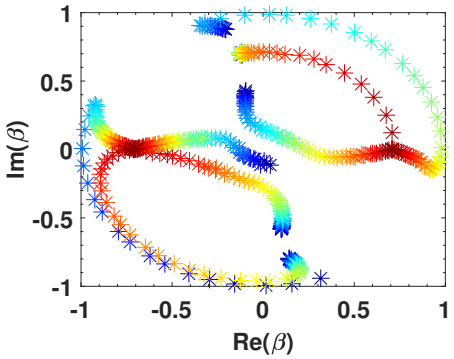

(f) Eigenvector evolution, $\tau = 100$

Figure 6.4. Eigenvalue and eigenvector plots for various delays. In all plots $\kappa = 0.02$ and $\theta\tau = 2n\pi$. With the exception of the zero-delay case, seven eigenvalue/eigenvector branches are plotted. Panels (a) & (c) are the real parts of the eigenvalues and panels (b) & (d) are the imaginary parts, the x-axes being $\Delta\omega/\kappa$ and the y-axes $\mathrm{Re}(\lambda)$ and $\mathrm{Im}(\lambda)$ respectively. Panels (e) & (f) show the evolution of the eigenvectors as a function of detuning, where the color of the points corresponds to the detuning (red corresponds to $\Delta\omega = 1$ and blue is the most negative $\Delta\omega$). The x-axis is the real part of β and the y-axis is the imaginary part of β, where β is the second component of the eigenvectors.

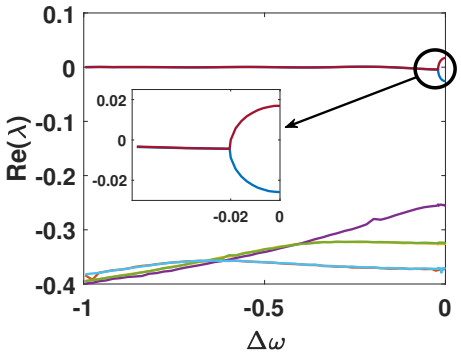

(a) Real part λ, $\tau = 10$

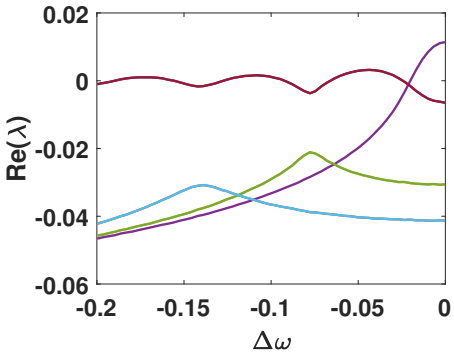

(b) Real part λ, $\tau = 50$

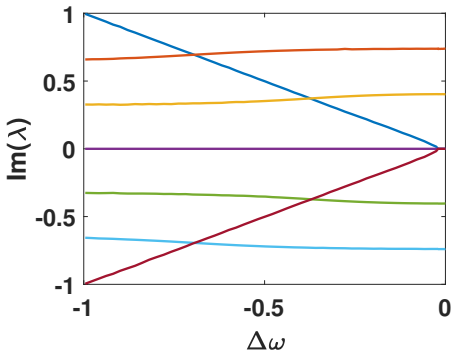

(c) Imaginary part λ, $\tau = 10$

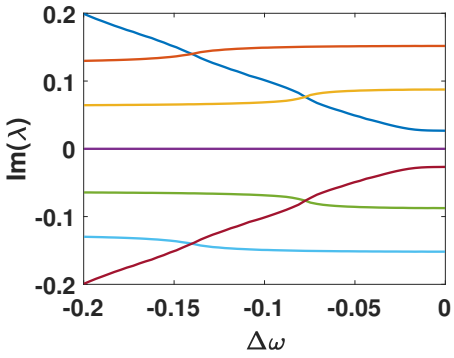

(d) Imaginary part λ, $\tau = 50$

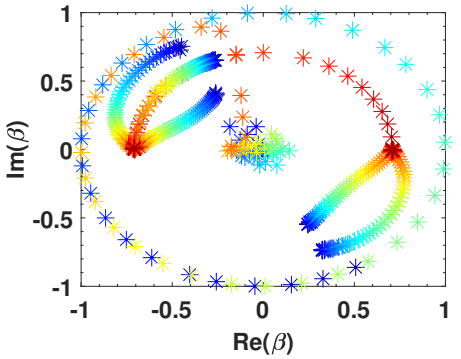

(e) Eigenvector evolution, $\tau = 10$

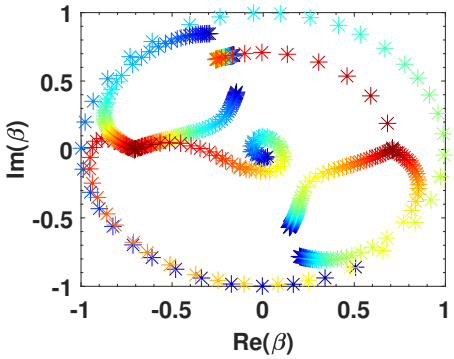

(f) Eigenvector evolution, $\tau = 50$

Figure 6.5. Eigenvalue and eigenvector plots for various delays. In all plots $\kappa = 0.02$ and $\theta\tau = 2n\pi$. Seven eigenvalue/eigenvector branches are plotted. Panels (a) & (c) are the real parts of the eigenvalues and panels (b) & (d) are the imaginary parts, the x-axes being $\Delta\omega/\kappa$ and the y-axes $\mathrm{Re}(\lambda)$ and $\mathrm{Im}(\lambda)$ respectively. Panels (e) & (f) show the evolution of the eigenvectors as a function of detuning, where the color of the points corresponds to the detuning (red corresponds to $\Delta\omega = 1$ and blue is $\Delta\omega$=-10/τ). The x-axis is the real part of β and the y-axis is the imaginary part of β, where β is the second component of the eigenvectors. The inset plot in panel (a) shows a close-up view of the eigenvalue degeneracy at $\Delta\omega = 1.022\kappa$.

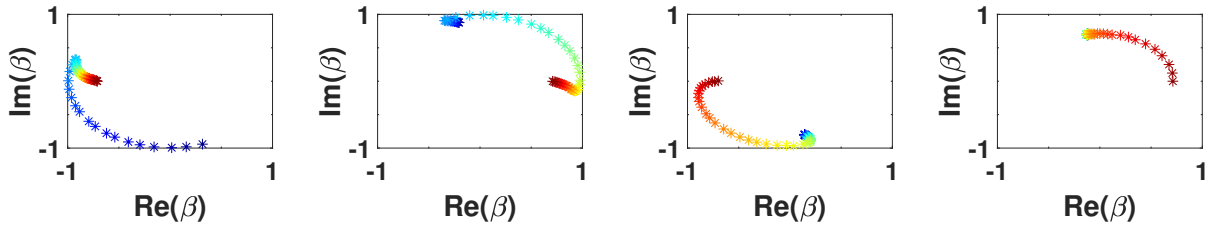

(a) $\tau = 100$, eigenvector 1 (b) $\tau = 100$, eigenvector 2 (c) $\tau = 100$, eigenvector 3 (d) $\tau = 100$, eigenvector 4

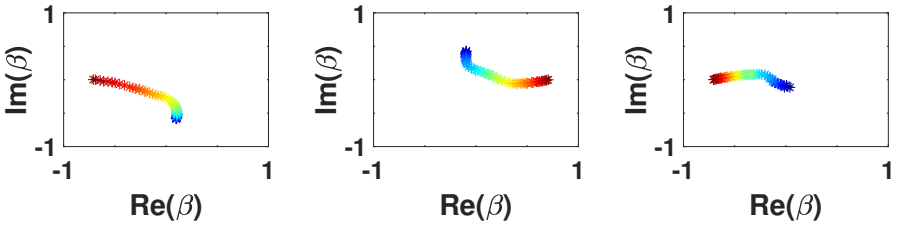

(e) $\tau = 100$, eigenvector 5 (f) $\tau = 100$, eigenvector 6 (g) $\tau = 100$, eigenvector 7

Figure 6.6. Individual eigenvector plots for $\tau = 100$. In all plots $\kappa = 0.02$ and $\theta\tau = 2n\pi$. Red points correspond to $\Delta\omega = 1$ and blue points correspond to $\Delta\omega$=-10/τ.

are symmetric about $\Delta\omega = 0$. Since the equations become infinite-dimensional for a non-zero delay, we have chosen only seven of the infinite eigenvalues to track as we change $\Delta\omega$ when $\tau \neq 0$. One of these eigenvalues comes from the intersection of F and G on the Im(λ)=0 axis, and the other six are the next intersections of F and G closest to the Im(λ)=0 axis, three on either side (see Fig. 6.3 for reference). Each eigenvalue is shown in a different color for ease of viewing. There are a few immediately noticeable differences between the zero-delay and nonzero-delay cases, one being that there is no longer a detuning at which the eigenvalues coalesce. Also, the real part of λ is no longer zero for $|\Delta\omega| > \kappa$, and similarly the imaginary part of λ is non-zero for $|\Delta\omega| < \kappa$. We will return to Fig. 6.4 e&f when we discuss the eigenvectors.

In Fig. 6.5 we explore the nature of the eigenvalues for a couple of intermediate τ values. If $\tau = 10$, as in Fig. 6.5a, the two most positive branches of Re(λ) (dark blue and red) coalesce at $\Delta\omega = 1.022\kappa$ (see inset to Fig. 6.5a). In the next section we will discuss why the coalescence happens at $\Delta\omega = 1.022\kappa$ instead of at $\Delta\omega = \kappa$. While these two branches mimic the behavior of the two real eigenvalue branches for $\tau = 0$, there are additional eigenvalues beneath the Re(λ)=0 axis which obviously do not coalesce at any point. The plot for the imaginary parts of the eigenvalues (Fig. 6.5c) also resembles the zero-delay case, with two branches (dark blue and red) coalescing at $\Delta\omega = 1.022\kappa$ and the rest being almost parallel to the Im(λ)=0 axis (orange, yellow, green, light blue). At $\Delta\omega = 1.022\kappa$, both the real and imaginary parts of these two eigenvalues coalesce; however, these are the *only* two branches whose real and imaginary branches simultaneously coalesce. Thus, for $\tau = 10$, we conclude that there is one EP in this detuning range, provided the corresponding eigenvectors are degenerate - we will return to this point in the next section and show that indeed, for $\tau = 10$, there is only one EP.

Upon increasing τ to more experimentally accessible delays ($\tau = 50$, Fig. 6.5), the most positive branches of Re(λ) (dark blue and red) oscillate about Re(λ)=0 with a greater amplitude (Fig. 6.5b), and the solutions under Re(λ)=0 become less negative compared to

$\tau = 10$. The imaginary parts of λ begin to deform as well (Fig. 6.5d) –the "v" shaped linear solutions (dark blue and red) no longer intersect the Im(λ)=0 solution, and the remaining branches become less parallel to Im(λ)=0. There is no detuning at which we see any pair of eigenvalues coalesce. When τ is very large ($\tau = 100$, a typical experimental value) the solutions for Re(λ) do not bear any resemblance to the zero-delay case, and there are no continuous "v" shaped solutions in the Im(λ) plot (Fig. 6.4b,d). Again, we do not see any eigenvalue degeneracy for $\tau = 100$. Since an EP requires not only that eigenvalues coalesce, but also that the corresponding eigenvectors are parallel, we now investigate the eigenvectors generated by these seven eigenvalues for various delays.

6.3.2 Eigenvector Results

To put the eigenvector results in context, we first discuss the well-known result for zero delay case, shown in Fig. 6.4e. When the detuning is most negative (blue), one eigenvector starts from $\beta = (0, 1)$ and moves toward $\beta = (0, \frac{1}{\sqrt{2}})$ as detuning is increased towards zero, while the other eigenvector starts near $\beta = (0, 0.1)$ and evolves upward to $\beta = (0, \frac{1}{\sqrt{2}})$. At $\Delta\omega = \kappa$ (the zero-delay PT transition) the two eigenvectors bow outward and eventually settle to $\beta = \pm(\frac{1}{\sqrt{2}}, 0)$ at $\Delta\omega = 0$. When $\Delta\omega = \kappa$ the two eigenvectors are degenerate, with $\beta = (0, \frac{1}{\sqrt{2}})$, and since their eigenvalues are also degenerate at that detuning we can say that there exists an EP at the PT transition.

Fig. 6.4f & 6.5e,f show eigenvector plots for various τ. For non-zero delays we plot seven eigenvector trajectories corresponding to the seven eigenvalues, and the color of each point represents the detuning value. In these figures the detuning is swept from $-10/\tau$ (blue) to 0 (red) with 60 equally spaced detunings between these two values. These trajectories, which show the second compontent of the eigenvectors (β), were generated by substituting the eigenvalues into Eq. (6.8). Since we set the first component of the eigenvectors α to be 1 the evolution of β therefore represents the evolution of the eigenvector. The behavior of

the eigenvectors is more complicated than the eigenvalue pictures, yet for all delays (except τ=0) the plots are similar.

To untangle the behavior of individual eigenvectors we show each of the seven eigenvectors for $\tau = 100$ in individual panels in Fig. 6.6 a-g. Panels (a) and (b) show two eigenvector trajectories that spiral clockwise inward as $\Delta\omega$ approaches zero, which form the circular shape see in Fig. 6.4f. The other five trajectories evolve much slower, as seen in panels (e), (f), and (g), where the spacing between each data point is smaller than in panels (a) and (b). In panels (c) and (d) the eigenvectors spiral clockwise outward, moving faster as the detuning approaches zero. These eigenvectors are, generally, always complex, as opposed to the solutions for $\tau = 0$ where the eigenvectors are purely imaginary for $\Delta\omega/\kappa > 1$. It's important to point out that all eigenvectors approach either $(\frac{1}{\sqrt{2}},\frac{1}{\sqrt{2}})$ or $(\frac{1}{\sqrt{2}},\frac{-1}{\sqrt{2}})$ as $\Delta\omega$ approaches 0. This is due to the fact that when $\Delta\omega$=0 the Hamiltonian (Eq. (6.3)) becomes a multiple of σ_x, and the eigenvectors of σ_x are $(\frac{1}{\sqrt{2}},\frac{1}{\sqrt{2}})$ and $(\frac{1}{\sqrt{2}},\frac{-1}{\sqrt{2}})$). To prove this we first write the Hamiltonian in Eq. (6.3) as

$$\begin{pmatrix} 0 & f(\lambda) \\ f(\lambda) & 0 \end{pmatrix}, \tag{6.9}$$

where $f(\lambda) = \kappa \mathrm{e}^{-\lambda\tau}\mathrm{e}^{-\mathrm{i}\theta\tau}$. The characteristic equation becomes λ^2 - $f^2(\lambda) = 0$, or $\lambda = \pm f(\lambda)$, and so the eigenvector evaluation becomes

$$\lambda \begin{pmatrix} \alpha \\ \beta \end{pmatrix} = f(\lambda) \begin{pmatrix} 0 & 1 \\ 1 & 0 \end{pmatrix} \begin{pmatrix} \alpha \\ \beta \end{pmatrix} \Longrightarrow \begin{pmatrix} \alpha \\ \beta \end{pmatrix} = \pm \begin{pmatrix} \beta \\ \alpha \end{pmatrix}, \tag{6.10}$$

which give the usual σ_x eigenvectors, independent of $\kappa\tau$.

6.3.3 Exceptional Points Results

From visually examining the eigenvector plots it's unclear where (or if) there are any eigenvector degeneracies. By increasing the detuning resolution and numerically combing

the raw data we find that there *are* detunings where the eigenvector degeneracies arise for the same parameters where the corresponding eigenvalues coalesce. In other words, the degeneracies occur between the same *pairs* of eigenvales/eigenvectors (the same F and G intersections). We can, therefore, confirm the existence of EPs, although the exact conditions for their existence are somewhat complicated, as we will show later.

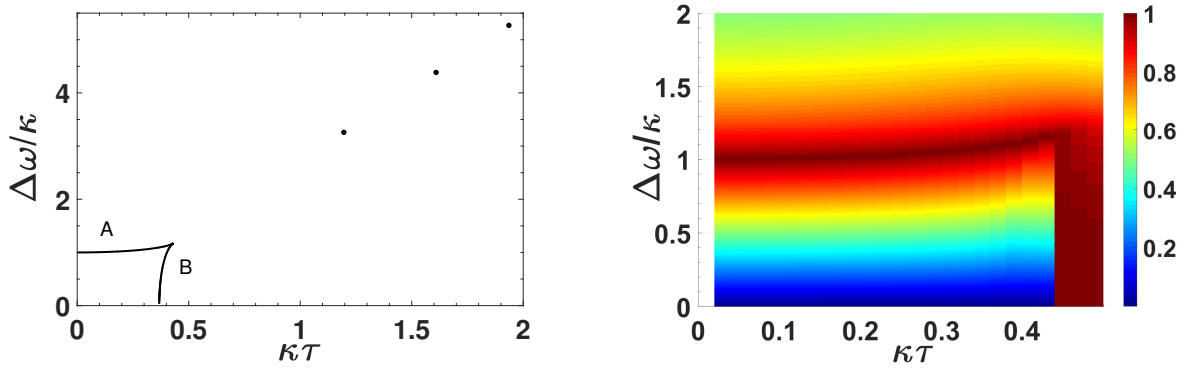

(a) Exceptional points as a function of $\kappa\tau$ (when $\theta\tau = 2n\pi$). The x-axis is $\kappa\tau$ and the y-axis is $\Delta\omega/\kappa$. There is a transition from continuous to discrete solutions at $\kappa\tau = 1/\sqrt{2e}$. Curve A is generated by the Lambert W function's 0^{th} branch and curve B is generated by the -1^{st} branch.

(b) Magnitude of the normalized complex inner-product for the two eigenvectors responsible for the eigenvalue degeneracy solutions closest to the zero-delay case (near $\Delta\omega/\kappa = 1$, curve A). When the magnitude is equal to 1 the two eigenvectors are parallel.

Figure 6.7. Exceptional point behavior as a function of $\kappa\tau$. Panel *a* shows exceptional points as a function of $\kappa\tau$ and panel *b* shows the magnitude of the complex inner-product of two specific eigenvectors responsible for the exceptional points in the region $0 < (\kappa\tau)^2 \leq 1/2e$.

Figure 6.7a is a summary plot of the EPs that arise in our system on a $\Delta\omega/\kappa$ vs $\kappa\tau$ plane. Curve A shows continuously occurring EPs up to a $\kappa\tau$ of about 0.5. Similarly, curve B is a series of continuously occurring EPs for $\kappa\tau$ between approximately 0.4-0.5. We conclude from these features that there is a range of $\kappa\tau$ values, $\kappa\tau < 0.4$, for which there is only one EP, and for $0.4 < \kappa\tau < 0.5$ there are two EPs. The existence of this latter regime is a direct consequence of the time-delayed coupling — that is, for zero time-delay there are no EPs near these values. We will show later that the exact condition for one EP is that $\kappa\tau < 1/e$.

This EP lies very close to the parameters that give rise to an EP for the zero delay case, i.e. $\Delta\omega = \kappa$. The slight concavity of curve A is the reason that the EP in Fig. 6.5a,c is at $\Delta\omega = 1.022\kappa$. The exact condition for two EPs is $1/\mathrm{e} \leq \kappa\tau \leq 1/\sqrt{2\mathrm{e}}$, with one EP very close to the zero-delay PT-symmetric EP (curve A in Fig. 6.7a) and the other (curve B in Fig. 6.7a) starting from $\Delta\kappa = 0$ and rapidly approaching curve A. For $\kappa\tau > 1/\sqrt{2\mathrm{e}}$ there are broadly spaced EPs for certain $\kappa\tau$ with regions in between without any EPs. Again, we emphasize that these conditions for one, two, or zero EPs were first determined numerically and later derived analytically, as described in the next section.

Figure 6.7b displays the magnitude of the complex inner-product of the two eigenvectors which produce the exceptional points near $\Delta\omega/\kappa = 1$ — not *all* eigenvector pairs are shown. When the magnitude of the inner-product is 1 the two eigenvectors are degenerate, and from the plot it's clear that this curve matches the same curve in Fig. 6.7a (curve A). Beyond the breaking point $\kappa\tau = 1/\sqrt{2\mathrm{e}}$ there is a clear phase transition, and the inner-product displays vastly different behavior, instantly jumping to completely different values.

6.3.4 Phase Accumulation

In the preceding discussion we have neglected the phase-accumulation term, $\theta\tau$, to consider the simplest time-delay problem and emphasize the features that lead to EPs. Non-zero phase-accumulation does have some effect on the existence of EPs, and so we briefly summarize the consequences of its inclusion. With the introduction of non-zero $\theta\tau$ in Eq. (6.6a&b) the cosine and sine terms pick up a phase shift, and the solutions for λ are no longer complex conjugate pairs (the F and G plots are no longer symmetric about the Re(λ)=0 axis). Furthermore, since Eq. (6.6b) has a phase shift θ in the sine term there can be no solutions with Im(λ)=0. A consequence of this is that now we will only track *six* eigenvalues/eigenvectors for non-zero $\theta\tau$. The lack of symmetry in F and G is reflected in Fig 6.8a&b, where the six eigenvalues for $\tau = 100$ appear as distinct curves, in contrast to the corresponding $\theta\tau = 2n\boldsymbol{\pi}$ case in Fig. 6.4b&d wherein three pairs of eigenvalues coincide and the seventh

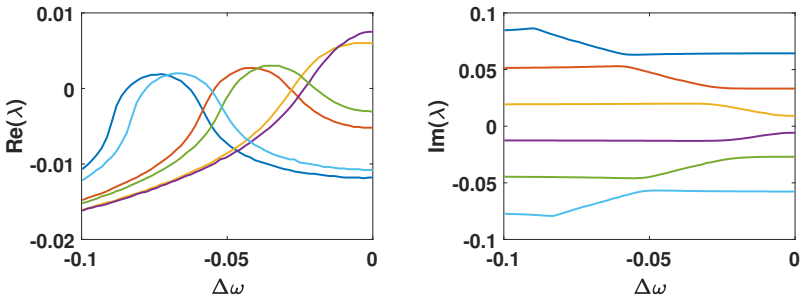

(a) Real part λ (b) Imaginary part λ

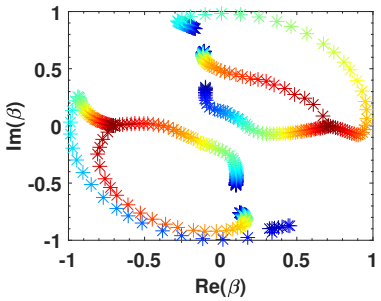

(c) Eigenvectors

Figure 6.8. Plots of eigenvalues and eigenvectors for $\kappa = 0.02$, $\tau = 100$, and $\theta\tau = 2.4$. Eigenvalue solutions are no longer complex conjugate pairs, but overall behavior is very similar to the $\theta\tau = 2n\pi$ case. Axes and colors are the same as in Figures 6.4 and 6.5.

is distinct. In particular, the Im(λ) plot clearly shows that the eigenvalue solutions are not symmetric about the Im(λ)=0 axis, meaning that λ no longer form complex-conjugate pairs. The eigenvectors (Fig. 6.8c) behave similarly to the zero phase accumulation case, with all eigenvectors approaching $(\frac{1}{\sqrt{2}},\frac{1}{\sqrt{2}})$ or $(\frac{1}{\sqrt{2}},\frac{-1}{\sqrt{2}})$ as $\Delta\omega$ approaches 0. A notable difference we find with the inclusion of phase accumulation is that for $\kappa\tau \leq 1/\sqrt{2\mathrm{e}}$ there are no values of $\theta\tau$ which allow for degenerate eigenvalues/eigenvectors. Interestingly, for any value of $\kappa\tau$ greater than $1/\sqrt{2\mathrm{e}}$, there are only two supplementary values (i.e. add up to π) of $\theta\tau$ that produce EPs for *specific* detunings. This result will be discussed in more detail in the following section.

6.4 Analytic Results

Time-delayed differential equations are often analytically intractable, but the Lambert W function can be used under some conditions to extract analytical solutions. In the following, the W function is used to get results that support our numerical observations discussed in the previous section. We refer the reader to Ref. [81] for an excellent description of the Lambert W function.

6.4.1 Second-order EPs

The characteristic equation for the Hamiltonian in Eq. (6.3) is given by:

$$\lambda^2 + \Delta\omega^2 - \kappa^2 \mathrm{e}^{-2\tau(\lambda+\mathrm{i}\theta)} = 0, \tag{6.11}$$

which can be factored as

$$\lambda^2 + \Delta\omega^2 - \kappa^2 \mathrm{e}^{-2\tau(\lambda+\mathrm{i}\theta)} = (\lambda - a_1)(\lambda - a_2)(\lambda - a_3)... = 0, \tag{6.12}$$

where a_n are solutions to Eq. (6.11). In the case of a second order eigenvalue degeneracy, Eq. (6.12) can be written as

$$(\lambda - a_1)^2(\lambda - a_2)(\lambda - a_3)... = 0, \tag{6.13}$$

where a_1 is the degenerate eigenvalue; a consequence of this degeneracy is that the *derivative* of Eq. (6.13) with respect to λ is also equal to 0, since the term $(\lambda - a_1)$ is present in all terms after differentiation. Higher order degeneracies are treated similarly – we will address them later in this section. The derivative of Eq. (6.11) is

$$2\lambda + 2\tau\kappa^2 \mathrm{e}^{-2\tau(\lambda + \mathrm{i}\theta)} = 0, \tag{6.14}$$

and using Eq. (6.14) with Eq. (6.11) we attempt to solve for the detuning $\Delta\omega$ for which there is a second order degeneracy. After eliminating λ we arrive at

$$1 \mp \sqrt{1 - (2\Delta\omega\tau)^2} - 2\kappa^2\tau^2 \mathrm{e}^{-2\mathrm{i}\theta\tau} \mathrm{e}^{1 \mp \sqrt{1-(2\Delta\omega\tau)^2}} = 0, \tag{6.15}$$

which can be written as

$$-z\mathrm{e}^{-z} = -2\kappa^2\tau^2 \mathrm{e}^{-2\mathrm{i}\theta\tau}, \tag{6.16}$$

where $z = 1 \mp \sqrt{1 - (2\Delta\omega\tau)^2}$. The solutions of Eq. (6.16) are given by the Lambert W function:

$$z = \mathrm{W}_n(-2\kappa^2\tau^2 \mathrm{e}^{-2\mathrm{i}\theta\tau}) \tag{6.17}$$

where n is an integer. Eq. (6.16) is written in the standard form of the Lambert W function, which is defined as the inverse of $f(\omega) = \omega \mathrm{e}^{\omega}$. The Lambert W function is commonly found in spectral analyses of systems with time delay due to the inclusion of terms like $\mathrm{e}^{\lambda\tau}$ in the characteristic equations [81]. It is real valued only when $f(\omega)$ is real and greater than -1/e

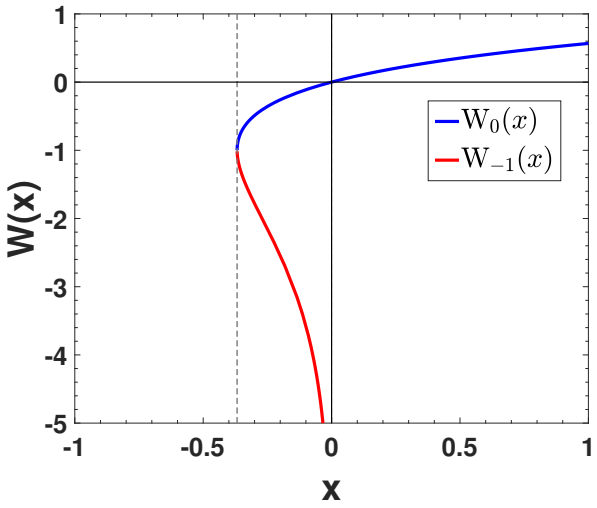

Figure 6.9. The Lambert W function's real branches for real x. The blue curve is $\mathrm{W}_0(x)$ and the red is $\mathrm{W}_{-1}(x)$. Note the turning point at $x = -1/\mathrm{e}$, marked with a dashed line.

(Fig. 6.9). From Eq. (6.17) we derive an expression for the critical detuning $\Delta\omega_c$ at which a degeneracy occurs:

$$\Delta\omega_c = \frac{\pm 1}{2\tau}\sqrt{1 - [\mathrm{W}_n(-2\kappa^2\tau^2\mathrm{e}^{-2\mathrm{i}\theta\tau}) + 1]^2}. \tag{6.18}$$

We require that $\Delta\omega_c$ be real, which means the term under the radical must be positive. Assuming a general solution $\mathrm{W}_n(-2\kappa^2\tau^2\mathrm{e}^{-2\mathrm{i}\theta\tau}) = a + \mathrm{i}b$ results in the requirement that W_n have the form $\mathrm{W}_n(-2\kappa^2\tau^2\mathrm{e}^{-2\mathrm{i}\theta\tau}) = a$ or $\mathrm{W}_n(-2\kappa^2\tau^2\mathrm{e}^{-2\mathrm{i}\theta\tau}) = -1 + \mathrm{i}b$, where a and b are real. This requirement places constraints on the argument of W_n, and therefore the parameter space swept by κ, τ, and θ is narrowed.

When substituted into Eq. (6.18), the first solution $\mathrm{W}_n(-2\kappa^2\tau^2\mathrm{e}^{-2\mathrm{i}\theta\tau}) = a$ gives

$$\Delta\omega_c = \frac{\pm 1}{2\tau}\sqrt{-(a^2 + 2a)}, \tag{6.19}$$

which, because $\Delta\omega_c$ must be real, produces an additional requirement that a must lie between -2 and 0. Now, since the Lambert W function is only real-valued when the argument

is purely real and is greater than $-1/e$, $-2\kappa^2\tau^2 e^{-2i\theta\tau}$ must be real and greater than $-1/e$, which implies that the phase accumulation must be a multiple of π, $\theta\tau = n\pi$ (where n is an integer). When evaluating the Lambert W function with a real argument there are two branches that can produce purely real outputs, namely the 0 and -1 branches. A plot of these real-valued solutions is given in Fig. 6.9. The $W_0(x)$ branch (blue) is bounded on the left by the point ($-1/e$, -1) and goes to infinity as x increases, while the $W_{-1}(x)$ branch (red) is bounded on the left by ($-1/e$,-1) and travels down asymptotically to the y-axis as x approaches zero. $W_{-1}(x)$ has no real solutions for $x > 0$. It's clear from the graph that $W_0(x)$ satisfies $-2 \leq W_0(x) \leq 0$ for all $-1/e \leq x \leq 0$; however, $W_{-1}(x)$ satisfies $-2 \leq W_{-1}(x) \leq 0$ only for $-1/e \leq x \leq 2/e^2$. This translates into the following constraints on $\kappa\tau$: for the $W_0(x)$ branch $\kappa\tau$ must satisfy $0 \leq 2\kappa^2\tau^2 \leq 1/e$, and for the W_1($x$) branch $\kappa\tau$ must satisfy $2/e^2 \leq 2\kappa^2\tau^2 \leq 1/e$.

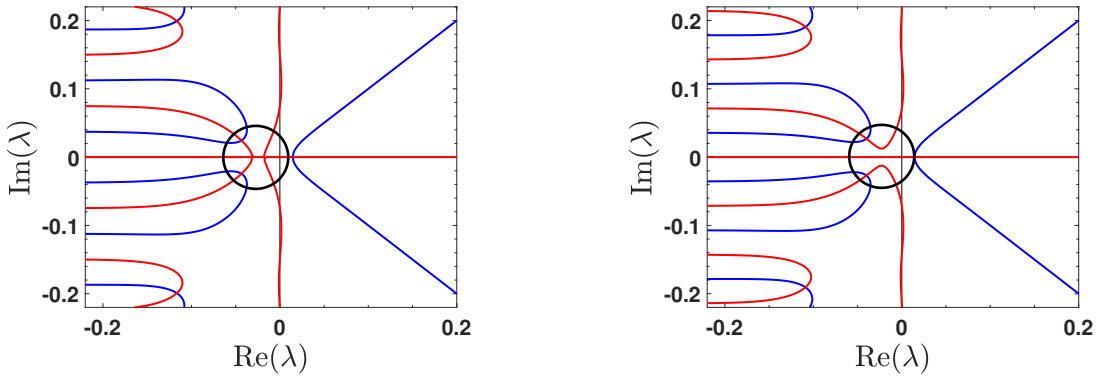

(a) Before breaking ($\kappa\tau = 0.42$)

(b) Before breaking ($\kappa\tau = 0.44$)

Figure 6.10. Breaking of G (red) as $(\kappa\tau)^2$ crosses 1/2e. The black circle indicates the breaking point.

In the context of the F and G equations, the existence of the W_0 solution depends on the continuity of the G branch that straddles the Re(λ)=0 axis — when $2\kappa^2\tau^2 > 1/e$, that branch becomes discontinuous near the origin and the two "antennae" branches of F will never merge (Fig. 6.10 a & b). The existence of the W_{-1} solution is related to the merging of the first two tongues of the F plot – when $2/e^2 \leq 2\kappa^2\tau^2 \leq 1/e$, there exists a detuning for

which the ±1 tongues merge into the 0th tongue, and the merging location on the Im(λ)=0 axis is determined by where the 0th tongue of G crosses the Im(λ)=0 axis (Fig. 6.11 a & b).

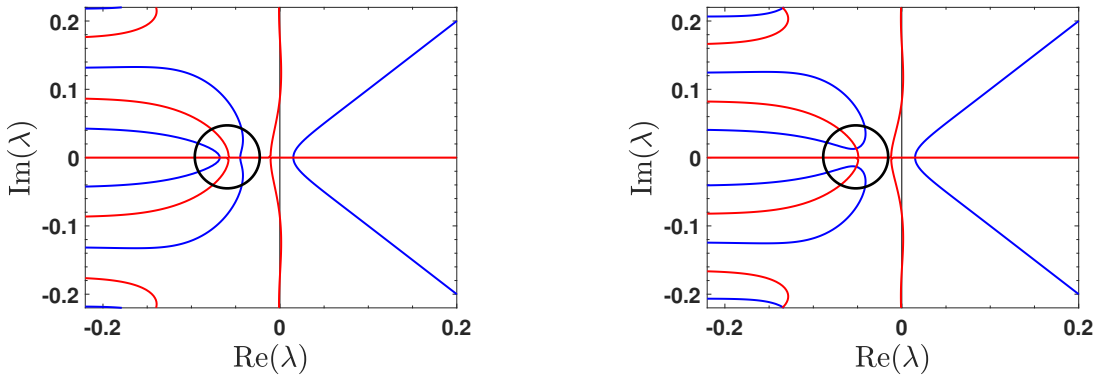

(a) Before breaking ($\kappa\tau = 0.36$) (b) Before breaking ($\kappa\tau = 0.38$)

Figure 6.11. Merging of F tongues (blue) as $\kappa\tau$ crosses 1/e. $\Delta\omega$=0 for both plots. The black circle indicates the breaking point.

From these constraints we conclude that there exists a single exceptional point for $0 \leq \kappa\tau \leq 1/\mathrm{e}$ and two for $1/\mathrm{e} \leq \kappa\tau \leq 1/\sqrt{2\mathrm{e}}$, which is in exact agreement with our numerical results. The corresponding $\Delta\omega_c$ can be found by evaluating Eq. (6.18) with the appropriate branch numbers (0 and -1) (Fig. 6.7a). Of special note are the solutions coming from W_0, whose detunings are very close to the exceptional point detunings in the zero-delay case ($\Delta\omega = \kappa$).

The second solution of $\mathrm{W}_n = -1 + \mathrm{i}b$ is more complicated. Starting from Eq. (6.17),

$$-1 + \mathrm{i}b = \mathrm{W}_n(-2\kappa^2\tau^2\mathrm{e}^{-2\mathrm{i}\theta\tau}) \tag{6.20}$$

we take the inverse and solve for θ:

$$\mathrm{e}^{-2\mathrm{i}\theta\tau} = \frac{(-1 + \mathrm{i}b)}{-2\mathrm{e}\kappa^2\tau^2}\mathrm{e}^{\mathrm{i}b}. \tag{6.21}$$

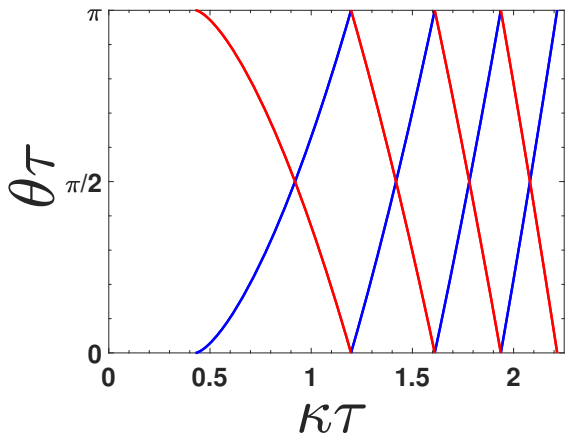

Figure 6.12. Solutions for $\theta_c\tau$ given $\kappa\tau$. The two solutions, blue and red, are supplementary.

Taking the complex logarithm of both sides and separating the real and imaginary parts allows us to solve for b:

$$b^2 = (2\mathrm{e}\kappa^2\tau^2) - 1. \tag{6.22}$$

When substituted, the resulting equation provides solutions for θ_c, the phase accumulations for which, given both κ and τ, there exists an eigenvalue degeneracy:

$$\theta_c\tau = \frac{1}{2}\left[\pm\sqrt{(2\mathrm{e}\kappa^2\tau^2)^2 - 1} \mp \arctan\left(\sqrt{(2\mathrm{e}\kappa^2\tau^2)^2 - 1}\right)\right] + n\boldsymbol{\pi}, \tag{6.23}$$

where n is an integer. A plot of $\theta_c\tau$ vs. $\kappa\tau$ is shown in Fig. 6.12. For $\kappa\tau \leq 1/\mathrm{e}$ there are no values of θ that produce a degeneracy, which agrees with our previous conclusion (when $\mathrm{W}_n = a$) and is a consequence of requiring that θ be real. When $\kappa\tau > 1/\mathrm{e}$ there are two supplementary solutions for $\theta_c\tau$ in the range $0 \geq \theta\tau \geq \boldsymbol{\pi}$, their sum being $\boldsymbol{\pi}$. It should be noted that when $\theta\tau \neq n\boldsymbol{\pi}$ there is no region where the exceptional points continuously change; rather, the degeneracies are isolated points in the $\kappa\tau$ vs. $\frac{\Delta\omega_c}{\kappa}$ plane. Of special note are the points in Fig. 6.12 where $\theta_c\tau$=0. These are the sources of the isolated EPs for $\kappa\tau > 1/\sqrt{2\mathrm{e}}$ in Fig. 6.7a.

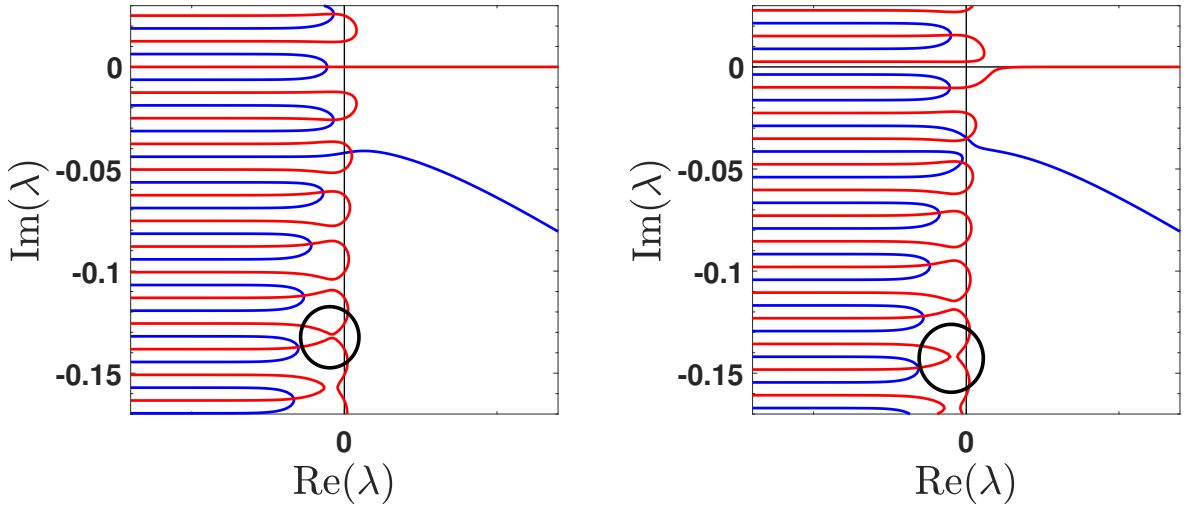

(a) $\theta\tau = 0$ (b) $\theta\tau = 1.25$

Figure 6.13. Demonstration of tongue merging as $\theta\tau$ varies. Here the -5th tongue merges with the -6th as $\theta\tau$ increases, the black circle indicates the merging point. $\kappa\tau$ and $\Delta\omega$ are fixed for both plots.

The detunings associated with these degeneracies can be found using Eq. (6.18) with the proper values of $\kappa\tau$ and $\theta\tau$; however, the proper branch of W_n must be used as well. Graphically, the solutions provided by Eq. (6.23) come from the separation of tongues in the G plot as $\kappa\tau$ increases. The proper index in Eq. (6.18) is chosen based on the observation of which tongue m is being created – explicitly, the index is $n = m \pm 1$ (positive for tongues above the Im(λ)=0 axis and vice versa). For example, when $\kappa\tau$=2.5 and $\theta\tau$=0.51 we see that the -5th tongue is separating, and therefore we use $n = -6$ in Eq. (6.18), giving us the proper detuning $\Delta\omega/\kappa$=6.8 (see Fig. 6.13 for a visualization of this merging process).

6.4.2 Higher-order EPs

Of course, all the preceding work is for a second order degeneracy; can this system exhibit higher order exceptional points? For a third order degeneracy, we again start with the assertion that Eq. (6.11) can be factored as

$$\lambda^2 + \Delta\omega^2 - \kappa^2 \mathrm{e}^{-2\tau(\lambda+\mathrm{i}\theta)} = (\lambda - a_1)(\lambda - a_2)(\lambda - a_3)... = 0, \tag{6.24}$$

where a_n are solutions to Eq. (6.11). In the case of a third order eigenvalue degeneracy, Eq. (6.12) can be written as

$$(\lambda - a_1)^3(\lambda - a_2)(\lambda - a_3)... = 0, \tag{6.25}$$

where a_{i} are solutions to Eq. (6. 24). Now both the first *and* second derivatives of Eq. (6.24) must be zero – these derivatives, along with the original equation, produce a set of three coupled equations that can be solved for the degenerate λ and the detunings $\Delta\omega$ for which they occur:

$$\lambda^2 + \Delta\omega^2 - \kappa^2 \mathrm{e}^{-2\tau(\lambda+\mathrm{i}\theta)} = 0 \tag{6.26a}$$

$$2\lambda + 2\tau\kappa^2 \mathrm{e}^{-2\tau(\lambda+\mathrm{i}\theta)} = 0 \tag{6.26b}$$

$$1 - 2(\kappa\tau)^2 \mathrm{e}^{-2\tau(\lambda+\mathrm{i}\theta)} = 0 \tag{6.26c}$$

By rearranging Eq. (6.26c), it's clear that the exponential term has to satisfy the relation $\mathrm{e}^{-2\tau(\lambda+\mathrm{i}\theta)} = 1/2(\kappa\tau)^2$. Since the right-hand side of the expression is always real, this constrains $\theta\tau$ to be an integer multiple of $\pi/2$. This expression, when substituted into Eq. (6.26b), gives the singular eigenvalue for which there exists a third-order degeneracy: $\lambda = -\frac{1}{2\tau}$. With this eigenvalue we can then evaluate Eq. (6.26a) and find the detunings for

which this degeneracy occurs: $\Delta\omega = \pm\frac{1}{2\tau}$. Taking the eigenvalue solution and substituting it back into Eq. (6.26c) results in a familiar expression for the constraints on κ and τ:

$$\kappa\tau = \frac{1}{\sqrt{2\mathrm{e}}} \tag{6.27}$$

This means that there is only a single combination of $\kappa\tau$ for which there exists a third-order exceptional point (Fig. 6.14) – the corresponding eigenvectors also coalesce at the specified detuning. This value of $\kappa\tau$ places the third-order EP at the cusp formed by the second-order EP curves A and B in Fig. 6.7a.

For the case of $N \geq 4$ degeneracies, Eq. (6.25) becomes

$$(\lambda - a_1)^N(\lambda - a_2)(\lambda - a_3)... = 0, \tag{6.28}$$

and the N-th derivative of Eq. (6.28) is then

$$-\kappa^2(-2\tau)^N\mathrm{e}^{-2\tau(\lambda+\mathrm{i}\theta)} = 0. \tag{6.29}$$

For any non-zero delay or feedback strength this equation has no solutions for λ, and thus there are no N-th order eigenvalue degeneracies. The system only allows for second and third-order exceptional points.

We see from the discussion in this section that the major features that were observed numerically for a time-delayed PT-symmetric system can be understood analytically via the use of the W function. The analytic approach not only elucidates some of the numerically calculated features, but also allows one to precisely establish the conditions under which certain features arise.

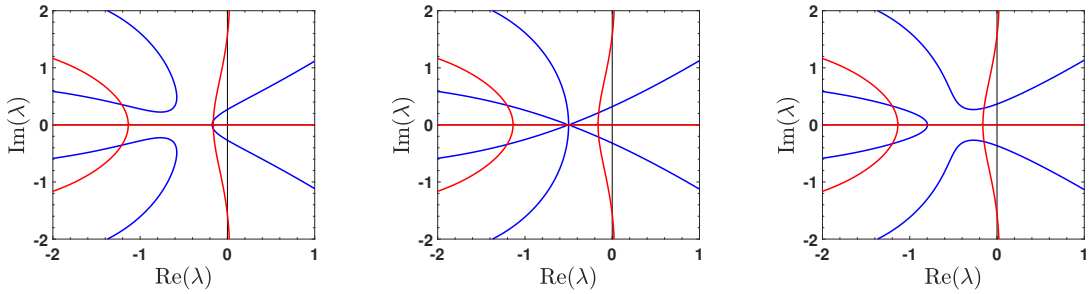

(a) $\Delta\omega = 0.48\tau$ (b) $\Delta\omega = 0.5\tau$ (c) $\Delta\omega = 0.52\tau$

Figure 6.14. Third-order degeneracy. For all three plots $(\kappa\tau)^2 = 1/2\mathrm{e}$ (with $\tau = 1$). As the detuning is increased, three eigenvalue solutions move closer together, eventually merging at $\lambda = -1/2\tau$ when $\Delta\omega = 1/2\tau$.

6.5 Discussion

The work presented in this section has demonstrated via numerical modeling and analytic derivations that a time-delay coupled, PT-symmetric system displays rich EP behavior when compared with the corresponding zero-delay dimer case. By tuning the system's delay time, coupling rate, or phase accumulation, we can move the system through three distinct regions in the exceptional point landscape, i.e. regions with 0, 1, or 2 second-order exceptional points. In addition, the system can exhibit a third-order exceptional point provided the delay and coupling rate are carefully chosen. Our experimental and numerical results have verified predictions, based on the Hamiltonian in Eq. (6.3), about the period and amplitude of the "sideband transitions" in Fig. 6.2 and the existence of the phase transition near $\Delta\omega = \kappa$, demonstrating the effectiveness of our simplified Hamiltonian [44]. The impact of these exceptional points on intensity behavior is still not well understood, however, as numerical simulations based on the full rate equations (Eqns. (6.2a-d)) show no evidence of any major transition at $\kappa\tau = 1/\sqrt{2\mathrm{e}}$ or any other transition point (Figure 6.15). In both plots there is a clear phase transition near $\Delta\omega = \kappa$, but only in the left plot is that transition supported by an exceptional point. It's possible that the added complexity of carrier population interaction and gain saturation wash out the exceptional point behavior,

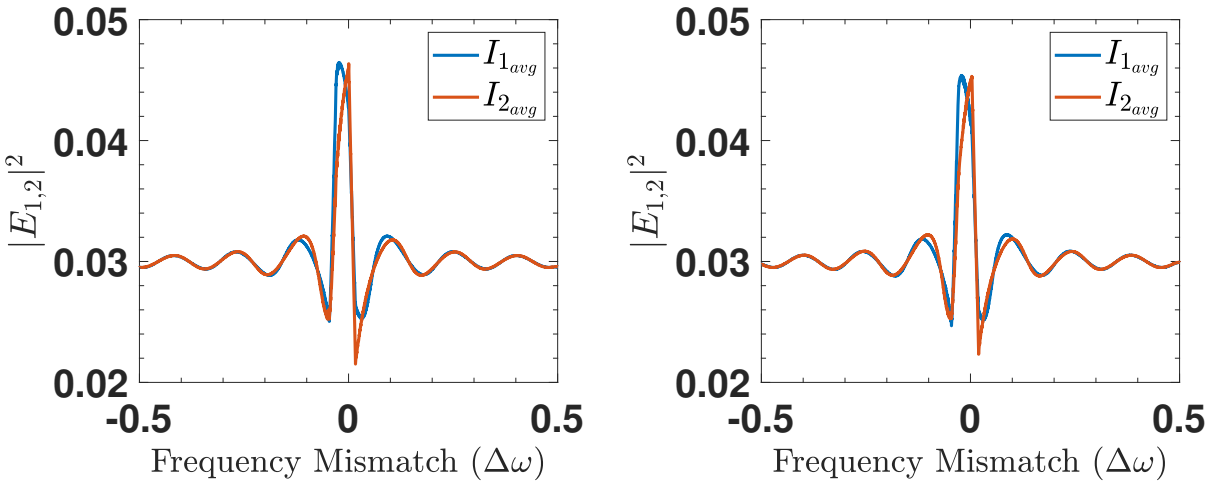

(a) $\kappa\tau = 0.42$ (b) $\kappa\tau = 0.44$

Figure 6.15. Numerical simulation of SCL intensities. For both plots $\kappa = 0.02$. Despite the lack of exceptional points for $\kappa\tau = 0.44$ in the pseudo-2x2 model, the right plot is nearly identical to the left, each with a PT transition near $\Delta\omega = \kappa$.

or it could be that the effects of this exceptional point breaking predicted by our pseudo-2x2 model produce more subtle effects, perhaps in the carrier populations, phase behaviors, etc.. The focus of this section has been on the EPs that arise in the time-delayed effective Hamiltonian, and the delay-coupled SCL system provides a good test bed for verifying the predictions made here. Among the open questions that can be addressed in future work are the effects of carrier population interaction and gain saturation on the EPs, and whether the effects of EPs in a time-delayed system produced observable signature in the carrier populations and phase-locking evolution.

7. SUMMARY

This work describes our research on the effects of time-delay in an optical implementation of PT-symmetry. We used a system of two delay-coupled semiconductor lasers as a test bed to study the interaction of nonzero delay with traditionally PT-symmetric features, namely a phase transition from bounded to unbounded laser intensities. This transition, the domewidth, was analytically described using a reduced Hamiltonian model, and predictions were checked via numerical solutions from the LK rate equation model and experimental data. Additionally we found that nonzero delay gave rise to broad intensity oscillations in the bounded region, when the laser frequency detuning was larger than the coupling strength, and we characterized the period and amplitude of these oscillations analytically, numerically, and experimentally. Good agreement between all three for both the sideband oscillations and domewidth, though there is room for improvement. This agreement is in spite of large gaps in complexity between the analytic model, the numerical model, and the experiment. We also numerically and analytically investigated the impact of nonzero delay on the exceptional points in the Hamiltonian model, finding that the presence of nonzero delay has the effect of warping the existing EPs, and for some parameter values either creating additional EPs or destroying them completely. The eigenvalues and eigenvectors associated with this Hamiltonian were also investigated, both in the exceptional point work and in the domewidth/sideband work. It was found that an understanding of the reduced model's eigenvalues provided good explanations for the SCL intensity behavior, again in spite of large gaps in complexity between the Hamiltonian model and experiment.

Future work will include an examination of other system aspects and extending this system beyond its current limits. Over the past few years incursions have been made into the following territories, but there has not been enough time to develop significant results:

- How does the addition of quantum noise affect the delay-induced intensity features. Are these robust in the presence of noise?

- The carrier inversion as a function of system parameters has not been thoroughly addressed. Is there anything significant to be discovered concerning the effects of time-delay? To our knowledge the carrier inversion only mirrors the intensity profiles.

- By separating the phase and amplitude in the LK equations, in the limit of zero delay an Adler equation is obtained for phase locking that has the same transition requirement as the zero-delay PT-transition. How is phase locking between SCLs impacted by delay?

- SCL frequency is also dependent on the injection current. Therefore we can experimentally change the frequency detuning by varying the lasers' pump currents. This was briefly explored by both Dr. Joseph Suelzer and more recently by graduate student Luke Thomas. How are intensity profile features impacted by delay and coupling in this setup?

- Currently both lasers experience the same coupling strength κ. What happens in the case of uneven coupling, or unidirectional coupling?

- What are the consequences of extending the system to three coupled lasers?

- With easy control over system parameters, and with the help of additional polarizers and rotators, is it possible to engineer exceptional point surfaces in the system?

These questions remain for future graduate students to explore.

REFERENCES

[1] J. M. Dudley, "Light, lasers, and the nobel prize," *Advanced Photonics*, vol. 2, no. 05, Oct. 2020, ISSN: 2577-5421. DOI: 10.1117/1.AP.2.5.050501. [Online]. Available: https://www.spiedigitallibrary.org/journals/advanced-photonics/volume-2/issue-05/050501/Light-Lasers-and-the-Nobel-Prize/10.1117/1.AP.2.5.050501.full.

[2] T. Morikawa, Y. Mitsuhashi, J. Shimada, and Y. Kojima, "Return-beam-induced oscillations in self-coupled semiconductor lasers," en, *Electronics Letters*, vol. 12, no. 17, p. 435, 1976, ISSN: 00135194. DOI: 10.1049/el:19760331. [Online]. Available: https://digital-library.theiet.org/content/journals/10.1049/el_19760331.

[3] I. Ikushima and M. Maeda, "Self-coupled phenomena of semiconductor lasers caused by an optical fiber," en, *IEEE Journal of Quantum Electronics*, vol. 14, no. 5, pp. 331–332, May 1978, ISSN: 0018-9197. DOI: 10.1109/JQE.1978.1069791. [Online]. Available: http://ieeexplore.ieee.org/document/1069791/.

[4] K. Vahala, C. Harder, and A. Yariv, "Observation of relaxation resonance effects in the field spectrum of semiconductor lasers," en, *Applied Physics Letters*, vol. 42, no. 3, pp. 211–213, Feb. 1983, ISSN: 0003-6951, 1077-3118. DOI: 10.1063/1.93894. [Online]. Available: http://aip.scitation.org/doi/10.1063/1.93894.

[5] L. Goldberg, H. Taylor, A. Dandridge, J. Weller, and R. Miles, "Spectral characteristics of semiconductor lasers with optical feedback," en, *IEEE Journal of Quantum Electronics*, vol. 18, no. 4, pp. 555–564, Apr. 1982, ISSN: 0018-9197. DOI: 10.1109/JQE.1982.1071581. [Online]. Available: http://ieeexplore.ieee.org/document/1071581/.

[6] G. P. Agarwal and N. K. Dutta, *Semiconductor lasers*, 2nd ed. New York: Van Nostrand Reinhold, 1993.

[7] C. Henry, "Theory of the linewidth of semiconductor lasers," en, *IEEE Journal of Quantum Electronics*, vol. 18, no. 2, pp. 259–264, Feb. 1982, ISSN: 0018-9197. DOI: 10.1109/JQE.1982.1071522. [Online]. Available: http://ieeexplore.ieee.org/document/1071522/.

[8] R. Broom, E. Mohn, C. Risch, and R. Salathe, "Microwave self-modulation of a diode laser coupled to an external cavity," en, *IEEE Journal of Quantum Electronics*, vol. 6, no. 6, pp. 328–334, Jun. 1970, ISSN: 0018-9197. DOI: 10.1109/JQE.1970.1076461. [Online]. Available: http://ieeexplore.ieee.org/document/1076461/.

[9] R. O. Miles, A. Dandridge, A. B. Tveten, H. F. Taylor, and T. G. Giallorenzi, "Feedback-induced line broadening in cw channel-substrate planar laser diodes," en, *Applied Physics Letters*, vol. 37, no. 11, pp. 990–992, Dec. 1980, ISSN: 0003-6951, 1077-3118. DOI: 10.1063/1.91744. [Online]. Available: http://aip.scitation.org/doi/10.1063/1.91744.

[10] J. Osmundsen, B. Tromborg, and H. Olesen, "Experimental investigation of stability properties for a semiconductor laser with optical feedback," en, *Electronics Letters*, vol. 19, no. 25-26, p. 1068, 1983, ISSN: 00135194. DOI: 10.1049/el:19830725. [Online]. Available: https://digital-library.theiet.org/content/journals/10.1049/el_19830725.

[11] Y. C. Chen, "Phase noise characteristics of single mode semiconductor lasers with optical feedback," en, *Applied Physics Letters*, vol. 44, no. 1, pp. 10–12, Jan. 1984, ISSN: 0003-6951, 1077-3118. DOI: 10.1063/1.94573. [Online]. Available: http://aip.scitation.org/doi/10.1063/1.94573.

[12] J. S. Suelzer, A. Prasad, R. Ghosh, and G. Vemuri, "Effects of quantum noise on the nonlinear dynamics of a semiconductor laser subject to two spectrally filtered, time-delayed optical feedbacks," en, *Optics Communications*, vol. 370, pp. 209–221, Jul. 2016, ISSN: 00304018. DOI: 10.1016/j.optcom.2016.03.017. [Online]. Available: https://linkinghub.elsevier.com/retrieve/pii/S0030401816301808.

[13] R. Tkach and A. Chraplyvy, "Regimes of feedback effects in 1.5-µm distributed feedback lasers," *Journal of Lightwave Technology*, vol. 4, no. 11, pp. 1655–1661, 1986, ISSN: 0733-8724. DOI: 10.1109/JLT.1986.1074666. [Online]. Available: http://ieeexplore.ieee.org/document/1074666/.

[14] C. M. Bender and S. Boettcher, "Real Spectra in Non-Hermitian Hamiltonians Having P T Symmetry," en, *Physical Review Letters*, vol. 80, no. 24, pp. 5243–5246, Jun. 1998, ISSN: 0031-9007, 1079-7114. DOI: 10.1103/PhysRevLett.80.5243. [Online]. Available: https://link.aps.org/doi/10.1103/PhysRevLett.80.5243.

[15] C. M. Bender, D. C. Brody, and H. F. Jones, "Complex Extension of Quantum Mechanics," en, *Physical Review Letters*, vol. 89, no. 27, p. 270 401, Dec. 2002, ISSN: 0031-9007, 1079-7114. DOI: 10.1103/PhysRevLett.89.270401. [Online]. Available: https://link.aps.org/doi/10.1103/PhysRevLett.89.270401.

[16] J. Schindler, A. Li, M. C. Zheng, F. M. Ellis, and T. Kottos, "Experimental study of active *LRC* circuits with PT symmetries," en, *Physical Review A*, vol. 84, no. 4, p. 040 101, Oct. 2011, ISSN: 1050-2947, 1094-1622. DOI: 10.1103/PhysRevA.84.040101. [Online]. Available: https://link.aps.org/doi/10.1103/PhysRevA.84.040101.

[17] S. Bittner, B. Dietz, U. Günther, H. L. Harney, M. Miski-Oglu, A. Richter, and F. Schäfer, "P T Symmetry and Spontaneous Symmetry Breaking in a Microwave Billiard," en, *Physical Review Letters*, vol. 108, no. 2, p. 024 101, Jan. 2012, ISSN: 0031-9007, 1079-7114. DOI: 10.1103/PhysRevLett.108.024101. [Online]. Available: https://link.aps.org/doi/10.1103/PhysRevLett.108.024101.

[18] C. M. Bender, B. K. Berntson, D. Parker, and E. Samuel, "Observation of PT phase transition in a simple mechanical system," en, *American Journal of Physics*, vol. 81, no. 3, pp. 173–179, Mar. 2013, ISSN: 0002-9505, 1943-2909. DOI: 10.1119/1.4789549. [Online]. Available: http://aapt.scitation.org/doi/10.1119/1.4789549.

[19] R. Fleury, D. Sounas, and A. Alù, "An invisible acoustic sensor based on parity-time symmetry," en, *Nature Communications*, vol. 6, no. 1, p. 5905, May 2015, ISSN: 2041-1723. DOI: 10.1038/ncomms6905. [Online]. Available: http://www.nature.com/articles/ncomms6905.

[20] C. Hang, G. Huang, and V. V. Konotop, "P T Symmetry with a System of Three-Level Atoms," en, *Physical Review Letters*, vol. 110, no. 8, p. 083 604, Feb. 2013, ISSN: 0031-9007, 1079-7114. DOI: 10.1103/PhysRevLett.110.083604. [Online]. Available: https://link.aps.org/doi/10.1103/PhysRevLett.110.083604.

[21] Z. Zhang, Y. Zhang, J. Sheng, L. Yang, M.-A. Miri, D. N. Christodoulides, B. He, Y. Zhang, and M. Xiao, "Observation of Parity-Time Symmetry in Optically Induced Atomic Lattices," en, *Physical Review Letters*, vol. 117, no. 12, p. 123 601, Sep. 2016, ISSN: 0031-9007, 1079-7114. DOI: 10.1103/PhysRevLett.117.123601. [Online]. Available: https://link.aps.org/doi/10.1103/PhysRevLett.117.123601.

[22] P. Peng, W. Cao, C. Shen, W. Qu, J. Wen, L. Jiang, and Y. Xiao, "Anti-parity–time symmetry with flying atoms," en, *Nature Physics*, vol. 12, no. 12, pp. 1139–1145, Dec. 2016, ISSN: 1745-2473, 1745-2481. DOI: 10.1038/nphys3842. [Online]. Available: http://www.nature.com/articles/nphys3842.

[23] M. Wimmer, A. Regensburger, M.-A. Miri, C. Bersch, D. N. Christodoulides, and U. Peschel, "Observation of optical solitons in PT-symmetric lattices," en, *Nature Communications*, vol. 6, no. 1, p. 7782, Nov. 2015, ISSN: 2041-1723. DOI: 10.1038/ncomms8782. [Online]. Available: http://www.nature.com/articles/ncomms8782.

[24] Y. N. Joglekar, F. A. Onanga, and A. K. Harter, "Time-invariant PT product and phase locking in PT -symmetric lattice models," en, *Physical Review A*, vol. 97, no. 1, p. 012 128, Jan. 2018, ISSN: 2469-9926, 2469-9934. DOI: 10.1103/PhysRevA.97.012128. [Online]. Available: https://link.aps.org/doi/10.1103/PhysRevA.97.012128.

[25] J. Li, A. K. Harter, J. Liu, L. de Melo, Y. N. Joglekar, and L. Luo, "Observation of parity-time symmetry breaking transitions in a dissipative Floquet system of ultracold atoms," en, *Nature Communications*, vol. 10, no. 1, p. 855, Dec. 2019, ISSN: 2041-1723. DOI: 10.1038/s41467-019-08596-1. [Online]. Available: http://www.nature.com/articles/s41467-019-08596-1.

[26] F. Klauck, L. Teuber, M. Ornigotti, M. Heinrich, S. Scheel, and A. Szameit, "Observation of PT-symmetric quantum interference," en, *Nature Photonics*, vol. 13, no. 12, pp. 883–887, Dec. 2019, ISSN: 1749-4885, 1749-4893. DOI: 10.1038/s41566-019-0517-0. [Online]. Available: http://www.nature.com/articles/s41566-019-0517-0.

[27] R. El-Ganainy, K. G. Makris, M. Khajavikhan, Z. H. Musslimani, S. Rotter, and D. N. Christodoulides, "Non-Hermitian physics and PT symmetry," en, *Nature Physics*, vol. 14, no. 1, pp. 11–19, Jan. 2018, ISSN: 1745-2473, 1745-2481. DOI: 10.1038/nphys4323. [Online]. Available: http://www.nature.com/articles/nphys4323.

[28] C. M. Bender, D. W. Hook, P. N. Meisinger, and Q.-h. Wang, "Complex Correspondence Principle," en, *Physical Review Letters*, vol. 104, no. 6, p. 061 601, Feb. 2010, ISSN: 0031-9007, 1079-7114. DOI: 10.1103/PhysRevLett.104.061601. [Online]. Available: https://link.aps.org/doi/10.1103/PhysRevLett.104.061601.

[29] H. Hodaei, A. Hassan, S. Wittek, H. Garcia, R. El-Ganainy, D. N. Christodoulides, and M. Khajavikhan, "Enhanced sensitivity at higher-order exceptional points," en, *Nature*, vol. 548, no. 7666, pp. 187–191, Aug. 2017, ISSN: 0028-0836, 1476-4687. DOI: 10.1038/nature23280. [Online]. Available: http://www.nature.com/articles/nature23280.

[30] L. Feng, Z. J. Wong, R.-M. Ma, Y. Wang, and X. Zhang, "Single-mode laser by parity-time symmetry breaking," en, *Science*, vol. 346, no. 6212, pp. 972–975, Nov. 2014, ISSN: 0036-8075, 1095-9203. DOI: 10.1126/science.1258479. [Online]. Available: https://www.sciencemag.org/lookup/doi/10.1126/science.1258479.

[31] H. Jing, S. K. Özdemir, X.-Y. Lü, J. Zhang, L. Yang, and F. Nori, "PT -Symmetric Phonon Laser," en, *Physical Review Letters*, vol. 113, no. 5, p. 053 604, Jul. 2014, ISSN: 0031-9007, 1079-7114. DOI: 10.1103/PhysRevLett.113.053604. [Online]. Available: https://link.aps.org/doi/10.1103/PhysRevLett.113.053604.

[32] C. Yidong, "Asymmetry from symmetry," en, *Nature Physics*, vol. 10, no. 5, pp. 336–337, May 2014, ISSN: 1745-2473, 1745-2481. DOI: 10.1038/nphys2941. [Online]. Available: http://www.nature.com/articles/nphys2941.

[33] P. Ring and P. Schuck, *The nuclear many body problem*, eng, 1. ed., 3. print., study ed, ser. Texts and monographs in physics. Berlin Heidelberg: Springer, 2004, ISBN: 9783540212065.

[34] H. Lipkin, N. Meshkov, and A. Glick, "Validity of many-body approximation methods for a solvable model," en, *Nuclear Physics*, vol. 62, no. 2, pp. 188–198, Feb. 1965, ISSN: 00295582. DOI: 10.1016/0029-5582(65)90862-X. [Online]. Available: https://linkinghub.elsevier.com/retrieve/pii/002955826590862X.

[35] C. Dembowski, H.-D. Gräf, H. L. Harney, A. Heine, W. D. Heiss, H. Rehfeld, and A. Richter, "Experimental Observation of the Topological Structure of Exceptional Points," en, *Physical Review Letters*, vol. 86, no. 5, pp. 787–790, Jan. 2001, ISSN: 0031-9007, 1079-7114. DOI: 10.1103/PhysRevLett.86.787. [Online]. Available: https://link.aps.org/doi/10.1103/PhysRevLett.86.787.

[36] Ş. K. Özdemir, S. Rotter, F. Nori, and L. Yang, "Parity–time symmetry and exceptional points in photonics," en, *Nature Materials*, vol. 18, no. 8, pp. 783–798, Aug. 2019, ISSN: 1476-1122, 1476-4660. DOI: 10.1038/s41563-019-0304-9. [Online]. Available: http://www.nature.com/articles/s41563-019-0304-9.

[37] A. Guo, G. J. Salamo, D. Duchesne, R. Morandotti, M. Volatier-Ravat, V. Aimez, G. A. Siviloglou, and D. N. Christodoulides, "Observation of P T -Symmetry Breaking in Complex Optical Potentials," en, *Physical Review Letters*, vol. 103, no. 9, p. 093 902, Aug. 2009, ISSN: 0031-9007, 1079-7114. DOI: 10.1103/PhysRevLett.103.093902. [Online]. Available: https://link.aps.org/doi/10.1103/PhysRevLett.103.093902.

[38] S. Longhi, "Phase transitions in Wick-rotated PT -symmetric optics," en, *Annals of Physics*, vol. 360, pp. 150–160, Sep. 2015, ISSN: 00034916. DOI: 10.1016/j.aop.2015.05.008. [Online]. Available: https://linkinghub.elsevier.com/retrieve/pii/S000349161500192X.

[39] H.-J. Wünsche, S. Bauer, J. Kreissl, O. Ushakov, N. Korneyev, F. Henneberger, E. Wille, H. Erzgräber, M. Peil, W. Elsäßer, and I. Fischer, "Synchronization of Delay-Coupled Oscillators: A Study of Semiconductor Lasers," en, *Physical Review Letters*, vol. 94, no. 16, p. 163 901, Apr. 2005, ISSN: 0031-9007, 1079-7114. DOI: 10.1103/PhysRevLett.94.163901. [Online]. Available: https://link.aps.org/doi/10.1103/PhysRevLett.94.163901.

[40] L. Junges and J. A. C. Gallas, "Stability diagrams for continuous wide-range control of two mutually delay-coupled semiconductor lasers," *New Journal of Physics*, vol. 17, no. 5, p. 053 038, May 2015, ISSN: 1367-2630. DOI: 10.1088/1367-2630/17/5/053038. [Online]. Available: https://iopscience.iop.org/article/10.1088/1367-2630/17/5/053038.

[41] R. Lang and K. Kobayashi, "External optical feedback effects on semiconductor injection laser properties," en, *IEEE Journal of Quantum Electronics*, vol. 16, no. 3, pp. 347–355, Mar. 1980, ISSN: 0018-9197. DOI: 10.1109/JQE.1980.1070479. [Online]. Available: http://ieeexplore.ieee.org/document/1070479/.

[42] J. Mulet, C. Masoller, and C. R. Mirasso, "Modeling bidirectionally coupled single-mode semiconductor lasers," en, *Physical Review A*, vol. 65, no. 6, p. 063 815, Jun. 2002, ISSN: 1050-2947, 1094-1622. DOI: 10.1103/PhysRevA.65.063815. [Online]. Available: https://link.aps.org/doi/10.1103/PhysRevA.65.063815.

[43] A. Wilkey, J. Suelzer, Y. Joglekar, and G. Vemuri, "Parity–Time Symmetry in Bidirectionally Coupled Semiconductor Lasers," en, *Photonics*, vol. 6, no. 4, p. 122, Nov. 2019, ISSN: 2304-6732. DOI: 10.3390/photonics6040122. [Online]. Available: https://www.mdpi.com/2304-6732/6/4/122.

[44] Y. N. Joglekar, G. Vemuri, and A. Wilkey, "Lambert function methods for laser dynamics with time-delayed feedback," *Acta Polytechnica*, vol. 57, no. 6, p. 399, Dec. 2017, ISSN: 1805-2363, 1210-2709. DOI: 10.14311/AP.2017.57.0399. [Online]. Available: https://ojs.cvut.cz/ojs/index.php/ap/article/view/4608.

[45] N. Schunk and K. Petermann, "Numerical analysis of the feedback regimes for a single-mode semiconductor laser with external feedback," *IEEE Journal of Quantum Electronics*, vol. 24, no. 7, pp. 1242–1247, Jul. 1988, ISSN: 00189197. DOI: 10.1109/3.960. [Online]. Available: http://ieeexplore.ieee.org/document/960/.

[46] J. Mork and B. Tromborg, "The mechanism of mode selection for an external cavity laser," *IEEE Photonics Technology Letters*, vol. 2, no. 1, pp. 21–23, Jan. 1990, ISSN: 1041-1135, 1941-0174. DOI: 10.1109/68.47029. [Online]. Available: http://ieeexplore.ieee.org/document/47029/.

[47] J. Mork, B. Tromborg, and P. Christiansen, "Bistability and low-frequency fluctuations in semiconductor lasers with optical feedback: A theoretical analysis," *IEEE Journal of Quantum Electronics*, vol. 24, no. 2, pp. 123–133, Feb. 1988, ISSN: 0018-9197, 1558-1713. DOI: 10.1109/3.105. [Online]. Available: http://ieeexplore.ieee.org/document/105/.

[48] T. Sano, "Antimode dynamics and chaotic itinerancy in the coherence collapse of semiconductor lasers with optical feedback," en, *Physical Review A*, vol. 50, no. 3, pp. 2719–2726, Sep. 1994, ISSN: 1050-2947, 1094-1622. DOI: 10.1103/PhysRevA.50.2719. [Online]. Available: https://link.aps.org/doi/10.1103/PhysRevA.50.2719.

[49] P. M. Alsing, V. Kovanis, A. Gavrielides, and T. Erneux, "Lang and Kobayashi phase equation," en, *Physical Review A*, vol. 53, no. 6, pp. 4429–4434, Jun. 1996, ISSN: 1050-2947, 1094-1622. DOI: 10.1103/PhysRevA.53.4429. [Online]. Available: https://link.aps.org/doi/10.1103/PhysRevA.53.4429.

[50] Y. Takeuchi, R. Shogenji, and J. Ohtsubo, "Chaotic dynamics in semiconductor lasers subjected to polarization-rotated optical feedback," en, *Applied Physics Letters*, vol. 93, no. 18, p. 181 105, Nov. 2008, ISSN: 0003-6951, 1077-3118. DOI: 10.1063/1.3020302. [Online]. Available: http://aip.scitation.org/doi/10.1063/1.3020302.

[51] L. Ge, Y. D. Chong, S. Rotter, H. E. Türeci, and A. D. Stone, "Unconventional modes in lasers with spatially varying gain and loss," en, *Physical Review A*, vol. 84, no. 2, p. 023 820, Aug. 2011, ISSN: 1050-2947, 1094-1622. DOI: 10.1103/PhysRevA.84.023820. [Online]. Available: https://link.aps.org/doi/10.1103/PhysRevA.84.023820.

[52] M. C. Zheng, D. N. Christodoulides, R. Fleischmann, and T. Kottos, "PT optical lattices and universality in beam dynamics," en, *Physical Review A*, vol. 82, no. 1, p. 010 103, Jul. 2010, ISSN: 1050-2947, 1094-1622. DOI: 10.1103/PhysRevA.82.010103. [Online]. Available: https://link.aps.org/doi/10.1103/PhysRevA.82.010103.

[53] N. V. Alexeeva, I. V. Barashenkov, A. A. Sukhorukov, and Y. S. Kivshar, "Optical solitons in PT -symmetric nonlinear couplers with gain and loss," en, *Physical Review A*, vol. 85, no. 6, p. 063 837, Jun. 2012, ISSN: 1050-2947, 1094-1622. DOI: 10.1103/PhysRevA.85.063837. [Online]. Available: https://link.aps.org/doi/10.1103/PhysRevA.85.063837.

[54] H. Ramezani, J. Schindler, F. M. Ellis, U. Günther, and T. Kottos, "Bypassing the bandwidth theorem with PT symmetry," en, *Physical Review A*, vol. 85, no. 6, p. 062 122, Jun. 2012, ISSN: 1050-2947, 1094-1622. DOI: 10.1103/PhysRevA.85.062122. [Online]. Available: https://link.aps.org/doi/10.1103/PhysRevA.85.062122.

[55] A. Regensburger, C. Bersch, M.-A. Miri, G. Onishchukov, D. N. Christodoulides, and U. Peschel, "Parity–time synthetic photonic lattices," en, *Nature*, vol. 488, no. 7410, pp. 167–171, Aug. 2012, ISSN: 0028-0836, 1476-4687. DOI: 10.1038/nature11298. [Online]. Available: http://www.nature.com/articles/nature11298.

[56] G. S. Agarwal and K. Qu, "Spontaneous generation of photons in transmission of quantum fields in P T -symmetric optical systems," en, *Physical Review A*, vol. 85, no. 3, p. 031 802, Mar. 2012, ISSN: 1050-2947, 1094-1622. DOI: 10.1103/PhysRevA.85.031802. [Online]. Available: https://link.aps.org/doi/10.1103/PhysRevA.85.031802.

[57] R. El-Ganainy, J. I. Dadap, and R. M. Osgood, "Optical parametric amplification via non-Hermitian phase matching," en, *Optics Letters*, vol. 40, no. 21, p. 5086, Nov. 2015, ISSN: 0146-9592, 1539-4794. DOI: 10.1364/OL.40.005086. [Online]. Available: https://www.osapublishing.org/abstract.cfm?URI=ol-40-21-5086.

[58] J. Doppler, A. A. Mailybaev, J. Böhm, U. Kuhl, A. Girschik, F. Libisch, T. J. Milburn, P. Rabl, N. Moiseyev, and S. Rotter, "Dynamically encircling an exceptional point for asymmetric mode switching," en, *Nature*, vol. 537, no. 7618, pp. 76–79, Sep. 2016, ISSN: 0028-0836, 1476-4687. DOI: 10.1038/nature18605. [Online]. Available: http://www.nature.com/articles/nature18605.

[59] H. Hodaei, M. A. Miri, A. U. Hassan, W. E. Hayenga, M. Heinrich, D. N. Christodoulides, and M. Khajavikhan, "Parity-time-symmetric coupled microring lasers operating around an exceptional point," en, *Optics Letters*, vol. 40, no. 21, p. 4955, Nov. 2015, ISSN: 0146-9592, 1539-4794. DOI: 10.1364/OL.40.004955. [Online]. Available: https://www.osapublishing.org/abstract.cfm?URI=ol-40-21-4955.

[60] J. W. Yoon, Y. Choi, C. Hahn, G. Kim, S. H. Song, K.-Y. Yang, J. Y. Lee, Y. Kim, C. S. Lee, J. K. Shin, H.-S. Lee, and P. Berini, "Time-asymmetric loop around an exceptional point over the full optical communications band," en, *Nature*, vol. 562, no. 7725, pp. 86–90, Oct. 2018, ISSN: 0028-0836, 1476-4687. DOI: 10.1038/s41586-018-0523-2. [Online]. Available: http://www.nature.com/articles/s41586-018-0523-2.

[61] J. Zhang, B. Peng, Ş. K. Özdemir, Y.-x. Liu, H. Jing, X.-y. Lü, Y.-l. Liu, L. Yang, and F. Nori, "Giant nonlinearity via breaking parity-time symmetry: A route to low-threshold phonon diodes," en, *Physical Review B*, vol. 92, no. 11, p. 115 407, Sep. 2015, ISSN: 1098-0121, 1550-235X. DOI: 10.1103/PhysRevB.92.115407. [Online]. Available: https://link.aps.org/doi/10.1103/PhysRevB.92.115407.

[62] H. Lü, S. K. Özdemir, L.-M. Kuang, F. Nori, and H. Jing, "Exceptional Points in Random-Defect Phonon Lasers," en, *Physical Review Applied*, vol. 8, no. 4, p. 044 020, Oct. 2017, ISSN: 2331-7019. DOI: 10.1103/PhysRevApplied.8.044020. [Online]. Available: https://link.aps.org/doi/10.1103/PhysRevApplied.8.044020.

[63] A. Cerjan, A. Raman, and S. Fan, "Exceptional Contours and Band Structure Design in Parity-Time Symmetric Photonic Crystals," en, *Physical Review Letters*, vol. 116, no. 20, p. 203 902, May 2016, ISSN: 0031-9007, 1079-7114. DOI: 10.1103/PhysRevLett.116.203902. [Online]. Available: https://link.aps.org/doi/10.1103/PhysRevLett.116.203902.

[64] K. Ding, Z. Q. Zhang, and C. T. Chan, "Coalescence of exceptional points and phase diagrams for one-dimensional P T -symmetric photonic crystals," en, *Physical Review B*, vol. 92, no. 23, p. 235 310, Dec. 2015, ISSN: 1098-0121, 1550-235X. DOI: 10.1103/PhysRevB.92.235310. [Online]. Available: https://link.aps.org/doi/10.1103/PhysRevB.92.235310.

[65] W. D. Heiss, "Exceptional points of non-Hermitian operators," *Journal of Physics A: Mathematical and General*, vol. 37, no. 6, pp. 2455–2464, Feb. 2004, ISSN: 0305-4470, 1361-6447. DOI: 10.1088/0305-4470/37/6/034. [Online]. Available: https://iopscience.iop.org/article/10.1088/0305-4470/37/6/034.

[66] H. Liu, D. Sun, C. Zhang, M. Groesbeck, R. Mclaughlin, and Z. V. Vardeny, "Observation of exceptional points in magnonic parity-time symmetry devices," en, *Science Advances*, vol. 5, no. 11, eaax9144, Nov. 2019, ISSN: 2375-2548. DOI: 10.1126/sciadv.aax9144. [Online]. Available: https://advances.sciencemag.org/lookup/doi/10.1126/sciadv.aax9144.

[67] M. Sakhdari, M. Hajizadegan, Q. Zhong, D. N. Christodoulides, R. El-Ganainy, and P.-Y. Chen, "Experimental Observation of P T Symmetry Breaking near Divergent Exceptional Points," en, *Physical Review Letters*, vol. 123, no. 19, p. 193 901, Nov.

2019, ISSN: 0031-9007, 1079-7114. DOI: 10.1103/PhysRevLett.123.193901. [Online]. Available: https://link.aps.org/doi/10.1103/PhysRevLett.123.193901.

[68] Ş. K. Özdemir, S. Rotter, F. Nori, and L. Yang, "Parity–time symmetry and exceptional points in photonics," en, *Nature Materials*, vol. 18, no. 8, pp. 783–798, Aug. 2019, ISSN: 1476-1122, 1476-4660. DOI: 10.1038/s41563-019-0304-9. [Online]. Available: http://www.nature.com/articles/s41563-019-0304-9.

[69] M. Brandstetter, M. Liertzer, C. Deutsch, P. Klang, J. Schöberl, H. E. Türeci, G. Strasser, K. Unterrainer, and S. Rotter, "Reversing the pump dependence of a laser at an exceptional point," en, *Nature Communications*, vol. 5, no. 1, p. 4034, Sep. 2014, ISSN: 2041-1723. DOI: 10.1038/ncomms5034. [Online]. Available: http://www.nature.com/articles/ncomms5034.

[70] M. Liertzer, L. Ge, A. Cerjan, A. D. Stone, H. E. Türeci, and S. Rotter, "Pump-Induced Exceptional Points in Lasers," en, *Physical Review Letters*, vol. 108, no. 17, p. 173 901, Apr. 2012, ISSN: 0031-9007, 1079-7114. DOI: 10.1103/PhysRevLett.108.173901. [Online]. Available: https://link.aps.org/doi/10.1103/PhysRevLett.108.173901.

[71] H. Hodaei, A. U. Hassan, S. Wittek, H. Garcia-Gracia, R. El-Ganainy, D. N. Christodoulides, and M. Khajavikhan, "Enhanced sensitivity at higher-order exceptional points," en, *Nature*, vol. 548, no. 7666, pp. 187–191, Aug. 2017, ISSN: 0028-0836, 1476-4687. DOI: 10.1038/nature23280. [Online]. Available: http://www.nature.com/articles/nature23280.

[72] W. Chen, Ş. Kaya Özdemir, G. Zhao, J. Wiersig, and L. Yang, "Exceptional points enhance sensing in an optical microcavity," en, *Nature*, vol. 548, no. 7666, pp. 192–196, Aug. 2017, ISSN: 0028-0836, 1476-4687. DOI: 10.1038/nature23281. [Online]. Available: http://www.nature.com/articles/nature23281.

[73] J. Wiersig, "Enhancing the Sensitivity of Frequency and Energy Splitting Detection by Using Exceptional Points: Application to Microcavity Sensors for Single-Particle Detection," en, *Physical Review Letters*, vol. 112, no. 20, p. 203 901, May 2014, ISSN: 0031-9007, 1079-7114. DOI: 10.1103/PhysRevLett.112.203901. [Online]. Available: https://link.aps.org/doi/10.1103/PhysRevLett.112.203901.

[74] A. Wilkey, S. Joseph, J. Yogesh N., and V. Gautam, "Time-delay induced transitions in anti-PT system of coupled semiconductor lasers: Theory and experiment," *in preparation*,

[75] M. C. Soriano, J. García-Ojalvo, C. R. Mirasso, and I. Fischer, "Complex photonics: Dynamics and applications of delay-coupled semiconductors lasers," en, *Reviews of Modern Physics*, vol. 85, no. 1, pp. 421–470, Mar. 2013, ISSN: 0034-6861, 1539-0756. DOI: 10.1103/RevModPhys.85.421. [Online]. Available: https://link.aps.org/doi/10.1103/RevModPhys.85.421.

[76] G. Van Tartwijk, A. Levine, and D. Lenstra, "Sisyphus effect in semiconductor lasers with optical feedback," *IEEE Journal of Selected Topics in Quantum Electronics*, vol. 1, no. 2, pp. 466–472, Jun. 1995, ISSN: 1077260X. DOI: 10.1109/2944.401230. [Online]. Available: http://ieeexplore.ieee.org/document/401230/.

[77] H. Olesen, J. Osmundsen, and B. Tromborg, "Nonlinear dynamics and spectral behavior for an external cavity laser," en, *IEEE Journal of Quantum Electronics*, vol. 22, no. 6, pp. 762–773, Jun. 1986, ISSN: 0018-9197. DOI: 10.1109/JQE.1986.1073061. [Online]. Available: http://ieeexplore.ieee.org/document/1073061/.

[78] F. Zhang, Y. Feng, X. Chen, L. Ge, and W. Wan, "Synthetic Anti-PT Symmetry in a Single Microcavity," en, *Physical Review Letters*, vol. 124, no. 5, p. 053 901, Feb. 2020, ISSN: 0031-9007, 1079-7114. DOI: 10.1103/PhysRevLett.124.053901. [Online]. Available: https://link.aps.org/doi/10.1103/PhysRevLett.124.053901.

[79] Y. Li, Y.-G. Peng, L. Han, M.-A. Miri, W. Li, M. Xiao, X.-F. Zhu, J. Zhao, A. Alù, S. Fan, and C.-W. Qiu, "Anti–parity-time symmetry in diffusive systems," en, *Science*, vol. 364, no. 6436, pp. 170–173, Apr. 2019, ISSN: 0036-8075, 1095-9203. DOI: 10.1126/science.aaw6259. [Online]. Available: https://science.sciencemag.org/content/364/6436/170.

[80] A. R. Wilkey, Y. N. Joglekar, J. S. Suelzer, and G. Vemuri, "Non-hermitian dynamics in delay coupled semiconductor lasers," in *Active Photonic Platforms XI*, G. S. Subramania and S. Foteinopoulou, Eds., San Diego, United States: SPIE, Sep. 2019, p. 16, ISBN: 9781510628557 9781510628564. DOI: 10.1117/12.2523786. [Online]. Available: https://www.spiedigitallibrary.org/conference-proceedings-of-spie/11081/2523786/Non-hermitian-dynamics-in-delay-coupled-semiconductor-lasers/10.1117/12.2523786.full.

[81] R. M. Corless, G. H. Gonnet, D. E. G. Hare, D. J. Jeffrey, and D. E. Knuth, "On the LambertW function," en, *Advances in Computational Mathematics*, vol. 5, no. 1, pp. 329–359, Dec. 1996, ISSN: 1019-7168, 1572-9044. DOI: 10.1007/BF02124750. [Online]. Available: http://link.springer.com/10.1007/BF02124750.